

Fiber Optic Temperature Effects for Compensation of Strain Measurements

R. Martin Kaumanns




MASTERARBEIT**FIBER OPTIC TEMPERATURE EFFECTS
FOR COMPENSATION OF STRAIN
MEASUREMENTS**

Freigabe:

Der Bearbeiter:

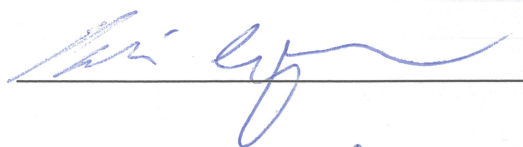
Unterschriften

R. Martin Kaumanns



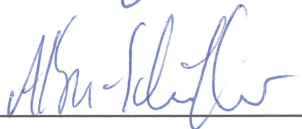
Betreuer:

Patrick Leyendecker

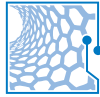


Der Institutsdirektor

Prof. Alin Albu-Schäffer



Dieser Bericht enthält 104 Seiten, 29 Abbildungen und 02 Tabellen



Lehrstuhl für
Nanoelektronik

Technische Universität München



TECHNISCHE UNIVERSITÄT MÜNCHEN
FAKULTÄT FÜR ELEKTROTECHNIK UND INFORMATIONSTECHNIK
LEHRSTUHL FÜR NANOELEKTRONIK
PROF. DR. PAOLO LUGLI

Fiber Optic Temperature Effects for Compensation of Strain Measurements

MASTER THESIS

by R. Martin Kaumanns

February 10, 2014

Abstract

This work analyzes the applicability of different temperature sensing methods in order to compensate Fiber Bragg Grating based strain measurements in a short segment of a single fiber. The presented methods for temperature measurements relying on the refractive index (including reflectometry techniques) or on scattering effects have significant disadvantages for simultaneous strain and temperature measurement. Despite this result a method for high resolution distributed temperature measurement is introduced based on spatially distributed fiber Bragg gratings.

In contrast to refractive index methods, doped fibers show promising properties. This work derives a detailed model of doped fiber fluorescence lifetime, leading to the conclusion that the fluorescence spectrum is more suited for temperature sensing. Additionally, a connection between absorption, stimulated emission, spontaneous emission and the measured spectrum is developed based on the fluorescence lifetime model found. The results emphasize the need to treat the measured spectrum as the steady state of a dynamic system rather than an approximated representation of internal absorption and emission spectra.

The fluorescence spectrum will be used for temperature sensing by tracking lowpass effects in the spectrum. The optimal doping material is subject to further research and not determined in this work.

Contents

1	Introduction	1
2	State of the Art	5
2.1	Ideal Undoped Fibers	5
2.1.1	Birefringent Fibers	6
2.1.2	Varying Refractive Indices along a Fiber	8
2.1.3	Varying Refractive Indices along a Birefringent Fiber	11
2.2	Ideal Doped Fibers	13
2.3	Non-Ideal Fibers	15
2.3.1	Brillouin Scattering	16
2.3.2	Raman Scattering	16
2.3.3	Simultaneous Measurement of Strain and Temperature	17
2.4	Conclusion	17
3	Fluorescence Lifetime	19
3.1	Calculation and Dependencies	19
3.2	Experimental Results	27
4	Fluorescence Spectrum	33
4.1	Calculation and Dependencies	33
4.2	Temperature Dependence of the Absorption Spectrum	39
4.2.1	Fluorescence Intensity Ratio (FIR)	42
4.2.2	Fourier Domain Intensity Ratio (FDIR)	45
4.3	Experimental Results	47
4.3.1	Fluorescence Intensity Ratio	50
4.3.2	Fourier Domain Intensity Ratio	50
4.3.3	Comparison	51

5	Reflectometry	55
5.1	Network Analysis Optical Frequency Domain Reflectometry	55
5.1.1	Method	55
5.1.2	Resolution	57
5.2	Incoherent Frequency-Modulated Continuous Wave OFDR	57
5.2.1	Method	57
5.2.2	Resolution	58
5.3	Coherent Optical Frequency Domain Reflectometry	59
5.3.1	Method	59
5.3.2	Resolution	64
5.3.3	Reflectivity Value Based Measurement	70
5.3.4	Position Based Measurement	72
5.3.5	Fitting Functions	74
5.3.6	Experimental Results	75
6	Conclusion	81
	List of Figures	a
	List of Tables	a
	Bibliography	j
	Acknowledgements	k

1 Introduction

In robotics strain measurements belong to the most often addressed problems. In order to control the motion of a robot or to provide some kind of force feedback when controlling the robot, measuring the strain is essential.

One example for a robotic system is shown in figure 1.1. The *MiroSurge System* was developed at the German Aerospace Center (DLR) and is used for minimally invasive surgery applications. Instruments (e.g. the gripper depicted in figure 1.1) are attached to the tip of a slim robot arm and remote controlled by the surgeon. In order to give the surgeon force feedback information, a six degrees of freedom force/torque sensor is located behind the exemplary gripper. The sensor design is based on the *Stewart platform*. The force/torque is calculated by analyzing the strain induced in the links between top and bottom segment [GH03]. One approach for strain measuring is the use of strain gauges, which change their resistance in case of strain. However, due to the position of the strain sensor, size and medical compatibility are of special interest.

Optical approaches have promising properties regarding possible sensor sizes and medical compatibility. Examples for medical compatibility are the need to avoid electrical signals near the measurement area or having a sensor design robust enough to sustain a sterilization process (e.g. sterilization by applying high temperatures or chemicals). An example for optical strain measurement is presented in [Has13], where Fiber Bragg Gratings (FBGs) are used for measuring the strains in the Stewart platform leading to one of the smallest six degrees of freedom sensor to date. The sensor is shown in figure 1.2.

Both the electronical and FBG-based optical sensor systems suffer from a critical drawback: Changes in length or refractive index are not only influenced by strain changes, but also by temperature changes. Relating to the medical application, a simple body contact could increase the temperature and cause the measurement of a non-existent force. In case of the Fiber Bragg Grating based approach, a dependency of about $1 \frac{\text{N}}{\text{K}}$ is observed [Has13]. Because of this, a temperature compensation is indispensable. One solution is the use of temperature sensors with additional circuitry and components, which undermines the advantages of the small and electronic-free light-based system. A second solution is an optical temperature sensor placed near the force sensors as presented in [Has13]. This solution suffers from the assumption of uniform temperature distribution, which is not necessarily true for medical applications. Additionally a

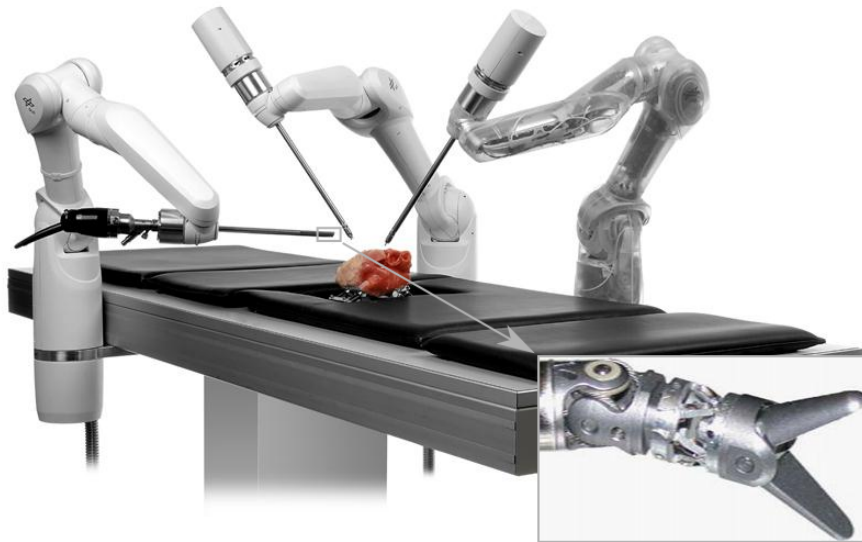


Figure 1.1: One example for a medical robotic system with a strain sensor (structure behind the gripper in the small image) for force feedback: The MiroSurge system is used for telemanipulation in minimally invasive surgery. Due to its position, the strain sensor has high demands regarding medical compatibility and size. Image ©DLR.

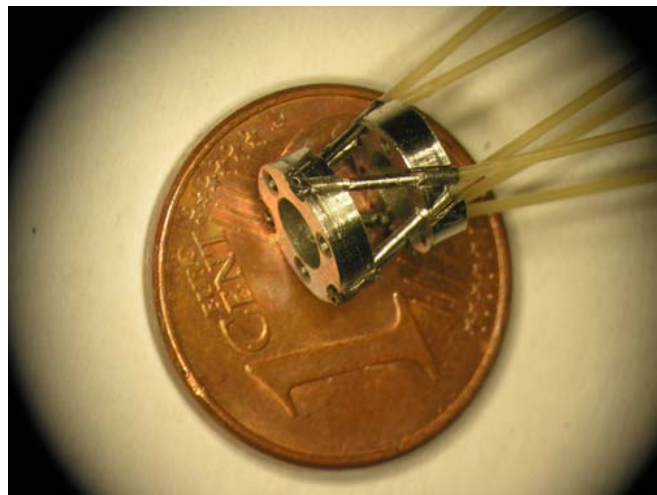


Figure 1.2: An example for a fiber optic strain sensor developed for the use in the MiroSurge system (figure 1.1) [Has13]. Image from [Ley10].

second sensor increases the sensor size. This explains the need for an optical approach at the same location as the strain sensor.

Important for this integrated compensation is its independence from the light intensity and the possibility of simultaneous strain measurement. Even if a certain intensity for the input light can be guaranteed, the intensity of the output light will be influenced by the properties of the transmitting fiber. The transmitting fiber can change the attenuation of the light due to a lot of effects. One example would be bending, which is unavoidable in a flexible system with moving parts. This work will evaluate the possibilities for such an optical, integrated and intensity independent (or at least intensity compensated) measurement of temperature with the possibility of simultaneous strain measurements.

In order to simplify the measurements, all approaches are only analyzed for their ability to measure the temperature. If the temperature measurement shows significant disadvantages, no proper temperature compensation can be expected in case of applied strain. The target application is the compensation of the strain sensor presented in [Has13] and depicted in 1.2. Thus the compensation must be usable for fiber segments with a length of approximately $L \approx 5.5$ mm. The application in minimally invasive surgery implies a temperature range from 283 K to 323 K that is used as operating range in the following.

In chapter 2, properties of single mode optical fibers and their suitability to compensate temperatures in the targeted setup are analyzed. A model of the fluorescence lifetime for doped fibers is derived in chapter 3 in order to test the robustness of lifetime measurements for temperature sensing. The measured emission spectrum of doped fibers is explained in chapter 4 and the observed temperature dependency is used for temperature measurements. In chapter 5, optical frequency domain reflectometry is used to determine intensity compensated reflection magnitudes and wavelengths of spatially distributed Fiber Bragg Gratings to test the applicability for simultaneous distributed strain and temperature measurement.

2 State of the Art

Since the optical strain measurement system is (single mode) fiber based, it is important to know which fiber types are available and how they differ. The most common fiber type is the pure silica undoped fiber. Undoped fibers differ in the distribution of their refractive indices. Doped fibers contain additional doping material that can be excited by transmitted light.

The properties of these two types will be presented based on ideal fibers. Finally the imperfections of optical fibers and their use for measurements will be discussed.

One special fiber type not covered in this work is the microstructured optical fiber, where the light guiding is done through manipulation of the waveguide structure rather than through the refractive index.

2.1 Ideal Undoped Fibers

Amongst others, undoped fibers may be distinguished by two properties: their refractive index and their length. Both properties are sensitive to temperature and to strain.

There are no significant influences on the light for a constant refractive index in an ideal fiber. Thus a constant refractive index is not suitable for sensing purposes. Three possibilities exist for varying refractive indices: they can vary along the fiber, with the polarization (usually in case of birefringence, which will be explained later) or with the polarization *and* along the (birefringent) fiber.

Because the target of this work is the simultaneous measurement of strain and temperature and the measurement of two effects needs at least two independent equations, a configuration is needed where two independent measurements are possible.

One possibility is to use two different wavelengths for the measurement. The refractive index is usually wavelength dependent, thus two completely different systems based on completely different refractive indices can be analyzed by using two wavelengths. Unfortunately, the variance of the refractive index and especially the variance of its reaction to temperature or strain changes is almost negligible. [Gho94] for instance measured a practically constant relative temperature sensitivity of about

$\frac{\partial_T n}{n} \approx 15 \cdot 10^{-6} \frac{1}{K}$ for wavelengths above 800 nm and in case of silica glasses. Due to the small variance, a measurement based on different wavelengths would be rather insensitive [Fer00]. This is why more sophisticated approaches are needed for the generation of two measurements.

In the following, possible configurations of undoped fibers are presented and their ability to provide two independent measurement equations are compared. Light can be divided into two categories: static light and time varying light. For this reason, every fiber configuration is analyzed with respect to both light categories.

2.1.1 Birefringent Fibers

Birefringent fibers exhibit two separate refractive indices for the incoming light – one for horizontal and one for vertical polarized light. The difference of refractive indices is called birefringence and is temperature sensitive. Generally speaking, every fiber is birefringent due to manufacturing imperfections, bending or other effects. This is why special care must be taken to ensure that the transmitting fiber does not have a significant influence on the measurement.

Static Input Light

Measurement Technique The refractive index difference must change either the polarization or the wavelength of the incoming light in case of static input light in order to get an intensity independent measurement.

Circular birefringent fibers are a subtype of so called *optically active materials*. Linearly polarized light is rotated by a circular birefringent fiber according to the difference of refractive indices. Therefore a polarization based measurement technique is possible. Polarization maintenance in optical fibers is especially difficult as nearly every fiber has some birefringent properties. The polarization may be changed depending on the temperature, pressure/bending or rotation of the transmission fiber causing false measurements. Robust polarizing maintaining fibers exist, but are normally built to transmit one particular polarization only [Dre12]. This is why a wavelength based approach may be preferable in general.

The difference of refractive indices in standard birefringent fibers generates two separate paths (one for each refractive index) splitted up prior and combined after the birefringent fiber. The difference in optical length for both paths creates an interference pattern filtering certain wavelengths (interferometer principle). Each path transmits a certain polarization orientation only. In order to achieve proper interference of both paths, a polarization filter after the birefringent fiber is needed [Ciu05]. The working principle is also depicted in figure 2.1. For proper interference, the polarization

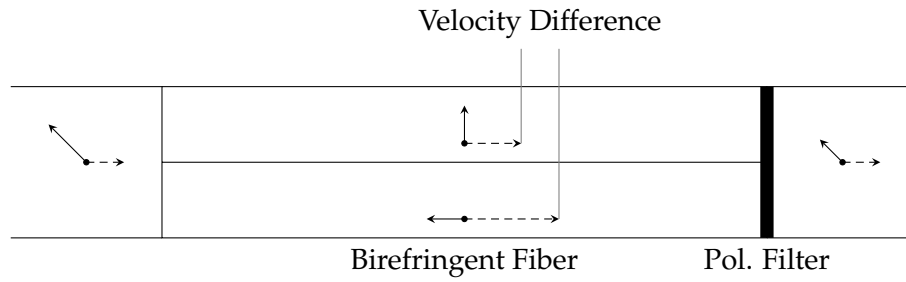


Figure 2.1: An interferometer based on a birefringent fiber. Light coupled into the birefringent fiber is splitted into a horizontally and vertically polarized fraction. Each fraction propagates through the fiber with different velocities due to the different refractive indices causing a phase (or path) difference. A linear polarization filter at the end of the birefringent fiber creates an interference between both polarization paths.

filter should be placed as near as possible to the sensing area to reduce the influence of the transmission fiber. Polarization changes after the interference point do not affect the intensity, which is why birefringent effects in the transmission fiber after the polarization filter are not problematic. A polarization filter and a polarization maintaining fiber prior to the sensor fiber ensures that the birefringence of the transmitting fiber has no influence (the second birefringence channel of the transmitting fiber will be empty, thus no difference in optical length will be generated by the transmitting fiber).

An example for a system using birefringence is the temperature sensor built by *OpSens* based on White-Light-Polarization Interferometry [Ops10].

Simultaneous Measurement of Strain and Temperature Purely birefringent fibers can be used to measure the difference of refractive indices in the fiber by analyzing the filtering pattern of the interferometer. Since there is no other feature and the refractive indices can be assumed to stay constant for every input light, there is no direct way for simultaneous measurement of strain and temperature as the second equation is missing.

Time Varying Input Light

Measurement Technique In order to exhibit a measurable effect on time varying light, the fiber must change the time variation of the input signal. Changing the time variation needs some kind of memory element (just like in electronics). The only memory element available in undoped fibers is their (optical) length, meaning that the analyzed features must be distributed along the propagation direction to cause different outputs.

The spatially distributed feature in birefringent fibers is the (differing) optical lengths for each path through the birefringent fiber. Using time varying light, the differing time delay corresponding to the optical length can be directly observed. Just like in the static case, a polarization filter and polarization maintaining fiber prior to the sensor fiber reduces the influence of the transmitting fiber. A polarization filter after the birefringent fiber is not necessary as no interference is needed.

It is important to note, that only the time difference and not the absolute time of both channels provides information about the birefringence of the fiber. The absolute time also includes the refractive index and the length of the transmitting fiber, which is usually not part of the sensing area.

Simultaneous Measurement of Strain and Temperature Similar to the static light case, only the birefringence can be measured. One feature is not enough for measuring two effects making the simultaneous measurement of strain and force impossible with the setup described.

However, a more sophisticated method for time varying birefringence measurement is presented in [Par96] based on the *Kerr Effect*. In this technique, a high power, circularly-polarised pulse of light induces a transient birefringence grating. A fluctuation of powers occurs for a counter propagating CW probe beam. The frequency of this fluctuation depends on the local birefringence. Therefore instead of only measuring the birefringence along the whole fiber, distributed birefringence measurements are possible. Accordingly, the position and the value of the birefringence can be used to build up an equation system. However the setup is complex and reaches spatial resolutions of only 0.6 m with 3 K accuracy, which is far too low for the target application of this work. In a similar manner, *Transient Brillouin Gratings* induced by two counter propagating short pump pulses have been used for distributed birefringence measurements yielding a resolution of 20 cm [Don10], which is still too much for a sensor in the millimeter scale.

2.1.2 Varying Refractive Indices along a Fiber

Reflection of light may occur whenever light travels from a medium of a given refractive index into a medium with a different refractive index. Therefore changing the refractive index along the fiber creates temperature dependent positions of certain reflectivities. For a measurement, the effect of the reflectivities on an input light must be analyzed.

Static Input Light

Measurement Technique If static light is used, the reflectivities must have an influence on the polarization or on the wavelengths of the light in order to obtain an intensity independent indicator for the measurand.

A fiber without any polarization dependent effect will not change the polarity in any way, which is why the polarization is not usable for measurement in this case.

To create a wavelength filter based on reflectivities, the reflectivities must be located in a way that allows interferences of the reflected light, thus providing an interference filter. A refractive index profile with such properties is a Fiber Bragg Grating.

A Fiber Bragg Grating [Hil97] [Erd97] is a periodic variation of the refractive index in an optical fiber. The grating causes the reflection of a certain wavelength λ_B that fulfills the *Bragg Condition* $\lambda_B = 2n_{eff}\Lambda$ with grating period Λ and effective fiber refractive index n_{eff} . Other wavelengths are transmitted. Therefore the reflection wavelength is direct proportional to the effective refractive index in the fiber and the grating periodicity. Applying temperatures to Fiber Bragg Gratings changes the elongation (i.e. grating periodicity) and refractive index of the fiber leading to a different reflection wavelength λ_B . The changed behavior can be observed and the applied temperature can be calculated.

Fiber Bragg Gratings are widely used for sensor applications. One example is optical temperature measurement as proposed in [Rao97].

Simultaneous Measurement of Strain and Temperature Special Fiber Bragg Gratings can even reflect multiple wavelengths. Two reflected wavelengths could be used to build up a system of two independent equations.

There are some approaches based on the changing of the periodicity or refractive index combinations along the fiber to create two or more reflected wavelengths (an overview can be found in [Che07]). But these approaches face the same disadvantages as two separate fiber Bragg gratings – the temperature and the strain might change along the fiber creating false measurements and longer grating structures are needed. Because the periodicity should not change along the fiber, the only degree of freedom left is the orientation of the grating. This is normally done by tilting the grating leading to so called *Tilted Fiber Bragg Gratings* [Mel89] as shown in figure 2.2.

Tilted fiber Bragg gratings can be explained by the use of coupled mode theory [Erd96], which is beyond the scope of this thesis. Roughly explained, the tilt changes the direction of the reflections and thus their mode. Modes differing from the core mode are coupled into the cladding and their backpropagating path is determined by the effective refractive index of the cladding. The wavelengths fulfilling the Bragg condition

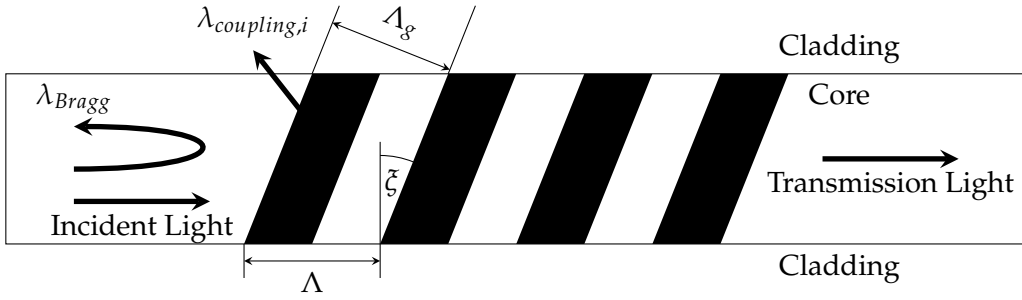


Figure 2.2: A Tilted Fiber Bragg Grating in an optical fiber according to [Don11]. Λ is the grating period and ζ represents the tilt angle and i is an index for a certain mode. The dark areas are regions with a different refractive index.

for the sum of the forward propagating core path and the backpropagating cladding path underly constructive interference in reflection and will partly vanish in transmission. However the reflections will be absorbed by the cladding and not be visible. A fraction of the reflections will stay in the core mode and the normal Fiber Bragg Formulas still apply for this fraction. Thus there is more than one reflected wavelength in a Tilted Fiber Bragg Grating (one wavelength for every mode i), but the complete set is only visible in the transmission spectrum.

One disadvantage is that the measurement of notches (in the transmission spectrum) instead of peaks (in the reflection spectrum) is more imprecise due to the weaker signal and thus undesirable. The second disadvantage of tilted gratings is the dependency of the Bragg wavelengths on the effective refractive index of the cladding. According to [Don11], the cladding's effective refractive index has been shown to be sensitive to the ambient refractive index (e.g. air). Thus, tilted gratings are suitable for analyzing surrounding liquids or gases, but inadequate for measurements in changing environments.

To sum up, none of the methods presented provides a satisfactory way to use Fiber Bragg Gratings in combination with static light to measure strain and temperature simultaneously in the same location in the fiber.

Time Varying Input Light

Measurement Technique As already mentioned in section 2.1.1, spatially distributed features are needed for time varying input light. In the case of varying refractive indices, these are the reflectivities in the fiber. With the help of reflectometry (e.g. *Optical Frequency Domain Reflectometry* or *Optical Time Domain Reflectometry*), the positions in the optical path, which depend on the refractive index, and the magnitude of the reflection can be measured. Especially the position information provides a stable

measurement for the refractive indices and the length of the fiber. A more detailed explanation follows in chapter 5.

A measurement system based on this approach is proposed by *Luna Inc.* [Sam12]. But instead of using artificially created reflectivities, the system is based on Rayleigh scattering that is inherent to every fiber. Rayleigh scatterings will be briefly discussed in chapter 2.3.

Simultaneous Measurement of Strain and Temperature As stated above, two properties can be measured: the optical position of the reflectivities and the reflectivity values themselves. These two measurements would be enough in order to measure strain and temperature. A disadvantage is that the reflectometry principle is based on a reference reflectivity. Attenuation changes (e.g. bending of the fiber) between the reference and the measurement reflectivity as well as changes of the reference reflectivity (e.g. due to temperature) will affect the measurement of the reflectivity values. In contrast, the optical positions of the reflectivities are independent of the reference. However, the reference reflectivity can be designed to be stable regarding external influences. This is why reflectometry techniques will be analyzed in more detail in chapter 5.

2.1.3 Varying Refractive Indices along a Birefringent Fiber

The third approach is to vary the refractive index along the fiber *and* with the polarization, which is essentially just a combination of the already analyzed methods.

Static Input Light

Measurement Technique For static input light, the periodical variation of the refractive index forms a Fiber Bragg Grating. The combination of a Fiber Bragg Grating in a birefringent fiber and a polarization based interferometer as observed for birefringent fibers leads to three wavelength filters. The Fiber Bragg Grating reflects different wavelengths in each channel of the birefringent fiber due to the differing refractive indices. The interferometer features a periodic transfer function based on the fiber length and the difference of the refractive indices. In reflection, only the two peaks caused by the Fiber Bragg Grating are visible. The reason is, that the two differing wavelengths in the reflection path are unable to interfere making the interferometer useless. In transmission, this setup leads to the periodic transfer function of the interferometer combined with the two Bragg wavelengths staying unaffected by the interferometer curve as the interference partner in the other channel got reflected.

The reflection properties are obviously more interesting as sharp peaks can be measured more easily. But in reflection, the interferometer feature does not have a significant effect on the measurement. In transmission, detecting the fiber Bragg wavelengths is quite complex as they do not always form a clear notch or a peak. Without being able to measure the Bragg wavelengths in a stable manner, the Fiber Bragg Grating is unnecessary. Thus in reflection the interferometer is not usable and in transmission, the Fiber Bragg Grating cannot be measured.

To be able to measure an effect significantly different from the previous configurations, the measurements should be done in reflection without the need for a polarizer. The two Bragg wavelengths measured correspond to the two refractive indices present in the birefringent fiber.

Simultaneous Measurement of Strain and Temperature As the two refractive indices of a birefringent fiber are independent, their reaction to temperature or strain can be assumed to be different. As the Bragg wavelengths are directly proportional to the corresponding (effective) refractive index, the two measured Bragg wavelengths are expected to exhibit different sensitivities to temperature respective strain. Accordingly an equation system for the Bragg wavelengths based on two independent equations can be created. If this equation system is solved for the two unknowns *temperature* and *strain*, a simultaneous measurement of strain and temperature is possible [Fer00].

Disadvantageous of using a birefringent Fiber Bragg Grating is that both channels react to changes in strain and temperature in the same way while only being different regarding the amount of the reaction. This leads to a decrease in sensitivity as an accurate solving of the equation system relies on the difference (or independence) of the reactions (compare to performances listed in [Che07]).

Additionally, the reflection peaks of the Fiber Bragg Grating might overlap, creating the need to separate both polarizations for proper measurement. However, maintaining two different polarizations in the transmission fiber is difficult as polarization maintaining fibers are normally designed to maintain one polarization only and normal fibers are likely to destroy or vary the polarizations due to bending or curling of the fiber.

Time Varying Input Light

Measurement Technique Time varying input light is used to analyze spatially distributed features. In case of birefringent fibers, these are the optical lengths in both channels. For varying refractive indices, these are the positions of the reflectivities in the optical path.

Like in the non-birefringent case, the optical positions and values of the reflectivities in the system can be determined by using reflectometry. But in contrast to the non-birefringent case, the reflectivities are distributed over two channels with different refractive indices changing the optical position.

Simultaneous Measurement of Strain and Temperature As already mentioned, the measurement of the reflectivity values using reflectometry depends on a reference reflectivity, which makes it more difficult to use them for a robust measurement. But in contrast to the non-birefringent case, the optical positions for reflectivities of two channels can be measured. These two channels provide information about the two refractive indices of the fiber.

The strain and the temperature could be measured by using the value of these two refractive indices. But just like in the static light case, the refractive indices will react to strain and temperature in the same way. The difference of the reaction is important for a precise measurement. But this difference will stay much smaller than the reaction itself, similar to [Fer00].

Additionally, without a polarizer, one cannot distinguish between the channels and the reflectometry would just detect reflectivities at the positions corresponding to their optical distance. If it is known which reflectivity corresponds to which channel, a simultaneous measurement of two refractive indices would be possible although no polarizer is involved as the optical position depends on the corresponding refractive index. However, the reflectivity positions of both channels might overlap in the measurement preventing a proper separation of both channels without using a polarizer. Yet, using a polarizer for separation of the channels is difficult due to the general difficulties of transmitting differently polarized light in fibers in a robust way (compare to the static light case).

2.2 Ideal Doped Fibers

A more convenient way to compensate for temperature is to use an effect independent of the strain measurement. Since the refractive index is strain sensitive, optical effects which are not based on the refractive indices are of special interest. Fibers providing such effects are fibers doped with an active material, most commonly with rare earth elements like Erbium or Ytterbium. The doping causes optical properties which are almost completely independent of strain but dependent on temperature [Col02], thus the doping could be used for temperature measurements. A method based on varying refractive indices along the fiber (e.g. Fiber Bragg Gratings) can provide the strain measurements within the doped fiber.

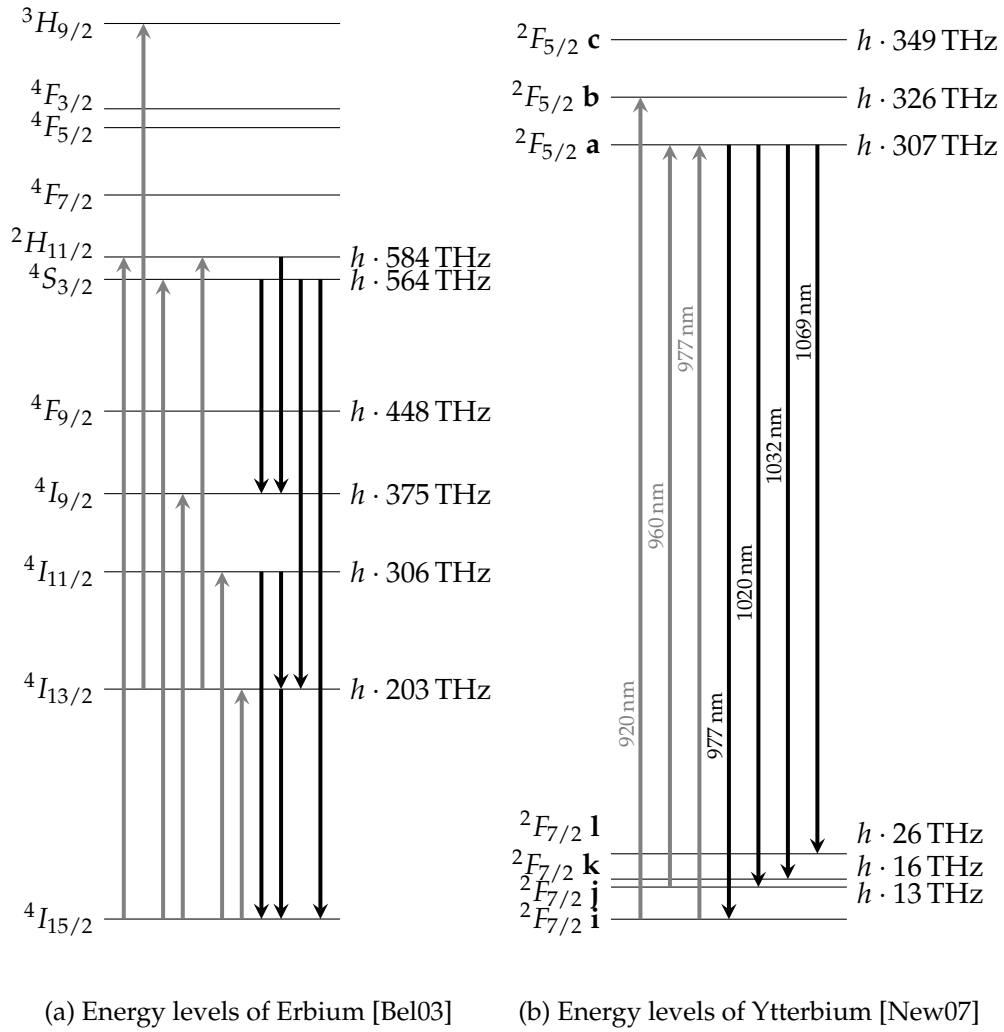


Figure 2.3: Energy levels of Erbium and Ytterbium with the energy expressed in terms of optical frequency and referenced to ground level.

Erbium is a rare earth element with a lot of energy levels/transitions (compare to figure 2.3a) and fibers can only be doped lowly due to quenching effects [Mys97]. For this reason, it is hard to handle for researching purposes as theoretical models (if existent) are complex and inaccurate plus the interaction with the input light is weak. Nevertheless, it is widely used because it emits light in the C-Band that is common in telecommunication.

In contrast to Erbium, Ytterbium almost represents an ideal two level system (compare to figure 2.3b), which is easier and more precise to model, and can be doped at higher concentrations. Therefore Ytterbium, is used for the following analysis.

Single mode light has the following features: its spectrum, its polarization and the behavior of both over time. Since doped fibers do not exhibit significant emission properties with respect to the polarization, the leftover interesting features are the

spectrum and the spectrum over time. These properties can be modified for the input light and the influence of the fiber can be analyzed for the output light.

As already mentioned, if the input light varies over time, the system must have some kind of memory capability to be able to change the variation in a measurable manner. Doped fibers do not memorize wavelengths but intensities. After light of a certain intensity has excited the dopant, the material will stay excited for a short time followed by an emission of light at a different wavelength. The emission wavelength depends on the emission spectrum of the material and the emission intensity depends on the exciting intensity generating some kind of intensity memory. This is why intensity-varying light will be filtered by the material but wavelength-varying light will just be converted to certain emission wavelengths. Consequentially only the variation of intensity over time is analyzed in the *spectrum over time* case.

To sum up, there are two set ups worth analyzing in the fluorescence measurement: apply light with a fixed input spectrum and analyzing the corresponding (fixed) output spectrum or inputting light with a time varying intensity and measuring the corresponding output intensity dynamics. The former is often addressed by the fluorescence intensity ratio measurement, the latter by the fluorescence lifetime measurement (compare to [Col02]). The lifetime measurement is discussed in more detail in chapter 3, the intensity ratio in chapter 4.

2.3 Non-Ideal Fibers

Non ideal fibers exhibit some formerly discussed properties: They are normally birefringent, the refractive index does not stay constant along the fiber and changes with wavelengths, they attenuate light in a nonlinear way for example depending on bending or humidity, they cannot transmit every wavelength or may even emit light at other wavelengths caused by chemical impurities. Some of these properties may be intended in order to provide different fiber variants (see section 2.1 or 2.2). Others can be reduced by careful design. And some can be used for measurements.

Parasitic non-ideal effects are usually very weak. Additionally, they will occur in the transmitting and in the sensing fiber, generating the need to separate the origin of the effect. Assigning origins to a non-ideal effect implies that the (measured) effect must occur in distinguishable locations. This reduces the usable effects for sensing and leads to reflectivities or more generally, scattering effects. Using static light cannot provide any conclusions about the spatial distribution of the scatterings. For this reason, scattering effects are normally measured using time-varying light based on reflectometry techniques.

An example for a scattering effect is *Rayleigh scattering*, which reflects light at the same wavelength as the input light. Reflectivities with the same wavelength as the input light (mostly caused by different refractive indices along the fiber) have already been covered in section 2.1. Other notable scattering effects in the field of fiber optics are *Brillouin scattering* and *Raman scattering* [Sin07].

2.3.1 Brillouin Scattering

Brillouin scattering is caused by time dependent optical density variations. It reflects light at different wavelengths than the input light. One reason for such density variations is temperature. Since optical density is also strain dependent, Brillouin scattering is often used for distributed strain measurement. While the Brillouin intensity normalized by the Rayleigh intensity (also called *Landau-Placzek-Ratio*) is dominantly temperature dependent [PCW96], the reflection wavelengths are dependent on the applied strain and temperature [Par97].

The reflection wavelengths are close to the input wavelength (the wavelength shift is small), differ along the fiber and thus are complex to measure in a distributed way. Essentially the response spectrum of each location in the fibre must be measured to be able to calculate the wavelength shift. Some approaches are explained in [Thé10], but most of the traditional methods are limited to a spatial resolution of about 1 m reducing the field of application to very long fibers. There are some experiments that were able to reach a resolution of 1 cm [Son10]. But this is still too imprecise for the target application of this work.

However temperature measurement is possible with higher resolutions as only the intensities of the scattering need to be measured. Yet, the (commercially) most successful distributed temperature measurements based on scattering intensities are based on Raman scattering [De 01] due to the easier spectral separation from the Rayleigh scattering and its larger sensitivity [PCW96].

2.3.2 Raman Scattering

Raman scattering reflects light at higher and lower wavelengths symmetric to the input wavelength. The reflection with higher wavelengths is called *Stokes Raman scattering* and the lower wavelengths reflection *Anti-Stokes Raman Scattering*. Using the ratio of both scatterings compensates possible attenuation effects in the fiber. Comparable to Brillouin scattering, the intensities of the anti-stokes scatterings are primarily temperature sensitive [Ala05]. And just like for Brillouin scattering, the wavelength shift of Raman scattering depends, in addition to the used material, on the applied strain [Hua09] [Rob87] and temperature [Har70]. But in contrast to Brillouin scattering, this wavelength shift is normally not used for strain measurements [Ina06].

2.3.3 Simultaneous Measurement of Strain and Temperature

Raman and Brillouin scattering show similar types of sensitivities to strain and temperature. Measuring frequency shifts along the fiber is complicated in the necessary millimeter scale, which is why the scattering intensities may be used preferably. Both intensities are primarily temperature dependent, but Raman scattering has found wider use for distributed temperature measurement.

Using birefringence for strain measurements would disturb the accurate measurement of the scattering intensities as the two separate channels would overlap in the measurement (compare to section 2.1.3). Doped fibers are not very strain sensitive (see section 2.2). However, the strain of the system could be measured by using reflectivity locations along the fiber combined with the already applied varying input light (just like in section 2.1.2).

Due to their promising properties, scattering based measurements are discussed in chapter 5 along with the reflectometry based measurement of refractive indices along a fiber as introduced in section 2.1.2.

2.4 Conclusion

Table 2.1 gives an overview of the most important ways and properties to measure temperatures in optical fibers.

Based on the previous discussion, the only approach based on ideal undoped fibers that seems worth analyzing regarding simultaneous strain and temperature measurement, is the measurement of reflection magnitudes and reflection positions along a fiber using reflectometry analysis. The other approaches are either too sensitive to their environment or too insensitive to the measurands. However, the applicability of reflection magnitude and reflection position measurements for simultaneous temperature and strain sensing needs further evaluation.

Property	Remark
Birefringence	Polarization dependent
Refractive index changings	Similar reactions for strain and temperature
Absorption and emission	For doped fibers, strain independent
Scatterings	Weak signals, various origins, strain independent

Table 2.1: Summary of temperature dependent properties in fibers. Dealing with polarization dependence proved to be cumbersome as reported by [Fer00] and [Dre12], thus birefringence based methods are not in the focus of this work.

Doped fiber methods are widely researched, mostly using the fluorescence lifetime or the fluorescence intensity ratio and promise a good way to measure the temperature almost independently from possible strains [Col02]. Yet, the publications for temperature detection based on fluorescence lifetime do not cover short fibers with high excitation needed for good signal to noise ratios. Moreover, the fluorescence intensity ratio is only one way to filter the temperature dependency of the spectrum, but other ways (e.g. based on the full spectrum) are still unreported.

A temperature measurement based on a quite strain independent method is also provided by the analysis of scatterings. Yet, scattering measurements have primarily been used for long fibers and the applicability for temperature compensation in short fibers with high resolutions requires clarification.

This is why both doped fiber methods will be addressed in this work (chapter 3 and 4) in addition to a reflectometry based measurement for changes in refractive index or scattering effects (chapter 5).

All methods except the analysis of changes in refractive index are nearly strain independent. The strain measurement could, for instance, be added by using Fiber Bragg Gratings (for doped fibers) or reflectivity locations in the fiber (for Raman/Brillouin scattering).

3 Fluorescence Lifetime

If a doped fiber is exposed to light of a certain wavelength, the energies of some photons are absorbed by the electrons of the dopant. The absorption causes a change of the energy level, such that (for example) electrons in the first energy level are raised to the second energy level (compare to figure 2.3b or 3.1c). The electrons are called *excited* in this case. They stay excited for certain amount of time before they return to their original energy level under emission of photons. This emission is called *fluorescence*. The time between excitation and emission is called *fluorescence lifetime*. If the fluorescence intensity is measured directly after stopping the excitation of the fiber (i.e. after stopping the exposure to light), a decay $I(t)$ of the fluorescence intensity can be measured. The time constant τ of this decay is closely connected to the fluorescence lifetime. In fact this time constant τ is used as representation of the fluorescence lifetime in the following.

It is generally assumed that the decay $I(t)$ of the measured fluorescence intensity is exponential, i.e. of the form

$$I(t) = I(0) \exp\left(-\frac{t}{\tau}\right). \quad (3.1)$$

Numerous publications are based on this assumption, e.g. [Zha93],[Zha96], [Sun98] and [Sun04] to name a few. However own measurements showed, that the assumption does not hold for short fibers (see figure 3.3). This observation has also been made in [Bow05]. It is shown in the following, that an exponential decay can only be expected for low fluorescence powers in case of short fibers.

3.1 Calculation and Dependencies

To be able to make statements about the dependencies and robustness of the fluorescence lifetime, its origin must be derived. Optical systems can reach a high complexity, thus some simplifications are made.

First of all, the following calculations are based on ideal two level systems without any radiationless transitions. Since the measurements are based on Ytterbium, this assumption holds sufficiently well. The reflections at the fiber boundaries will be ignored, which requires good splices and identical refractive indices for the transmitting

Variable	Description
ν	Optical frequency of the light
T	Temperature of the fiber section
$N_1(t)$	Density of electrons in the ground energy level
$N_2(t)$	Density of electrons in the excited energy level
N	Density of excitable electrons (doping)
$N_{2,\nu}(t)$	Balance for the density of electrons in the excited energy level for a certain frequency ν
$u_\nu(t)$	Density of photons from an external source
$B_\nu(T)$	Density of photons caused by Planckian radiation (temperature radiation)
$Y_\nu(t)$	Overall amount of fluorescence photons (or defect of photons) in fiber section caused by emission/absorption
$y_\nu(t)$	Average density of fluorescence photons (or defect of photons) caused by emission/absorption
$g_\nu(t)$	Overall density of photons in the fiber
E_ν	Transmission function of the measurement system
$I(t)$	Intensity of the measured light
$\sigma_{a,\nu}$	Effective absorption cross-section (absorption probability)
$\sigma_{e,\nu}$	Effective emission cross-section (stimulated emission probability)
a_ν	Emission probability (spontaneous emission probability)
v_ν	Group velocity of light in the fiber

Table 3.1: Notation used for fluorescence calculations. The index ν expresses the variable's dependency to the optical frequency ν .

and sensing fiber. Additionally, the photon density (i.e. excitation light) in the fiber is assumed to be constant along the fiber. The external input light should be time constant.

In reality, the photon density will change along the fiber creating an infinite amount of fiber sections. For proper calculation, each fiber section would need to be modeled to have a distinct external input and fluorescence output. As the fluorescence propagates in every direction, the fluorescence output will be the input for each neighboring fiber section each having an own fluorescence output. This would lead to an infinite cyclic network of fiber sections, which is only numerically solvable.

The notation used for the following calculations is summed up in table 3.1. For the variables, the following logical connections exist

$$N = N_1(t) + N_2(t) \quad (3.2)$$

$$N_2(t) = \int_0^\infty N_{2,\nu}(t) d\nu \quad (3.3)$$

$$g_\nu(t) = u_\nu(t) + B_\nu(T) + y_\nu(t). \quad (3.4)$$

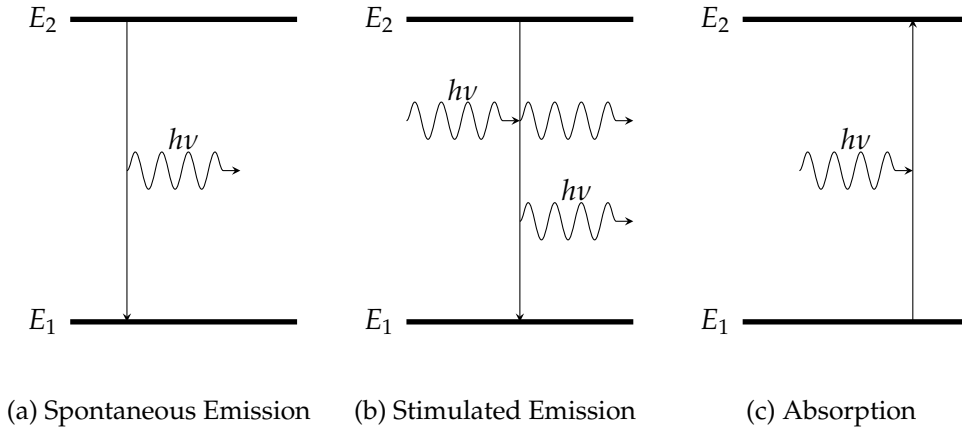


Figure 3.1: The main causes for electron transitions in fluorescent materials. Depicted is an ideal two level system with ground energy level E_1 and excited energy level E_2 . A spontaneous decay of an electron from the second energy level to the ground level is called spontaneous emission and generates a photon with energy $h\nu \approx E_2 - E_1$. A photon with energy $h\nu$ can also stimulate an emission of another photon with the same propagation direction and energy $h\nu$. This process is called stimulated emission. In the case of absorption, a photon with energy $h\nu$ excites an electron from ground level to the excited energy level.

The first equation states, that the overall amount of excitable electrons is equal to the amount of electrons being in the first or second energy level. $N_{2,\nu}(t)$ represents the difference of electrons having absorbed a photon with frequency ν minus the electrons having emitted a photon with frequency ν . Or in other words the current balance of electrons in the second energy level for a certain frequency ν . The total amount of electrons in the second energy level is the sum (or integral) over the balances of all frequencies ν . This is stated by the second equation. The last equation states, that the photons in the fiber section consist of photons caused by an external light source, photons caused by Planckian radiation and photons created during the fiber internal absorption/emission process.

According to [McC64], the system must fulfill the rate equation denoted by

$$-\dot{N}_{2,\nu}(t) = \sigma_{e,\nu} g_\nu(t) v_\nu N_2(t) + a_\nu N_2(t) - \sigma_{a,\nu} g_\nu(t) v_\nu N_1(t). \quad (3.5)$$

Essentially the rate equation states the following: The amount of emitted photons per second per unit volume for a certain optical frequency equals the amount of photons emitted by stimulated emission (figure 3.1b) plus the photons spontaneously emitted (figure 3.1a) minus the absorbed photons (figure 3.1c). Note that the emission of each photon causes a decay of an electron from second to ground energy level, thus the amount of emitted photons per second per unit volume equals the amount of electron decays per second per unit volume $-\dot{N}_{2,\nu}(t)$. The concept of stimulated emission, spontaneous emission and absorption is further explained in figure 3.1.

Let $l_v(t, \Delta t, \mathbf{x})$ be the percentage of emitted photons that have been generated at position \mathbf{x} at the time $t - \Delta t$ and are still in the fiber at the time t . First of all, it is assumed that the distribution of photon emitting directions and generation positions stays constant over time. Thus, the times needed for leaving the fiber stay constant. Secondly, the mean duration until reabsorption for each emitted photon is assumed to be long compared to the time needed for leaving the fiber, such that the lifetime of photons in the fiber is dominated by the fiber dimensions. Then it follows that $l_v(t, \Delta t, \mathbf{x})$ is approximately time constant and will just depend on Δt making it independent from t . In case $l_v(t, \Delta t, \mathbf{x})$ drops fast enough over Δt (which is normally true as the time needed by photons to leave the fiber is much smaller than the time constants of the system), only very small values of Δt must be taken into account. For small values of Δt , $\dot{N}_{2,v}(t - \Delta t)$ can be assumed to be constant over Δt , i.e. $\dot{N}_{2,v}(t - \Delta t) \approx \dot{N}_{2,v}(t)$. These assumptions yield the following equation for the overall amount of fluorescence photons in the fiber:

$$Y_v(t) = - \int_{\mathbf{x}} \int_0^\infty l_v(t, \Delta t, \mathbf{x}) \dot{N}_{2,v}(t - \Delta t) d\Delta t d\mathbf{x} \approx - \dot{N}_{2,v}(t) \int_{\mathbf{x}} \int_0^\infty l_v(\Delta t, \mathbf{x}) d\Delta t d\mathbf{x}. \quad (3.6)$$

To fulfill the assumption of position independent photon density, the average density of fluorescence photons is used for further calculations. The average density in a fiber of radius r and length L with average photon lifetime $\Delta \tilde{t}_v$ is

$$y_v(t) \approx \frac{Y_v(t)}{\pi r^2 L} \approx - \dot{N}_{2,v}(t) \frac{\int_{\mathbf{x}} \int_0^\infty l_v(\Delta t, \mathbf{x}) d\Delta t d\mathbf{x}}{\pi r^2 L} = - \Delta \tilde{t}_v \cdot \dot{N}_{2,v}(t). \quad (3.7)$$

The measured power $I(t)$ will consist of all photons located at the fiber's end surface travelling towards the photodiode. The fiber end pointing towards the photodiode is passed by $\pi r^2 \cdot g_v(t)$ photons per meter. The distribution of different photon emission directions is assumed to stay constant (at least for the optical frequencies measured). Thus of all emitted photons, only the time constant percentage e_v actually propagates towards the photodiode. The remaining emitted photons never reach the photodiode. Therefore the photodiode measures the fractional amount of $e_v \cdot \pi r^2 g_v(t)$ photons. The first ds meters after the fiber end will be filled up with $ds \cdot e_v \pi r^2 g_v(t)$ photons. It took the photons $dt = \frac{ds}{v_v}$ seconds to reach the distance ds . Because $ds \cdot e_v \pi r^2 g_v(t)$ photons each having the energy $h\nu$ left the fiber in dt seconds, the power (i.e. energy per timestep) leaving the fiber is

$$I_v(t) = h\nu \cdot v_v \cdot e_v \pi r^2 g_v(t). \quad (3.8)$$

Of course the photodiode will have its own sensivity \tilde{e}_ν for each optical frequency. Thus the power measured by the photodiode is

$$I(t) = \int_0^\infty \tilde{e}_\nu \cdot h\nu v_\nu e_\nu \pi r^2 g_\nu(t) d\nu = \int_0^\infty E_\nu g_\nu(t) d\nu, \quad (3.9)$$

where E_ν is used to sum up the transmission function $\tilde{e}_\nu h\nu v_\nu e_\nu \pi r^2$.

With all connections between the variables explained, the system can be analyzed in more detail. To solve this system, a differential equation based on a measurable variable is derived, e.g. $g_\nu(t)$. Starting with equation (3.4), plugging in equation (3.7) and deriving yields

$$g_\nu(t) \approx u_\nu(t) + B_\nu(T) - \Delta \tilde{t}_\nu \cdot \dot{N}_{2,\nu}(t) \quad (3.10)$$

$$\dot{g}_\nu(t) \approx \dot{u}_\nu(t) - \Delta \tilde{t}_\nu \cdot \ddot{N}_{2,\nu}(t). \quad (3.11)$$

The same can be done using equation (3.5) and (3.2)

$$\dot{N}_{2,\nu}(t) = -[\sigma_{e,\nu} + \sigma_{a,\nu}] g_\nu(t) v_\nu N_2(t) - a_\nu N_2(t) + \sigma_{a,\nu} g_\nu(t) v_\nu N \quad (3.12)$$

$$\ddot{N}_{2,\nu}(t) = -[\sigma_{e,\nu} + \sigma_{a,\nu}] v_\nu [\dot{g}_\nu(t) N_2(t) + g_\nu(t) \dot{N}_2(t)] - a_\nu \dot{N}_2(t) + \sigma_{a,\nu} \dot{g}_\nu(t) v_\nu N. \quad (3.13)$$

And the last formula needed for a complete differential equation is the derivation of equation (3.3) using the *Leibniz Integral Rule*

$$\dot{N}_2(t) = \int_0^\infty \dot{N}_{2,\nu}(t) d\nu. \quad (3.14)$$

Inserting equation (3.12) into (3.14), (3.14) into (3.13), (3.13) into (3.11) and (3.12) into (3.10) leads to two equations with the variable $N_2(t)$ being in both equations. Thus it is possible to replace $N_2(t)$ creating a single differential equation based on $g_\nu(t)$. The result is

$$\sigma_\nu = [\sigma_{a,\nu} + \sigma_{e,\nu}] v_\nu \quad (3.15)$$

$$\tilde{u}_{\nu,T}(t) = u_\nu(t) + B_\nu(T) \quad (3.16)$$

$$k_\nu = 1 + \Delta \tilde{t}_\nu v_\nu \sigma_{a,\nu} N \quad (3.17)$$

$$\dot{g}_\nu(t) \approx [\sigma_\nu g_\nu(t) + a_\nu] \frac{[\sigma_\nu g_\nu(t) + a_\nu] \Delta \tilde{t}_\nu \int_0^\infty \frac{\tilde{u}_{\nu,T}(t) - g_\nu(t)}{\Delta \tilde{t}_\nu} d\nu + \dot{u}_\nu(t)}{\sigma_\nu \tilde{u}_{\nu,T}(t) + a_\nu k_\nu}. \quad (3.18)$$

The system dynamics should not be part of the measurement integral in equation (3.9) as this would require the exact knowledge of E_ν in order to draw the connection between the measured dynamics and the actual system dynamics. Hence $g_\nu(t)$ should ideally be of the following form with the system dynamics modeled by the frequency

constant $f_k(t)$ and the frequency behavior modeled by the time constant $h_k(\nu)$

$$g_\nu(t) \stackrel{!}{=} \sum_{k=1}^K f_k(t) h_k(\nu). \quad (3.19)$$

This postulate yields an intensity with the time variable (i.e. the system dynamics) outside the measurement integral

$$I(t) \stackrel{!}{=} \sum_{k=1}^K f_k(t) \int_0^\infty E_\nu h_k(\nu) d\nu. \quad (3.20)$$

If using this approach does not lead to any conflict, a valid solution for the differential equation has been found.

Plugging equation (3.19) into (3.18) yields

$$c_\nu(t) = \frac{\left[\sigma_\nu \sum_{k=1}^K f_k(t) h_k(\nu) + a_\nu \right] \Delta \tilde{t}_\nu \int_0^\infty \frac{\tilde{u}_{\nu,T}(t) - \sum_{k=1}^K f_k(t) h_k(\nu)}{\Delta \tilde{t}_\nu} d\nu + \dot{u}_\nu(t)}{\sigma_\nu \tilde{u}_{\nu,T}(t) + a_\nu k_\nu}, \quad (3.21)$$

with

$$\sum_{k=1}^K \dot{f}_k(t) h_k(\nu) \stackrel{!}{\approx} \sum_{k=1}^K f_k(t) h_k(\nu) \sigma_\nu c_\nu(t) + a_\nu c_\nu(t). \quad (3.22)$$

Let

$$f_1(t) = 1 \quad (3.23)$$

$$h_1(\nu) = -\frac{a_\nu}{\sigma_\nu} \quad (3.24)$$

in order to remove the appended term $a_\nu c_\nu(t)$. Then the index $k = 1$ in equation (3.22) can be substituted leading to

$$\sum_{k=2}^K \dot{f}_k(t) h_k(\nu) \stackrel{!}{\approx} \sum_{k=2}^K f_k(t) h_k(\nu) \sigma_\nu c_\nu(t). \quad (3.25)$$

According to the comparison of coefficients, $\sigma_\nu c_\nu(t)$ should only be time dependent

$$c(t) = \sigma_\nu c_\nu(t) = \frac{\sigma_\nu^2 \Delta \tilde{t}_\nu \int_0^\infty \frac{\tilde{u}_{\nu,T}(t) - \sum_{k=1}^K f_k(t) h_k(\nu)}{\Delta \tilde{t}_\nu} d\nu \sum_{k=2}^K f_k(t) h_k(\nu) + \sigma_\nu \dot{u}_\nu(t)}{\sigma_\nu \tilde{u}_{\nu,T}(t) + a_\nu k_\nu}. \quad (3.26)$$

Resolving this expression for the sum yields

$$\sum_{k=2}^K f_k(t) h_k(\nu) = \frac{c(t)}{\int_0^\infty \frac{\tilde{u}_{\nu,T}(t) - \sum_{k=1}^K f_k(t) h_k(\nu)}{\Delta \tilde{t}_\nu} d\nu} \cdot \frac{\sigma_\nu \tilde{u}_{\nu,T}(t) + a_\nu k_\nu - \frac{\sigma_\nu \dot{u}_\nu(t)}{c(t)}}{\sigma_\nu^2 \Delta \tilde{t}_\nu}. \quad (3.27)$$

Although it is possible to treat $u_v(t)$ as time changing variable $u_v(t) = u_v u_t$, the system will be hardly solvable due to its increased complexity. Therefore, as already mentioned, $u_v(t)$ is assumed to be time constant in the following calculations

$$\sum_{k=2}^K f_k(t) h_k(v) = \frac{c(t)}{\int_0^\infty \frac{\tilde{u}_{v,T} - \sum_{k=1}^K f_k(t) h_k(v)}{\Delta \tilde{t}_v} dv} \cdot \frac{\sigma_v \tilde{u}_{v,T} + a_v k_v}{\sigma_v^2 \Delta \tilde{t}_v}. \quad (3.28)$$

The comparison of the coefficients yields for the remaining indices

$$f_2(t) = \frac{c(t)}{\int_0^\infty \frac{\tilde{u}_{v,T} - \sum_{k=1}^K f_k(t) h_k(v)}{\Delta \tilde{t}_v} dv} \quad (3.29)$$

$$h_2(v) = \frac{\sigma_v \tilde{u}_{v,T} + a_v k_v}{\sigma_v^2 \Delta \tilde{t}_v}. \quad (3.30)$$

Thus for $c(t)$ holds (with $f_2(t)$ as unknown variable and using equations (3.23), (3.24), (3.29) and (3.30))

$$c(t) = f_2(t) \int_0^\infty \frac{\tilde{u}_{v,T} + \frac{a_v}{\sigma_v} - f_2(t) \frac{\sigma_v \tilde{u}_{v,T} + a_v k_v}{\sigma_v^2 \Delta \tilde{t}_v}}{\Delta \tilde{t}_v} dv. \quad (3.31)$$

According to the formulas (3.25), (3.26) and (3.31) the simplified differential equation to solve is

$$\dot{f}_2(t) \approx f_2(t) c(t) = f_2(t)^2 \int_0^\infty \frac{\tilde{u}_{v,T} + \frac{a_v}{\sigma_v}}{\Delta \tilde{t}_v} dv - f_2(t)^3 \int_0^\infty \frac{\sigma_v \tilde{u}_{v,T} + a_v k_v}{\sigma_v^2 \Delta \tilde{t}_v^2} dv. \quad (3.32)$$

This differential equation is solved using a Computer Algebra System like *Mathematica*. The solution is implicitly given by

$$a = \int_0^\infty \frac{\tilde{u}_{v,T} + \frac{a_v}{\sigma_v}}{\Delta \tilde{t}_v} dv \quad (3.33)$$

$$b = \int_0^\infty \frac{\sigma_v \tilde{u}_{v,T} + a_v k_v}{\sigma_v^2 \Delta \tilde{t}_v^2} dv \quad (3.34)$$

$$t + C_1 = -\frac{1}{a^2} \left[b \ln \left(\frac{a}{f_2(t)} - b \right) + \frac{a}{f_2(t)} \right]. \quad (3.35)$$

$f_2(t)$ can be substituted with the measurable value $I(t)$ by using equation (3.20) as well as (3.23), (3.24) and (3.30). Thus

$$c = \int_0^\infty E_v \frac{\sigma_v \tilde{u}_{v,T} + a_v k_v}{\sigma_v^2 \Delta \tilde{t}_v} dv \quad (3.36)$$

$$d = \int_0^\infty E_v \frac{a_v}{\sigma_v} dv \quad (3.37)$$

$$f_2(t) = \frac{I(t) + d}{c}. \quad (3.38)$$

C_1 can be calculated by setting $t = 0$, i.e.

$$C_1 = -\frac{1}{a^2} \left[b \ln \left(\frac{ac}{I(0) + d} - b \right) + \frac{ac}{I(0) + d} \right]. \quad (3.39)$$

Combining equations (3.35), (3.38) and (3.39) yields

$$\tau = \frac{b}{a^2} = \frac{\int_0^\infty \frac{\tilde{u}_{\nu,T} + \frac{a_\nu}{\sigma_\nu} k_\nu}{\sigma_\nu \Delta \tilde{t}_\nu^2} d\nu}{\left(\int_0^\infty \frac{\tilde{u}_{\nu,T} + \frac{a_\nu}{\sigma_\nu}}{\Delta \tilde{t}_\nu} d\nu \right)^2} \quad (3.40)$$

$$f = \frac{ac}{b} = \frac{\int_0^\infty \frac{\tilde{u}_{\nu,T} + \frac{a_\nu}{\sigma_\nu}}{\Delta \tilde{t}_\nu} d\nu \int_0^\infty E_\nu \frac{\sigma_\nu \tilde{u}_{\nu,T} + a_\nu k_\nu}{\sigma_\nu^2 \Delta \tilde{t}_\nu} d\nu}{\int_0^\infty \frac{\sigma_\nu \tilde{u}_{\nu,T} + a_\nu k_\nu}{\sigma_\nu^2 \Delta \tilde{t}_\nu^2} d\nu} \quad (3.41)$$

$$t = \tau \left[\ln \left(\frac{I(0) - (f - d)}{I(t) - (f - d)} \right) + \ln \left(\frac{I(t) + d}{I(0) + d} \right) + \frac{f}{I(0) + d} - \frac{f}{I(t) + d} \right]. \quad (3.42)$$

Note that $I(t) \geq 0$ and $d > 0$, meaning that no matter what value $I(t)$ takes, the equation cannot reach $t = \infty$ based on the last two summands, which must be a valid value for a time continuous system. Thus, the only way to reach $t = \infty$ is that the logarithms reach infinity leading to the condition

$$\frac{I(\infty) + d}{I(\infty) - (f - d)} \stackrel{!}{=} \infty$$

$$I(\infty) = f - d. \quad (3.43)$$

This simplifies equation (3.42) to

$$t = \tau \left[\ln \left(\frac{I(0) - I(\infty)}{I(t) - I(\infty)} \right) + \ln \left(\frac{I(t) + d}{I(0) + d} \right) + \frac{I(\infty) + d}{I(0) + d} - \frac{I(\infty) + d}{I(t) + d} \right]. \quad (3.44)$$

Equations (3.44) and (3.40) represent the most detailed derivation of fluorescence decay to the author's knowledge. Two possible simplifications in case d is much bigger than $I(0)$ are

$$\text{Semiexponential Simplification:} \quad t = \tau \ln \left(\frac{I(0) - I(\infty)}{I(t) - I(\infty)} \cdot \frac{I(t) + d}{I(0) + d} \right) \quad (3.45)$$

$$\text{Exponential Simplification:} \quad t = \tau \ln \left(\frac{I(0) - I(\infty)}{I(t) - I(\infty)} \right). \quad (3.46)$$

The former simplification has also been found by [Bow05], who assumed (amongst others) that the average density of fluorescence photons $y_\nu(t)$ is proportional to the density of electrons in the excited energy level $N_2(t)$, i.e. $y_\nu(t) \approx C_\nu N_2(t)$ with frequency dependent constant C_ν . Note that d partly compensates the missing two summands. Thus, d found by fitting equation (3.45) will not entirely correspond to d found by fitting equation (3.44). The latter represents the ideal exponential decay already

mentioned in equation (3.1). Both simplifications make it possible to express $I(t)$ in an explicit way.

The influence of the measurement system E_v is found in the variable d , while the lifetime τ is completely independent of the measurement system. Yet the lifetime τ relies on the input photon density u_v (equation (3.40)). In order to get comparable lifetime measurements, u_v must be kept at the exact same level which is hard to guarantee in real life applications. Additionally, the dependence of the lifetime τ on u_v implies that the dynamic system is not a linear time invariant system.

The temperature dependence of τ can primarily be found in the temperature radiance $B_v(T)$ and in the rate equation coefficients a_v , $\sigma_{a,v}$ and $\sigma_{e,v}$. Temperature changes in v_v will cause equivalent changes in $\Delta\tilde{t}_v$ and $\tilde{u}_{v,T}$ cancelling out the change.

τ depends on the doping density N , which is sensitive to strain. $\Delta\tilde{t}_v$ also shows a small strain sensitivity as an applied strain changes the geometry of the fiber leading to a changed effective time a photon needs to leave the fiber. This explains the small strain sensitivity of the fluorescence lifetime as observed in [Col02].

The connection of the steady state intensity $I(\infty)$ to other variables will be subject of chapter 4.

3.2 Experimental Results

The setup used for measuring the fluorescence lifetime is depicted in figure 3.2. A 980 nm laserdiode excites a 5 mm long Ytterbium doped fiber. The length of the fiber is limited due to the physical properties of the intended mounting place. The fluorescence intensity near 1040 nm is filtered and measured using a photodiode, a fourth order besssel lowpass with a cut off frequency of 20 kHz and a 192 kHz/24 bit analog to digital converter. The excitation light intensity is measured by a second reference photodiode.

For validation of the formulas derived in section 3.1, three measurements of fluorescence decay were made at room temperature with differing excitation powers from 15 mW to 30 mW. The laser diode was switched off after 50 ms of constant excitement (i.e. u_v forms a 10 Hz square wave). After that, the resulting decay of fluorescence was tracked and fitted with equation (3.44) and both simplifications (3.45) and (3.46) using the nonlinear least squares fitting method for implicit functions explained in [Mat09]. The results for the fluorescence decay are plotted in figure 3.3 along with the fittings.

The exponential fit (3.46) shows poor agreement with the measurement, the semiexponential (3.45) and the original function (3.44) are almost indistinguishable. The assumptions made for equation (3.44) seem to be fulfilled and the equation describes the fluorescence decay very precisely for every excitation power.

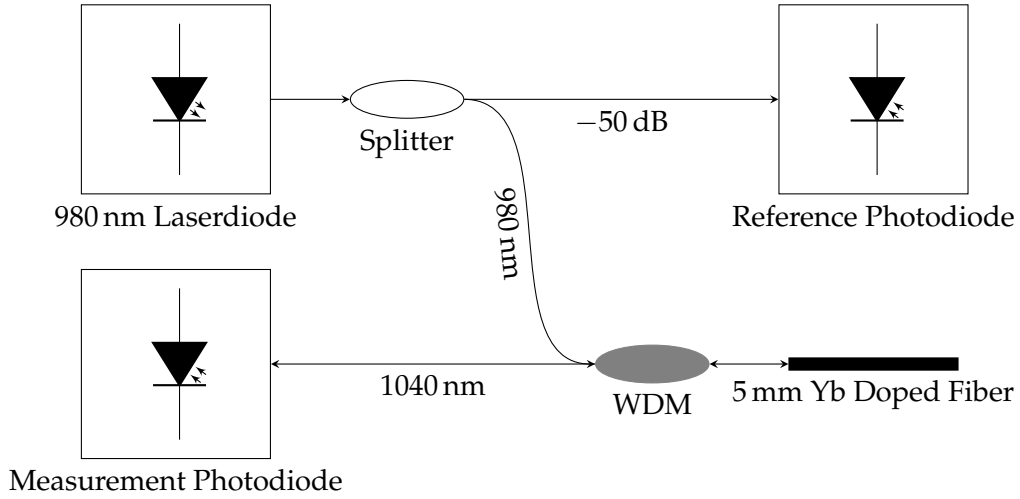


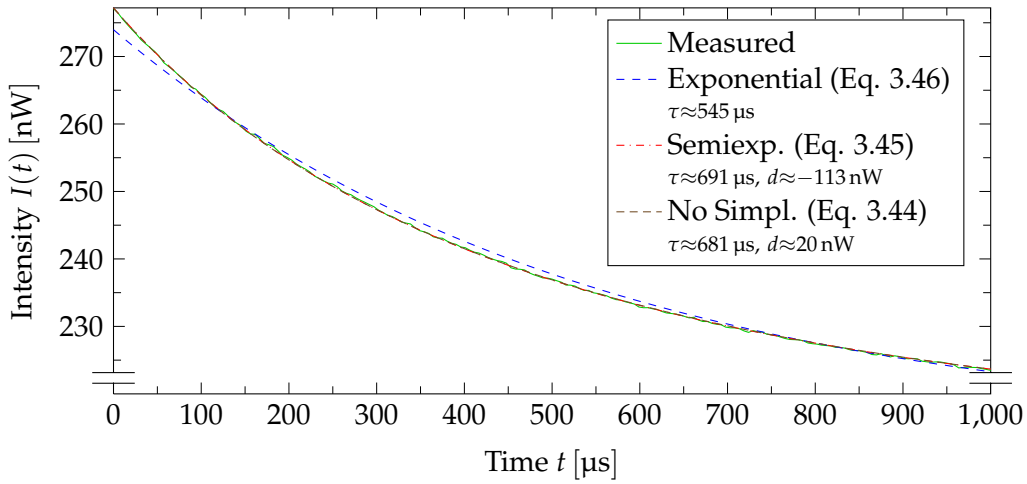
Figure 3.2: The used setup for measuring the fluorescence lifetime. WDM stands for Wavelength Division Multiplexing and is used to filter and split the signal. The photodiodes are monitored by a 192 kHz/24 bit analog to digital converter after their signal has been filtered by a 20 kHz fourth order bessel lowpass [Ley10]. Due to the short measurement duration, the environmental conditions (e.g. temperature) are assumed to stay constant.

The fitting constant of interest is the lifetime τ . Especially important is its sensitivity to the excitation power. In an ideal case, τ should be completely independent of the excitation power. The lowest experimentally derived standard deviation of τ over excitation power is reached for the fitting approach based on equation (3.44) (as shown in in figure 3.4) and is 3.43 μs . Accordingly the expected accuracy of the lifetime τ determined by the standard deviation over excitation is in the order of

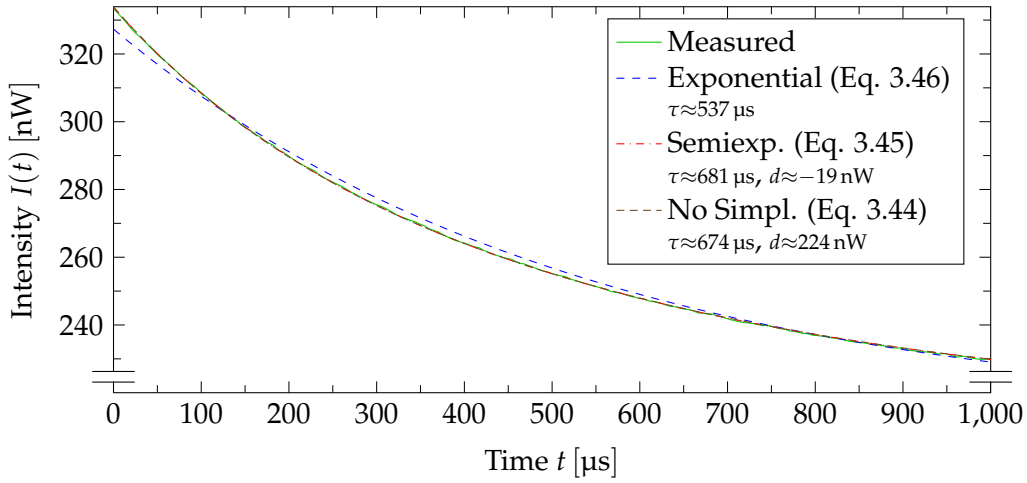
$$[\Delta\tau] \approx 4 \mu\text{s}. \quad (3.47)$$

The reasons for this variance may be the instability of the implicit nonlinear fitting used, because four degrees of freedom (τ , d , $I(0)$ and $I(\infty)$) need to be determined. An alternative explanation is the varying noise excitation $u_v(t)$ of the fiber during the power off phase of the laser diode (i.e. a differing $I(\infty)$). While the latter may be avoided using a more sophisticated setup, the former is caused by mathematical limitations. Thus the instability of the implicit nonlinear fitting represents lower boundary for the accuracy of the system.

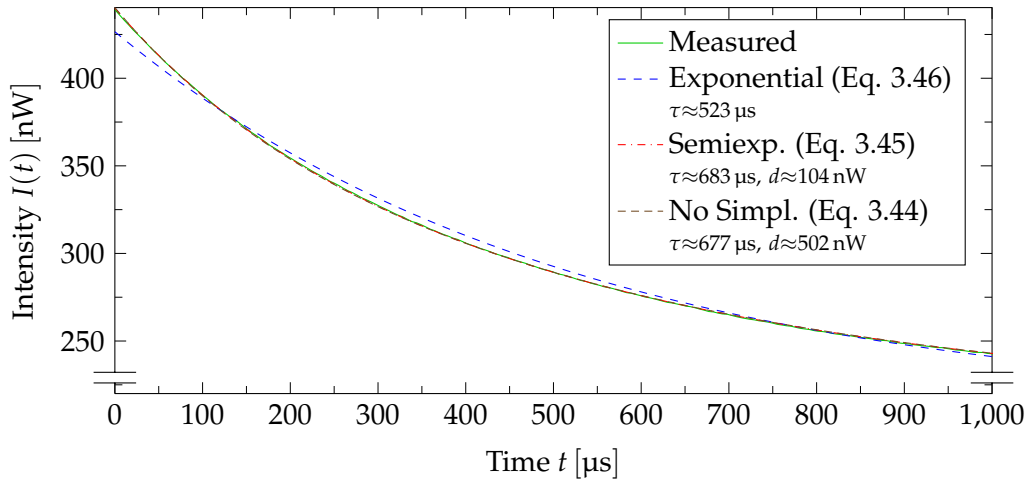
The worst case for the influence of noise regarding measurements are weak excitations, e.g. due to strong bending of the transmitting fiber. To calculate an estimation of the worst case lower boundary for the accuracy of τ , the fitting of equation (3.44) to the low excitation measurement is used as a perfect reference measurement $R_0(t)$ (figure 3.3a). Equation (3.44) is used, because it showed the most robust behavior in the previous measurements (see figure 3.4). The low excitation measurement is used



(a) Low excitation of 15 mW.



(b) Medium excitation of 20 mW.



(c) High excitation of 30 mW.

Figure 3.3: The decay of the Ytterbium fluorescence intensity after turning off the exciting laser diode for different excitation powers and different fitting equations. Almost no difference between the fittings based on (3.45) or (3.44) and the measurement can be observed while the exponential fitting (3.46) does not fit correctly in all cases.

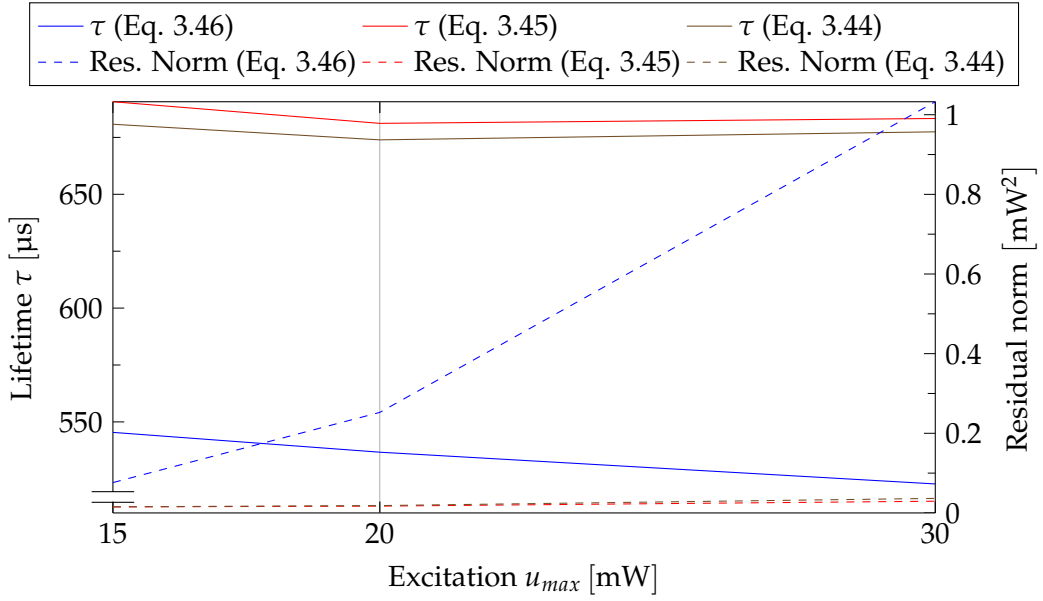


Figure 3.4: The sensivity of the lifetime τ plotted against different excitations and fitting variants together with the corresponding squared error between fitting and dataset. The lifetime τ of the exponential fitting (eq. 3.46) has a standard deviation of $11.43 \mu\text{s}$ over the excitations, the semiexponential (eq. 3.45) has $4.98 \mu\text{s}$ and no simplification (eq. 3.44) varies with a standard deviation of $3.43 \mu\text{s}$. Thus the biggest robustness is expected from the fitting according to equation 3.44 although the fitting error is almost negligible for both fittings from equation 3.45 and equation 3.44. The exponential fit (eq. 3.46) shows a poor error performance but a quite stable lifetime estimation.

to simulate a worst case. White Gaussian noise $\mathcal{N}(0, \sigma^2)$ is added with a variance σ^2 based on the variance measured for $I(t)$ where $t \gg 1 \text{ ms}$. Note that the measurement noise is primarily caused by the shot noise of the photodiode, which cannot be reduced with a better circuit or cooling. Thus a simulated set $R_i(t)$ of perfect measurements only influenced by measurement noise is created based on the perfect reference measurement $R_0(t)$ and the added simulated noise $\mathcal{N}(0, \sigma^2)$

$$\sigma^2 \approx \text{Var}(I(t \gg 1 \text{ ms})) \approx 0.01 \text{ nW}^2 \quad (3.48)$$

$$R_i(t) = R_0(t) + \mathcal{N}(0, \sigma^2), \quad (3.49)$$

where $i \geq 1$ is the index of the generated simulated measurement. Then the corresponding lifetime τ_i was determined for each simulated measurement. The result for 100 simulated measurements is shown in figure 3.5. Ideally τ_i should not vary over the simulated measurements, but obviously it does with a standard deviation of about

$$\Delta\tau_{sim} \approx 3.9 \mu\text{s}. \quad (3.50)$$

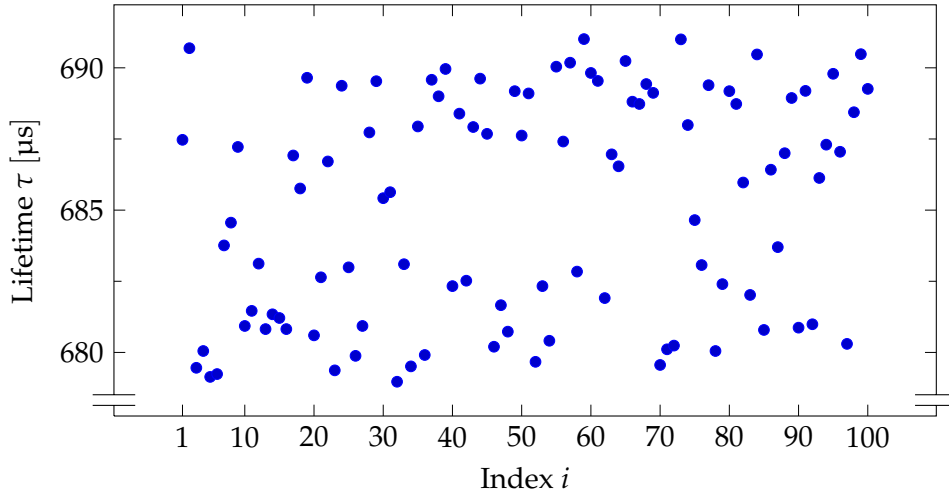


Figure 3.5: The sensitivity of the lifetime τ over different simulated measurements $R_i(t) = R_0(t) + \mathcal{N}(0, \text{Var}(I(t \gg 1 \text{ ms})))$ for a fitting based on equation (3.44). The standard deviation of the lifetime is $3.9 \mu\text{s}$.

Since this variation is only due to the sensitivity of the fitting algorithm to the unavoidable measurement noise, it can be seen as an estimated lower boundary for the accuracy of the lifetime. This is in good accordance with the measured accuracy of $\Delta\tau \approx 4 \mu\text{s}$.

[Sun98] created a model for Ytterbium fluorescence lifetimes over temperature. Although the model is based on exponential decays, the order of magnitude for the lifetime sensitivity can be expected to be applicable in this work as well. Figure 3.6 shows the behavior of the fluorescence lifetime over temperature for different doping concentrations in the temperature region important for this work. Based on this model, the best case sensitivity is about

$$\frac{\Delta\tau}{\Delta T} \approx 250 \frac{\text{ns}}{\text{K}}. \quad (3.51)$$

This corresponds to a lower boundary sensitivity for the system in this work of

$$\Delta T_{\min} \approx \frac{3.9 \mu\text{s}}{250 \frac{\text{ns}}{\text{K}}} = 15.6 \text{ K}. \quad (3.52)$$

In reality, the sensitivity is probably even worse, although the lower boundary sensitivity is already far away from any satisfying value.

In summary, the temperature measurement based on fluorescence lifetime needs a very well defined environment with very stable power off excitations. The high quantity of degrees of freedom for the fitting function decreases the robustness of the system. Therefore the constraints with respect to noise are tough and hard to fulfill for

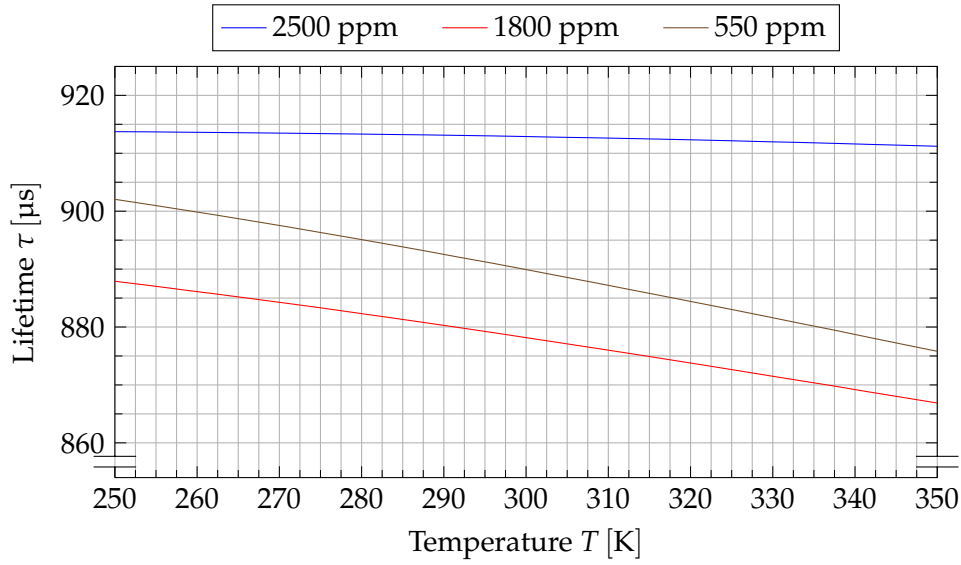


Figure 3.6: The sensivity of the fluorescence lifetime over temperature according to [Sun98] for different dopings of Ytterbium doped fibers.

short length fibers with weak fluorescence intensities due to shot noise. Fitting functions with less degrees of freedom (e.g. a pure exponential decay) show poor agreement with the measured decay. Most of the more sophisticated (and maybe more robust) fitting algorithms, e.g. based on phase shifts in Fourier domain, cannot be used as the system is not a linear time invariant system. Normal gradient descent (or similar) algorithms are slow and computationally expensive.

Thus, the system is not very well suited for fast and robust temperature measurements based on fluorescence lifetime with high accuracy. However, measurements in very high temperature regions are possible, where the low absolute accuracy may still suffice the requirements and the lifetime sensitivity is intrinsically much higher [Sun98].

4 Fluorescence Spectrum

Both the emission and the absorption spectra of fluorescent materials vary with temperature. In case of an ideal two level system, the fluorescence is created by the emission of photons during the transition of excited electrons from the second energy level to the ground energy level (compare to figure 2.3b). This transition can happen spontaneously or stimulated by another photon (compare to figure 3.1). Each emitted photon can also cause a stimulated emission of another photon. This process of self stimulated emission is called *amplified spontaneous emission*. Electrons in the ground energy level can absorb previously emitted photons and change to the second energy level. This process is called *reabsorption*. Additionally photons emitted from an external input source are absorbed or cause stimulated emissions. All these processes cause various transitions of electrons between the two energy levels. Each transition changes the probability of a photon getting absorbed or emitted as the amount of electrons in the ground or second energy level changes. Thus the rate of transitions varies over time until the same amount of electrons decay from the second to the ground energy level as electrons are excited from the ground energy level to the second energy level. In this case, the distribution of electrons among the two energy levels stays constant. The (time constant) measured spectrum is the result of the emission in this steady state.

4.1 Calculation and Dependencies

Just like in chapter 3, it is assumed that the excitation is relatively constant along the fiber. According to equation (3.43), the emission intensity of the steady state system is equal to

$$\begin{aligned}
 I(\infty) = f - d &= \frac{\int_0^\infty \frac{\tilde{u}_{v,T} + \frac{a_v}{\sigma_v}}{\Delta \tilde{f}_v} d\nu}{\int_0^\infty \frac{\sigma_v \tilde{u}_{v,T} + a_v k_v}{\sigma_v^2 \Delta \tilde{f}_v^2} d\nu} \cdot \int_0^\infty E_v \frac{\sigma_v \tilde{u}_{v,T} + a_v k_v}{\sigma_v^2 \Delta \tilde{f}_v} d\nu - \int_0^\infty E_v \frac{a_v}{\sigma_v} d\nu \\
 &= \int_0^\infty E_v \left[\frac{\int_0^\infty \frac{\tilde{u}_{v,T} + \frac{a_v}{\sigma_v}}{\Delta \tilde{f}_v} d\nu}{\int_0^\infty \frac{\sigma_v \tilde{u}_{v,T} + a_v k_v}{\sigma_v^2 \Delta \tilde{f}_v^2} d\nu} \cdot \frac{\sigma_v \tilde{u}_{v,T} + a_v k_v}{\sigma_v^2 \Delta \tilde{f}_v} - \frac{a_v}{\sigma_v} \right] d\nu. \quad (4.1)
 \end{aligned}$$

This result is compared to equation (3.9) evaluated for $t \rightarrow \infty$

$$I(\infty) = \int_0^\infty E_\nu g_\nu(\infty) d\nu. \quad (4.2)$$

As both equations must hold for every possible E_ν , it directly follows for the steady state fluorescence density spectrum that

$$\gamma(\tilde{u}_{\nu,T}) = \frac{\int_0^\infty \frac{\tilde{u}_{\nu,T} + \frac{a_\nu}{\sigma_\nu}}{\Delta \tilde{f}_\nu} d\nu}{\int_0^\infty \frac{\tilde{u}_{\nu,T} + \frac{a_\nu}{\sigma_\nu} k_\nu}{\sigma_\nu \Delta \tilde{f}_\nu^2} d\nu} \quad (4.3)$$

$$g_\nu(\infty) = \gamma(\tilde{u}_{\nu,T}) \frac{\tilde{u}_{\nu,T} + \frac{a_\nu}{\sigma_\nu} k_\nu}{\sigma_\nu \Delta \tilde{f}_\nu} - \frac{a_\nu}{\sigma_\nu}, \quad (4.4)$$

where $\gamma(\tilde{u}_{\nu,T})$ is a scale for the excitation of the fiber.

The thermal radiation $B_\nu(T)$ is defined as the radiation that occurs in *thermodynamic* equilibrium without excitation. No energy is emitted or absorbed in thermodynamic equilibrium meaning that no emission or absorption effects can occur, i.e. $\dot{N}_{2,\nu}(\infty) = 0$ for all frequencies ν . For the thermal radiation holds (compare to (3.10))

$$g_\nu(\infty)|_{u_\nu(\infty)=0} = B_\nu(T) - \Delta \tilde{f}_\nu \cdot \dot{N}_{2,\nu}(\infty) = B_\nu(T), \quad (4.5)$$

with $\dot{N}_{2,\nu}(\infty) = 0$.

An equation system can be constructed by using all known formulas for $g_\nu(\infty)$ based on equations (3.10) and (3.12) as well as equation (4.4) for the normal case and the thermodynamic equilibrium case (i.e. $u_\nu(\infty) = 0$ and $g_\nu(\infty) = B_\nu(T)$)

$$g_\nu(\infty) = \gamma(\tilde{u}_{\nu,T}) \frac{\tilde{u}_{\nu,T} + \frac{a_\nu}{\sigma_\nu} k_\nu}{\sigma_\nu \Delta \tilde{f}_\nu} - \frac{a_\nu}{\sigma_\nu} \quad (4.6)$$

$$B_\nu(T) = \gamma(B_\nu(T)) \frac{B_\nu(T) + \frac{a_\nu}{\sigma_\nu} k_\nu}{\sigma_\nu \Delta \tilde{f}_\nu} - \frac{a_\nu}{\sigma_\nu} \quad (4.7)$$

$$g_\nu(\infty) = \tilde{u}_{\nu,T} + \Delta \tilde{f}_\nu [\sigma_\nu N_2(\infty) - v_\nu \sigma_{a,\nu} N] g_\nu(\infty) + \Delta \tilde{f}_\nu a_\nu N_2(\infty) \quad (4.8)$$

$$B_\nu(T) = B_\nu(T) + \Delta \tilde{f}_\nu [\sigma_\nu N_{2,0}(\infty) - v_\nu \sigma_{a,\nu} N] B_\nu(T) + \Delta \tilde{f}_\nu a_\nu N_{2,0}(\infty). \quad (4.9)$$

$N_{2,0}(\infty)$ is the upper level population density in case of thermodynamic equilibrium.

Some tedious, but straightforward further computations yield four different equations

$$N_{eff} = \frac{k_\nu}{\Delta \tilde{t}_\nu \sigma_\nu} = \frac{1}{\gamma(\tilde{u}_{\nu,T})} + N_2(\infty) = \frac{1}{\gamma(B_\nu(T))} + N_{2,0}(\infty) \quad (4.10)$$

$$\tilde{\sigma}_\nu = \frac{\sigma_{a,\nu}}{\sigma_{a,\nu} + \sigma_{e,\nu}} \quad (4.11)$$

$$B_\nu(T) = \frac{\frac{a_\nu}{v_\nu} N_{2,0}(\infty)}{\sigma_{a,\nu} N_{1,0}(\infty) - \sigma_{e,\nu} N_{2,0}(\infty)} \quad (4.12)$$

$$g_\nu(\infty) = u_\nu \frac{1 - \tilde{\sigma}_\nu \frac{N}{N_{eff}}}{1 - \frac{N_2(\infty)}{N_{eff}}} + B_\nu(T) \left[1 + \tilde{\sigma}_\nu \frac{N}{N_{eff}} \frac{\frac{N_2(\infty)}{N_{2,0}(\infty)} - 1}{1 - \frac{N_2(\infty)}{N_{eff}}} \right]. \quad (4.13)$$

Notable properties derived from equation (4.10) are $N_{eff} > N_2(\infty) \geq N_{2,0}(\infty)$ and $N_{eff} > \tilde{\sigma}_\nu N$.

It is clear from equation (4.13), that the measured spectrum will depend on the population density $N_2(\infty)$ and, accordingly, the excitation photon density u_ν . N_{eff} , $N_{2,0}(\infty)$, N and $\tilde{\sigma}_\nu$ are constant over the excitation photon density u_ν . Considering high excitation photon densities, i.e. $N_2(\infty)$ is large compared to $N_{2,0}(\infty) \frac{N_{eff} + \tilde{\sigma}_\nu N}{N_{2,0}(\infty) + \tilde{\sigma}_\nu N}$, and regions where the excitation does not overlay the measurement, i.e. $u_\nu = 0$, equation (4.13) can be approximated by

$$g_\nu(\infty) \approx B_\nu(T) \tilde{\sigma}_\nu \frac{N}{N_{eff}} \frac{\frac{N_2(\infty)}{N_{2,0}(\infty)} - 1}{1 - \frac{N_2(\infty)}{N_{eff}}} \propto B_\nu(T) \tilde{\sigma}_\nu. \quad (4.14)$$

The empirical explanation that the condition of high excitations can be fulfilled in the scope of this work is the observation that the fluorescence power of the excited material is significantly stronger than the thermal radiation power. For $u_\nu = 0$, $g_\nu(\infty) \gg B_\nu(T)$ is fulfilled, if equation (4.14) is fulfilled (compare to equation (4.13)). Therefore, the spectrum reaches a shape independent from the excitation for large excitations. If a large excitation can be guaranteed, the insensitivity of the shape might suffice to track the temperature dependence of the spectrum with adequate accurateness. Note however, that this condition might be a problem for certain application areas. In the following, a detailed analysis of what can be measured in cases of high excitation is presented.

According to McCumber [McC64], the following relation holds

$$\frac{\sigma_{e,\nu}}{\sigma_{a,\nu}} = \frac{N_{1,0}}{N_{2,0}} \exp\left(-\frac{h\nu}{k_B T}\right) = \exp\left(\frac{h[\nu_z - \nu]}{k_B T}\right). \quad (4.15)$$

The McCumber relation is a consequence of the temperature dependent population of the two energy levels and their sublevels. ν_z is called *zero-line frequency* and describes the frequency where $\sigma_{e,\nu} = \sigma_{a,\nu}$. A more detailed explanation is beyond the scope of this thesis, but can be found in [McC64]. In case of Ytterbium, the zero-line frequency

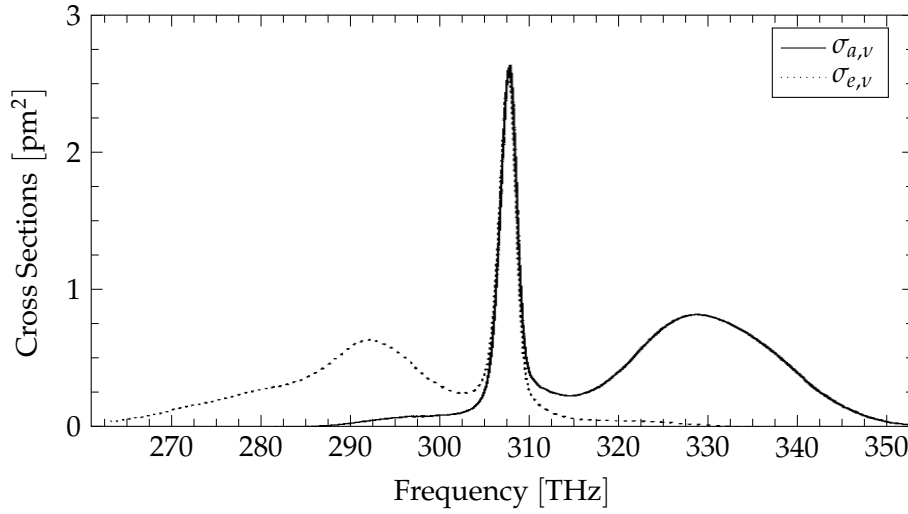


Figure 4.1: The emission and absorption cross sections, i.e. $\sigma_{e,\nu}$ and $\sigma_{a,\nu}$, of Ytterbium in germanosilicate glass as measured in [Pas97].

is normally located near the transition with the highest energy, i.e. $\nu_z \approx \frac{c}{977\text{ nm}} = 307\text{ THz}$ (compare to figure 4.1). Using the McCumber relation in the formulas (4.11) and (4.12) yields

$$\tilde{\sigma}_\nu = \frac{1}{1 + \exp\left(\frac{h[\nu_z - \nu]}{k_B T}\right)} \quad (4.16)$$

$$B_\nu(T) = \frac{\frac{a_\nu}{\nu_\nu \sigma_{e,\nu}}}{\exp\left(\frac{h\nu}{k_B T}\right) - 1}. \quad (4.17)$$

Note that $B_\nu(T)$ can also be defined based on the thermal radiation of a non-ideal black body in thermodynamic equilibrium. In this case, the generalized Planck's law for the *photon density* $B_\nu(T)$ is used. According to [Sch91], the generalized Planck's law converted to photon density representation is expressed by (neglecting fiber internal reflectivities)

$$\alpha_\nu = 1 - \exp(-\sigma_{a,\nu} N_{1,0}(\infty) L) \approx \sigma_{a,\nu} N_{1,0}(\infty) L \quad \text{if } L \ll \frac{1}{\sigma_{a,\nu} N_{1,0}(\infty)} \quad (4.18)$$

$$B_\nu(T) = \frac{\alpha_\nu \frac{8\pi\nu^2}{v_\nu^3}}{\exp\left(\frac{h\nu}{k_B T}\right) - 1}, \quad (4.19)$$

where α_ν is the absorptance derived using the *Beer–Lambert Law* [Pow98, p. 104] and approximated using the relation $e^x \approx 1 + x$ for $|x| \ll 1$. L is the effective length (a mean length over all directions) of the fiber which is assumed to be short. A compari-

son of equations (4.17) and (4.19) followed by using equation (4.15) yields

$$\frac{a_\nu}{v_\nu \sigma_{e,\nu}} = \sigma_{a,\nu} \frac{8\pi N_{1,0}(\infty) L \nu^2}{v_\nu^3} = \sigma_{e,\nu} \frac{8\pi N_{1,0}(\infty) L \nu^2}{v_\nu^3} \exp\left(\frac{h[\nu - \nu_z]}{k_B T}\right). \quad (4.20)$$

Resolving for $\sigma_{e,\nu}$ yields

$$\sigma_{e,\nu} = \sqrt{a_\nu} \frac{v_\nu}{\sqrt{8\pi N_{1,0}(\infty) L \nu^2}} \exp\left(\frac{h[\nu_z - \nu]}{2k_B T}\right). \quad (4.21)$$

Therefore, combined with equations (4.16) and (4.17), the overall fluorescence photon density under high excitation is

$$f_{\sigma_{a,\nu}}(T) = \frac{\frac{8\pi N_{1,0}(\infty) L \nu^2}{v_\nu^3}}{\left[1 + \exp\left(\frac{h[\nu_z - \nu]}{k_B T}\right)\right] \left[\exp\left(\frac{h\nu}{k_B T}\right) - 1\right]} \quad (4.22)$$

$$f_{\sigma_{e,\nu}}(T) = \frac{\frac{8\pi N_{1,0}(\infty) L \nu^2}{v_\nu^3} \exp\left(-\frac{h\nu_z}{k_B T}\right)}{\left[1 + \exp\left(\frac{h[\nu_z - \nu]}{k_B T}\right)\right] \left[1 - \exp\left(-\frac{h\nu}{k_B T}\right)\right]} \quad (4.23)$$

$$f_{\sqrt{a_\nu}}(T) = \frac{\frac{\sqrt{8\pi N_{1,0}(\infty) L \nu^2}}{v_\nu^2} \exp\left(-\frac{h\nu_z}{2k_B T}\right)}{\left[1 + \exp\left(\frac{h[\nu_z - \nu]}{k_B T}\right)\right] \left[\exp\left(\frac{h\nu}{2k_B T}\right) - \exp\left(-\frac{h\nu}{2k_B T}\right)\right]} \quad (4.24)$$

$$g_\nu(\infty) \propto B_\nu(T) \tilde{\sigma}_\nu = f_{\sigma_{a,\nu}}(T) \cdot \sigma_{a,\nu} \quad (4.25)$$

$$= f_{\sigma_{e,\nu}}(T) \cdot \sigma_{e,\nu} \quad (4.26)$$

$$= f_{\sqrt{a_\nu}}(T) \cdot \sqrt{a_\nu}. \quad (4.27)$$

According to equation (3.8), the measured intensity spectrum is

$$I_\nu(\infty) \propto \nu g_\nu(\infty) \propto \nu f_{\{\sigma_{a,\nu}|\sigma_{e,\nu}|\sqrt{a_\nu}\}}(T) \cdot \{\sigma_{a,\nu}|\sigma_{e,\nu}|\sqrt{a_\nu}\}, \quad (4.28)$$

assuming $e_\nu v_\nu$ is constant over frequency. Each function $f(T) = \nu f_{\{\sigma_{a,\nu}|\sigma_{e,\nu}|\sqrt{a_\nu}\}}(T)$ can be approximated using a first order Taylor series

$$f(T) \approx f(T_0)|_{\nu=\nu_z} \cdot \left[1 + \frac{\partial_T f(T)|_{T=T_0}}{f(T_0)} [T - T_0]\right] \cdot \frac{f(T_0)}{f(T_0)|_{\nu=\nu_z}}, \quad (4.29)$$

where $f(T_0)|_{\nu=\nu_z}$ has the function of a constant frequency and is a temperature independent factor. In case $\frac{\partial_T f(T)|_{T=T_0}}{f(T_0)}$ is also frequency independent, the expression $\frac{I_\nu(\infty)}{f(T_0)}$ will be proportional to the corresponding spectrum (i.e. $\sigma_{a,\nu}$, $\sigma_{e,\nu}$ or $\sqrt{a_\nu}$) regardless of the temperature (compare to equation (4.28)). Ideally, $f(T_0)$ can also be assumed to be constant over frequency, in which case $I_\nu(\infty)$ is directly proportional to the corresponding spectrum.

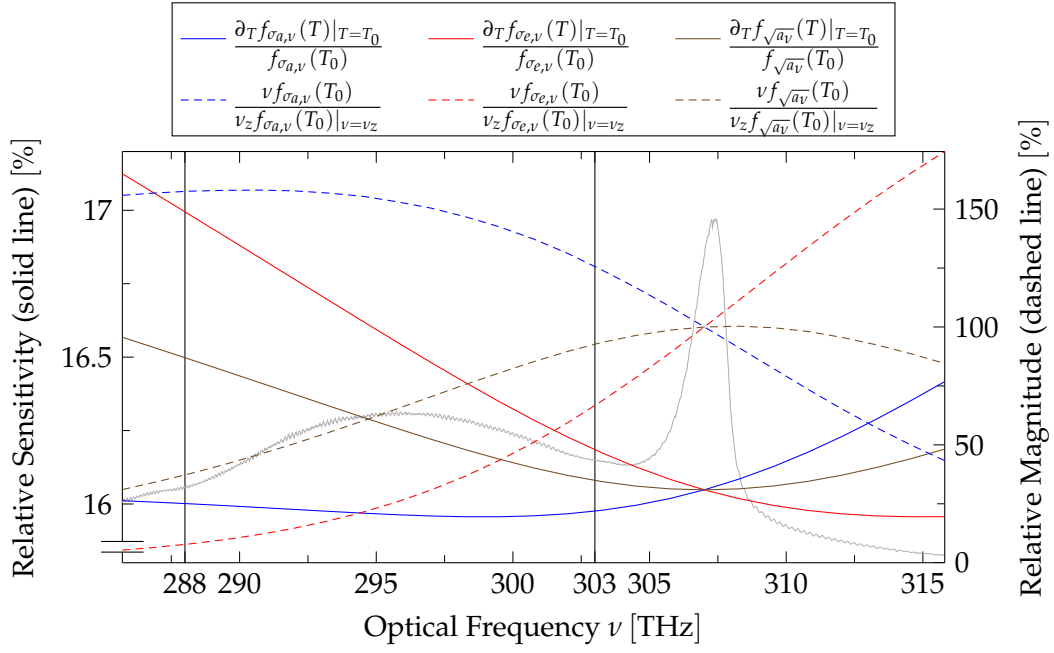


Figure 4.2: The behavior of the factors $\nu f_{\sigma_{a,\nu}}(T)$, $\nu f_{\sigma_{e,\nu}}(T)$ and $\nu f_{\sqrt{a_\nu}}(T)$ over temperature and frequency evaluated at $T_0 = 303$ K and assuming a frequency independent v_ν (refer to equations (4.22) till (4.29)). The background shows a logarithmic example measurement $I_\nu(\infty)$ of the spectrum. The temperature sensitivity in the minor peak region between 288 THz and 303 THz is stable over frequency, if it is referenced to the absorption spectrum $\sigma_{a,\nu}$. Consequentially $\frac{I_\nu(\infty)}{\nu f_{\sigma_{a,\nu}}(T_0)} \propto \sigma_{a,\nu}$ holds in this region regardless of the temperature. Since $\nu f_{\sigma_{a,\nu}}(T_0)$ shows relatively good frequency stability as well, the assumption $I_\nu(\infty) \propto \sigma_{a,\nu}$ can be used for applications with smaller accuracy needs. For a connection between $I_\nu(\infty)^2$ and a_ν , $\nu f_{\sqrt{a_\nu}}(T)$ must be squared and $\partial_T f_{\sqrt{a_\nu}}(T)$ doubled decreasing the stability over frequencies.

According to figure 4.2,

$$\frac{I_\nu(\infty)}{\nu f_{\sigma_{a,\nu}}(T_0)} \propto \sigma_{a,\nu} \quad (4.30)$$

is fulfilled in the region of the minor emission peak. Tests showed, that using the approximation

$$I_\nu(\infty) \propto \sigma_{a,\nu} \quad (4.31)$$

does not decrease the reachable accuracy significantly as $\nu f_{\sigma_{a,\nu}}(T_0)$ is approximately constant over the frequency in the analyzed region. Consequentially, this approximation will be used in the following for the sake of convenience.

To sum up, the steady state emission spectrum of an Ytterbium doped fiber under high excitation in the wavelength range $990 \text{ nm} < \lambda < 1040 \text{ nm}$ or, equivalently, the

frequency range

$$288 \text{ THz} < \nu < 303 \text{ THz} \quad (4.32)$$

of the minor emission peak is approximately directly proportional to the absorption spectrum $\sigma_{a,\nu}$. This observation is contrary to the intuitive assumption, that the measured spectrum roughly corresponds to the spontaneous emission (although all spectra still have similar properties). There are no significant temperature effects changing the proportionality to the absorption spectrum in this region. Accordingly, measured temperature effects will be a direct result of the temperature effects of the absorption spectrum itself reducing the complexity for temperature sensing. The temperature effects of the absorption spectrum are discussed in the next chapter.

As a remark, the overall measured spectrum exhibits more than just the temperature dependence of the absorption spectrum. It has been shown in figure 4.2, that the shape of the spectrum also changes with temperature according to $\nu f_{\sigma_{a,\nu}}(T)$. With a stable normalization of the spectrum, this additional temperature effect could be used to improve the temperature measurement. The underlying mechanism, however, is rather complex as at least two temperature dependent effects influence each other (the changes caused by $\nu f_{\sigma_{a,\nu}}(T)$ and the temperature dependent change of the absorption spectrum). In addition, the stable normalization is another problem to solve and the correct measurement of the entire spectrum (especially of the main peak) exhibits certain problems as can be seen in figure 4.4. This is why this work focuses on the minor peak, that shows temperature effects primarily caused by the absorption spectrum.

4.2 Temperature Dependence of the Absorption Spectrum

Several effects influence the absorption spectrum. In this work, the two-level assumption is used (see section 3.1), i.e. the system is believed to consist of only two energy levels with different transitions. In reality, each energy level will consist of multiple sublevels (compare to figure 2.3b). Sublevels are able to interchange electrons to a certain extent without the need for external excitation. If the temperature is increased, the higher sublevels will get more densely populated. Consequentially, transitions starting from higher sublevels will increase while transitions starting from lower sublevels will decrease. Normally this causes a shift of the emission spectrum towards higher frequencies. This effect is modeled by the McCumber relation in equation 4.15 that has already been used for the formulas derived.

A second effect is the spectral line broadening. Several reasons exist for the broadening of spectra, most of them are well analyzed for gas spectra [Dem11]. A detailed analysis is beyond the scope of this thesis. One intuitive example for spectral broad-

ening is *Doppler Broadening*, caused by the temperature dependent movement of electrons. If an electron emits a photon, the frequency of the photon will be shifted according to the movement of the electron following the principle of the Doppler effect. The higher the temperature, the faster the electrons will move, the stronger the frequency bandwidth of emitted photons will be. However, *Doppler Broadening* is mainly observed in gases.

Two main categories exist, the *inhomogeneous broadening* and the *homogeneous broadening*. Inhomogeneous broadening is observed if each single atom shows different emission probabilities (e.g. because they have different velocities like for Doppler broadening). Homogeneous broadening describes effects that have equal probabilities for all atoms. An effect of the former category is usually modeled by a convolution of the spectrum with a *Gaussian* filter, the latter by a convolution with a *Lorentzian* filter [Dem11].

A Gaussian filter kernel is defined by

$$s_G(\nu) \propto \exp\left(-\pi^2 \frac{\nu^2}{\theta}\right) \quad (4.33)$$

with $\sqrt{\theta}$ being proportional to the bandwidth.

A Lorentzian kernel is represented by

$$s_L(\nu) \propto \frac{1}{1 + 4\pi^2 \frac{\nu^2}{\gamma^2}}, \quad (4.34)$$

where γ is proportional to the bandwidth.

A convolution is equal to a multiplication in Fourier domain. As every broadening effect is represented by a convolution of one of the above functions with the spectrum, the total broadening can be described by a multiplication of all Fourier domain kernels contributing to the broadening. The Fourier transformation from ν to t_ν yields for the broadening kernels

$$S_G(t_\nu) \propto \exp(-\theta t_\nu^2) \quad (4.35)$$

$$S_L(t_\nu) \propto \exp(-\gamma |t_\nu|). \quad (4.36)$$

t_ν describes a frequency over the optical frequency ν (which is basically a time). For easier discrimination, t_ν will be called Fourier frequency in the following. The overall broadening in Fourier domain caused by different effects is consequentially

$$S'(t_\nu) = \prod_k S_{L,k}(t_\nu) \prod_i S_{G,i}(t_\nu) \propto \exp\left(-\sum_k \gamma_k |t_\nu| - \sum_i \theta_i t_\nu^2\right). \quad (4.37)$$

Additionally, a spectral shift might occur, e.g. due to an energy shift between the two energy levels or due to pressure broadening. All individual shifts will add up to a single spectral shift $\frac{\Delta\nu}{2\pi}$. A spectral shift in optical frequency domain is expressed by using a phase shift in Fourier frequency domain. The overall spectral change $S(t_\nu)$ is therefore modeled using

$$\Gamma = \sum_k \gamma_k \quad (4.38)$$

$$\Theta = \sum_i \theta_i \quad (4.39)$$

$$S(t_\nu) = S'(t_\nu) \exp(-i\Delta\nu t_\nu) \propto \exp(-\Gamma|t_\nu| - \Theta t_\nu^2 - i\Delta\nu t_\nu). \quad (4.40)$$

Most known thermal spectral changes exhibit a temperature dependency of the broadening bandwidths (γ respectively $\sqrt{\theta}$) or spectral shift that has the form of a power function. The sums of the power functions (i.e. Γ , Θ and $\Delta\nu$) form polynomial functions. The sum of the three polynomials will again form a polynomial. Thus the overall thermal change $S(t_\nu, T)$ can be written in terms of a polynomial function with temperature independent coefficients

$$S(t_\nu, T) = C(T) \exp\left(-\sum_{p=1}^P [\Gamma_p |t_\nu| + \Theta_p t_\nu^2 + i\Delta\nu_p t_\nu] T^{\frac{p}{K}}\right), \quad (4.41)$$

in which K defines the stepsize, P the degree of the polynomial and $C(T)$ some scaling coefficient. Note that the exact polynomial coefficients depend (amongst others) on the material and the structure of the material, which is why they are assumed to be unknown in the following.

Considering the absorption spectrum $\sigma_{a,\nu}(T)$ in Fourier domain at a specific temperature T

$$\sigma_{a,\nu}(T) \circ \bullet \Sigma_{a,t_\nu}(T) \quad (4.42)$$

the Fourier absorption spectrum $\Sigma_{a,t_\nu}(T)$ consists of a multiplication of the zero temperature spectrum with the thermal change

$$\begin{aligned} \Sigma_{a,t_\nu}(T) &= S(t_\nu, T) \cdot \Sigma_{a,t_\nu}(0) \\ &= C(T) \Sigma_{a,t_\nu}(0) \exp\left(-\sum_{p=1}^P [\Gamma_p |t_\nu| + \Theta_p t_\nu^2 + i\Delta\nu_p t_\nu] T^{\frac{p}{K}}\right). \end{aligned} \quad (4.43)$$

Note that

$$\Sigma_{a,t_\nu=0}(T) = C(T) \Sigma_{a,t_\nu=0}(0) \quad (4.44)$$

holds, such that the temperature dependent coefficient $C(T)$ can be substituted

$$\frac{\Sigma_{a,t_\nu}(T)}{\Sigma_{a,t_\nu=0}(T)} = \frac{\Sigma_{a,t_\nu}(0)}{\Sigma_{a,t_\nu=0}(0)} \cdot \exp \left(- \sum_{p=1}^P [\Gamma_p |t_\nu| + \Theta_p t_\nu^2 + i\Delta\nu_p t_\nu] T^{\frac{p}{k}} \right). \quad (4.45)$$

Due to the normalization with $\frac{1}{\Sigma_{a,t_\nu=0}(T)}$, it is not important whether the absorption spectrum $\sigma_{a,\nu}(T)$ itself is used for the calculation or just some spectrum proportional to the absorption spectrum, e.g. $I_\nu(\infty)$ from equation (4.31).

To be able to measure the temperature, at least two measurements corresponding to different Fourier frequencies t_ν are needed (one for normalization and one for the measurement itself), where one frequency is normally $t_\nu = 0$. A direct approach is the use of *Fourier Transform Infrared Spectroscopy* (FTIR) [Gri07]. FTIR directly measures the Fourier response of the spectrum using a Michelson interferometer. This setup would be rather complex for verification of spectrum based temperature measurement and selecting specific wavelength ranges for the measurement is difficult. This is why a regular spectrum analyzer is used in this work and a Fourier transform is performed in software.

Another idea is based on the optical frequency domain. Two measurements are done. One where the amplitudes of high Fourier frequencies are dominant. The other over the full range to catch the zero Fourier frequency component $\Sigma_{a,t_\nu=0}(T)$ or alternatively where weak Fourier frequencies dominate. This is equivalent to the *Fluorescence Intensity Ratio* (FIR) approach already introduced in section 2.2.

Both approaches will be discussed in reverse order the following.

4.2.1 Fluorescence Intensity Ratio (FIR)

The Fluorescence Intensity Ratio is based on the ratio of two measurements [Bax96]. According to equations (3.9) and (4.31) the two measurements can be denoted by

$$I_0(\infty, T) = \int_{-\infty}^{\infty} h_0(\nu) \sigma_{a,\nu}(T) d\nu \quad (4.46)$$

$$I_1(\infty, T) = \int_{-\infty}^{\infty} h_1(\nu) \sigma_{a,\nu}(T) d\nu, \quad (4.47)$$

with measurement and scaling functions $h_0(\nu)$ and $h_1(\nu)$. Based on the formula for convolutions evaluated at $\nu = 0$, the convolution-multiplication-identity of Fourier transforms, the inverse transform of Fourier signals evaluated at $\nu = 0$ and the symmetrical properties of phase and amplitude for real Fourier transforms the following

relation holds

$$\begin{aligned}
 \int_{-\infty}^{\infty} h(\nu) \sigma_{a,\nu}(T) d\nu &= (h(-\nu) * \sigma_{a,\nu}(T))(\nu = 0) \\
 &= \int_{-\infty}^{\infty} \Sigma_{a,t_\nu}(T) |H(-t_\nu)| e^{i\varphi_H(-t_\nu)} dt_\nu \\
 &= \int_{-\infty}^{\infty} \Sigma_{a,t_\nu}(T) |H(t_\nu)| e^{-i\varphi_H(t_\nu)} dt_\nu.
 \end{aligned} \tag{4.48}$$

Broad functions $h(\nu)$ result in narrow Fourier transforms $H(t_\nu)$. In the most extreme case, $H(t_\nu)$ will form a dirac function. Thus, assuming a broad function $h_0(\nu)$ yields

$$I_0(\infty, T) \approx \Sigma_{a,t_\nu=0}(T) |H_0(0)|. \tag{4.49}$$

$I_0(\infty, T)$ can be interpreted as the scaled mean value of the absorption spectrum. An alternative method for measuring the mean value $I_0(\infty, T)$ is using a function $h_0(\nu)$, that selects a region of ν where weak Fourier frequencies dominate. However, these regions have weak intensities in most cases.

A good choice for $h_1(\nu)$ is a function selecting a region of ν , where $\sigma_{a,\nu}(T)$ changes significantly with temperature. Additionally, the ratio $\frac{I_1(\infty, T)}{I_0(\infty, T)}$ should be strictly monotonically decreasing with higher temperatures to ensure a unique mapping of ratio and temperature. This is normally the case if only regions with a stronger intensity than the mean value $I_0(\infty, T)$ are selected. Higher intensities will broaden towards the mean value with higher temperatures leading to a monotonic decrease. Regions fulfilling these requirements are the peaks of the absorption spectrum $\sigma_{a,\nu}(T)$, i.e. regions of positive amplitudes and high Fourier frequencies.

Therefore another alternative for $h_0(\nu)$ would be a function selecting a region of negative amplitudes (or notches) to get a strong counterpart to $I_1(\infty, T)$ and an increased temperature sensitivity. However, the signal powers of notches are very weak thwarting the advantage of the counterpart effect due to increased noise. Selecting $h_0(\nu)$ as mean value creates the biggest frequency difference between $I_0(\infty, T)$ and $I_1(\infty, T)$ without losing signal power.

The Fluorescence Intensity Ratio is the ratio of both measurements, i.e.

$$\frac{I_1(\infty, T)}{I_0(\infty, T)} \approx \int_{-\infty}^{\infty} \frac{\Sigma_{a,t_\nu}(T)}{\Sigma_{a,t_\nu=0}(T)} \frac{|H_1(t_\nu)|}{|H_0(0)|} e^{-i\varphi_{H_1}(t_\nu)} dt_\nu. \tag{4.50}$$

Inserting equation (4.45) leads to

$$e^{C_0(t_v)} = \frac{\Sigma_{a,t_v}(0)}{\Sigma_{a,t_v=0}(0)} \frac{|H_1(t_v)|}{|H_0(0)|} e^{-i\varphi_{H_1}(t_v)} \quad (4.51)$$

$$C_p(t_v) = -\Gamma_p |t_v| - \Theta_p t_v^2 - i\Delta\nu_p t_v \quad \text{for } p \geq 1 \quad (4.52)$$

$$\frac{I_1(\infty, T)}{I_0(\infty, T)} \approx \int_{-\infty}^{\infty} e^{C_0(t_v)} e^{\sum_{p=1}^P C_p(t_v) T^{\frac{p}{K}}} dt_v = \int_{-\infty}^{\infty} e^{\sum_{p=0}^P C_p(t_v) T^{\frac{p}{K}}} dt_v \quad (4.53)$$

with some temperature independent complex constants $C_p(t_v)$.

Using the definition of an exponential function

$$e^x = \lim_{M \rightarrow \infty} \sum_{m=0}^M \frac{x^m}{m!} \quad (4.54)$$

the ratio can be rewritten as

$$\frac{I_1(\infty, T)}{I_0(\infty, T)} \approx \int_{-\infty}^{\infty} \lim_{M \rightarrow \infty} \sum_{m=0}^M \frac{\left[\sum_{p=0}^P C_p(t_v) T^{\frac{p}{K}} \right]^m}{m!} dt_v. \quad (4.55)$$

The m 'th power of a polynomial with degree P is a polynomial with degree mP . The sum of polynomials with maximum degree MP is a polynomial with degree MP . These two observations yield

$$\frac{I_1(\infty, T)}{I_0(\infty, T)} \approx \lim_{M \rightarrow \infty} \sum_{p=0}^{MP} \tilde{C}_p T^{\frac{p}{K}}. \quad (4.56)$$

Note that the integral as well as all measurement functions $H_0(t_v)$ and $H_1(t_v)$ moved into the (real) coefficients \tilde{C}_p . This result is similar to a normal polynomial fit of the ratio $\frac{I_1(\infty, T)}{I_0(\infty, T)}$. However, the approximation (4.56) is based on the convergent approximation (4.54).

Alternatively the equation (4.56) can be expressed in matrix notation for W measurements

$$\underbrace{\begin{pmatrix} \frac{I_1(\infty, T_1)}{I_0(\infty, T_1)} \\ \vdots \\ \frac{I_1(\infty, T_W)}{I_0(\infty, T_W)} \end{pmatrix}}_{\mathbf{I}} = \underbrace{\begin{pmatrix} 1 & T_1^{\frac{1}{K}} & \dots & T_1^{\frac{MP}{K}} \\ \vdots & \vdots & \ddots & \vdots \\ 1 & T_W^{\frac{1}{K}} & \dots & T_W^{\frac{MP}{K}} \end{pmatrix}}_{\mathbf{T}} \underbrace{\begin{pmatrix} \tilde{C}_0 \\ \vdots \\ \tilde{C}_{MP} \end{pmatrix}}_{\tilde{\mathbf{C}}}. \quad (4.57)$$

Therefore the coefficients $\tilde{\mathbf{C}}$ are easily calculated with the pseudoinverse \mathbf{T}^+

$$\tilde{\mathbf{C}} = \mathbf{T}^+ \mathbf{I}. \quad (4.58)$$

The temperature region of interest in this work is between 283 K and 323 K. As this is a quite narrow temperature region, it is assumed that a linear fit, i.e. $MP = 1$ and $K = 1$, approximates the ratio $\frac{I_1(\infty, T)}{I_0(\infty, T)}$ with sufficient accuracy.

There are other possibilities to approximate (4.53) besides equation (4.56), for example using a sum of exponentials based on *Prony's Method*. These possibilities are not covered in this work as the measured ratios are nearly affine (probably due to the small temperature range analyzed) and do not justify more complex approximations.

To summarize, two measurement regions $h_0(\nu)$ and $h_1(\nu)$ generate two intensities $I_0(\infty, T)$ and $I_1(\infty, T)$. $h_0(\nu)$ selects a wide range of frequencies in the region defined by inequation (4.32). $h_1(\nu)$ selects a peak in the same region. As the needed temperature range is small, the behavior of the ratio $\frac{I_1(\infty, T)}{I_0(\infty, T)}$ can be assumed to be sufficiently described by an affine first order term

$$\frac{I_1(\infty, T)}{I_0(\infty, T)} \approx \tilde{C}_0 + \tilde{C}_1 T = \begin{pmatrix} 1 & T \end{pmatrix} \begin{pmatrix} \tilde{C}_0 \\ \tilde{C}_1 \end{pmatrix} \quad (4.59)$$

4.2.2 Fourier Domain Intensity Ratio (FDIR)

The Fourier Domain Intensity Ratio is based on a software Fourier transformation of the absorption spectrum $\Sigma_{a,t_\nu}(T)$. According to equation (4.31), $\Sigma_{a,t_\nu}(T)$ is known by a measurement and discrete Fourier transformation of the output spectrum in the region defined by equation (4.32)

$$\Sigma_{a,t_\nu}(T) \propto \mathcal{F}(I_\nu(\infty))(t_\nu). \quad (4.60)$$

The scaling of the spectrum is not important as it will cancel out. Note that selecting only a certain region of $\sigma_{a,t_\nu}(T)$ (which is unavoidable as $\sigma_{a,t_\nu}(T)$ is proportional to $I_\nu(\infty)$ only for the region defined in equation (4.32)) increases the importance of an appropriate window function. A good window function reduces the resulting distortions of the Fourier transform $\Sigma_{a,t_\nu}(T)$. The best results are obtained by using the *Hamming window*, which is why it was used for selecting the correct part of $I_\nu(\infty)$.

The general temperature dependency of the spectrum is derived in the following. Afterwards, some assumptions are made in order to simplify the system for practical use.

Rewriting equation (4.45) yields

$$e^{C(t_\nu)} = \frac{\Sigma_{a,t_\nu}(0)}{\Sigma_{a,t_\nu=0}(0)} \quad (4.61)$$

$$\ln \left(\frac{\Sigma_{a,t_\nu}(T)}{\Sigma_{a,t_\nu=0}(T)} \right) = C(t_\nu) + \sum_{p=1}^P [-\Gamma_p |t_\nu| - \Theta_p t_\nu^2 - i\Delta\nu_p t_\nu] T^{\frac{p}{k}}. \quad (4.62)$$

Alternatively the equation can be expressed in matrix notation for W measurements and $F + 1$ frequencies with \mathbf{I}_F being the $F \times F$ unity matrix

$$\underbrace{\begin{pmatrix} \ln \left(\frac{\Sigma_{a,t_{v,1}}(T_1)}{\Sigma_{a,t_v=0}(T_1)} \right) & \cdots & \ln \left(\frac{\Sigma_{a,t_{v,F}}(T_1)}{\Sigma_{a,t_v=0}(T_1)} \right) \\ \vdots & \ddots & \vdots \\ \ln \left(\frac{\Sigma_{a,t_{v,1}}(T_W)}{\Sigma_{a,t_v=0}(T_1)} \right) & \cdots & \ln \left(\frac{\Sigma_{a,t_{v,F}}(T_W)}{\Sigma_{a,t_v=0}(T_1)} \right) \end{pmatrix}}_{\Sigma} = \underbrace{\begin{pmatrix} 1 & T_1^{\frac{1}{K}} & \cdots & T_1^{\frac{P}{K}} \\ \vdots & \vdots & \ddots & \vdots \\ 1 & T_W^{\frac{1}{K}} & \cdots & T_W^{\frac{P}{K}} \end{pmatrix}}_{\mathbf{T}} \underbrace{\begin{pmatrix} C(t_{v,1}) & \cdots & C(t_{v,F}) & 0 & 0 & 0 \\ 0 & \cdots & 0 & \Gamma_1 & \Theta_1 & \Delta\nu_1 \\ \vdots & \ddots & \vdots & \vdots & \vdots & \vdots \\ 0 & \cdots & 0 & \Gamma_P & \Theta_P & \Delta\nu_P \end{pmatrix}}_{\mathbf{C}} \underbrace{\begin{pmatrix} \mathbf{I}_F \\ -|t_{v,1}| & \cdots & -|t_{v,F}| \\ -t_{v,1}^2 & \cdots & -t_{v,F}^2 \\ -it_{v,1} & \cdots & -it_{v,F} \end{pmatrix}}_{\mathbf{T}_v} \quad (4.63)$$

For a calibration of the coefficients in \mathbf{C} , the following variables are defined

$$\widetilde{\mathbf{T}}_v = \begin{pmatrix} -|t_{v,1}| & \cdots & -|t_{v,F}| \\ -t_{v,1}^2 & \cdots & -t_{v,F}^2 \\ -it_{v,1} & \cdots & -it_{v,F} \end{pmatrix} \quad (4.64)$$

$$\mathbf{c} = \begin{pmatrix} C(t_{v,1}) & \cdots & C(t_{v,F}) & \Gamma_1 & \Theta_1 & \Delta\nu_1 & \cdots & \Gamma_P & \Theta_P & \Delta\nu_P \end{pmatrix} \quad (4.65)$$

$$\mathbf{D} = \mathbf{T}^+ \Sigma. \quad (4.66)$$

Let $\text{diag}^P(\widetilde{\mathbf{T}}_v)$ denote a block-diagonal matrix, where $\widetilde{\mathbf{T}}_v$ is placed P times along the diagonal. \mathbf{d} is the rowwise vectorized matrix \mathbf{D} (i.e. \mathbf{d} is a row vector). Then, the system can be rewritten as

$$\mathbf{d} = \mathbf{c} \begin{pmatrix} \mathbf{I}_F \\ \text{diag}^P(\widetilde{\mathbf{T}}_v) \end{pmatrix}. \quad (4.67)$$

Therefore the coefficients are calculated using

$$\mathbf{c} = \mathbf{d} \begin{pmatrix} \mathbf{I}_F \\ \text{diag}^P(\widetilde{\mathbf{T}}_v) \end{pmatrix}^+. \quad (4.68)$$

If the degree of the polynom P is increased by one, three new unknown variables are introduced into the system. For this reason, the system must be approximated by a lower degree polynom to be able to calibrate the system without needing an unrealistic amount of measurements. Additionally, the powers of the temperature matrix are widely unknown, which is why the complexity of dependencies (especially regard-

ing Fourier frequencies and temperature) should be reduced to be able to calibrate effective constants \tilde{C} that cover a lot of internal behavior.

Similar to section 4.2.1, it is assumed that the narrow temperature range allows the use of an affine function. Thus $P = 1$ and $K = 1$ is used in the following. Lower Fourier frequencies are more robust against noise as only properties existing over a broad range of the optical spectrum are taken into account. Therefore, only three frequencies are used in the analysis: the zero frequency $t_v = 0$, the first positive frequency $t_{v,1} = +1$ and the first negative frequency $t_{v,2} = -1$ (this approach is based on a discrete Fourier transformation, therefore index numbers are sufficient for a description of the frequency). Note that $t_{v,1}$ and $t_{v,2}$ carry the same information due to the symmetrical properties of the Fourier spectrum for real functions, which is why the use of just $t_{v,1}$ is equivalent. The restriction to only one frequency additionally increases the accuracy of the assumption, that an affine function describes the behavior sufficiently well due to the reduced complexity of the system. Accordingly equation (4.62) simplifies to

$$\tilde{C}(t_v) = -\Gamma_p |t_v| - \Theta_p t_v^2 - i\Delta\nu_p t_v \quad (4.69)$$

$$\ln \left(\frac{\sum_{a,t_v=1}(T)}{\sum_{a,t_v=0}(T)} \right) \approx C(1) + \tilde{C}(1)T = \begin{pmatrix} 1 & T \end{pmatrix} \begin{pmatrix} C(1) \\ \tilde{C}(1) \end{pmatrix}. \quad (4.70)$$

This equation is easily calibrated by using the method already mentioned in section 4.2.1.

To sum up, the logarithmic ratio of the zero frequency and first frequency term of a discrete Fourier transformation of the optical spectrum measured in the region defined by equation (4.32) is expected to depend on the temperature in an affine way. This approach requires an accurate measurement, sampling and Fourier transformation (using an appropriate window function) of the optical spectrum, which is more complex than just measuring two regions like in the FIR case.

4.3 Experimental Results

The measurement setup is depicted in figure 4.3. To be able to measure the emission, the system must be excited. Measuring the emission spectrum in the same direction as the excitement is called *in transmission*. Measuring in the opposite direction is denoted as *in reflection*. Measuring in reflection requires some kind of beam splitter. Beam splitters (especially in fiber optics) exhibit their own transmission curves altering the original spectrum. Therefore, the measurement described in this section is carried out in transmission. Measuring in transmission (and also in reflection due to non-ideal effects) requires an excitation light source with a wavelength which is not part of the

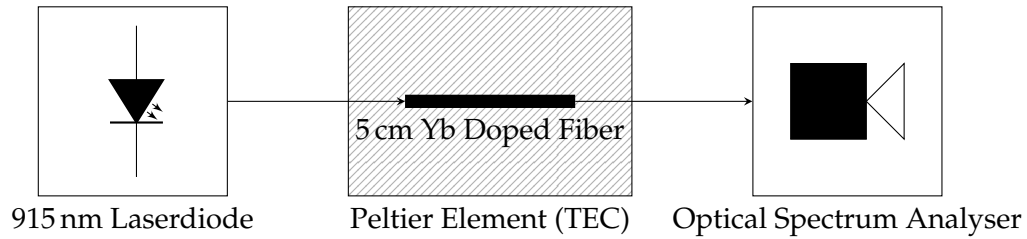


Figure 4.3: The utilized setup for measuring the fluorescence spectrum. The peltier element was used for temperature stabilization. The resolution of the optical spectrum analyzer was set to 0.05 nm or, equivalently, 13.6 GHz in the 1000 nm range.

emission spectrum. Accordingly a 915 nm light source is used in this work to excite the dopant.

Figure 4.4 shows an example measurement. A remarkable disadvantage of the measurement in transmission is the visibility of the laser diode's emission spectrum, which is probably the reason for the behavior of the spectrum at the left and right borders, where the measured intensity increases proportional to the laser power. In order to avoid wrong measurements of the fluorescence peaks due to the visibility of the laser diode's emission spectrum, the length of the fiber was increased to obtain higher fluorescence intensities. Therefore, instead of a 5 mm fiber length as used in section 3.2, the fiber used for the following measurements has a length of 5 cm. The spectrum of the laser diode could alternatively be filtered with increased effort.

Another problem are unwanted reflections in the fiber. These reflections are caused by intersections between two fibers with different refractive indices or imperfect splices. The reflections form interferometers with a periodic filtering pattern clearly visible around the peaks of the measurements in figures 4.4 and 4.5. Especially the measurement near the main peak in figure 4.4 is almost unusable as the periodicity of the interferometer is similar to the peak bandwidth. A profound conclusion about the peak power and spectral change over temperature is not possible as the interferometric effect overlays the temperature effects. However, the spectral part of interest is the second and not the main peak (refer to equation (4.32)). This is why there is no further investigation for a possible reduction of the interferometric effects.

The second peak that is used for the temperature measurement is shown in greater detail in figure 4.5. Five temperatures between 283 K and 323 K were used for calibration. For each temperature, seven laser powers from 55 mW to 145 mW were applied to test the robustness of the system.

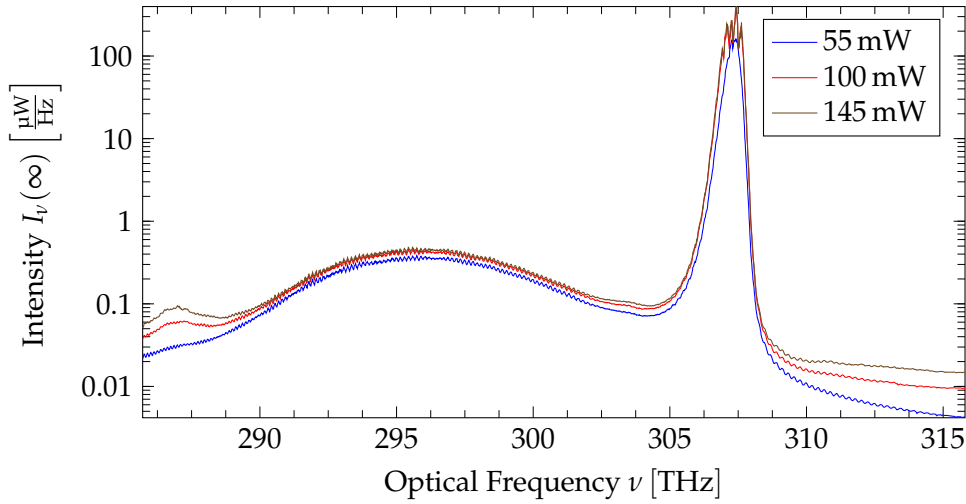


Figure 4.4: The measured Spectrum $I_\nu(\infty)$ of the Ytterbium doped fiber over different powers for the 915 nm excitation laserdiode at room temperature $T = 293$ K. The interferometric distortions at the main emission peak for high excitation powers prevent an accurate measurement of the peak power, whereas the second peak shows less distortions. Some excitation proportional effects occur at the low power borders of the spectrum, probably saturation effects or minor emissions of the used laserdiode.

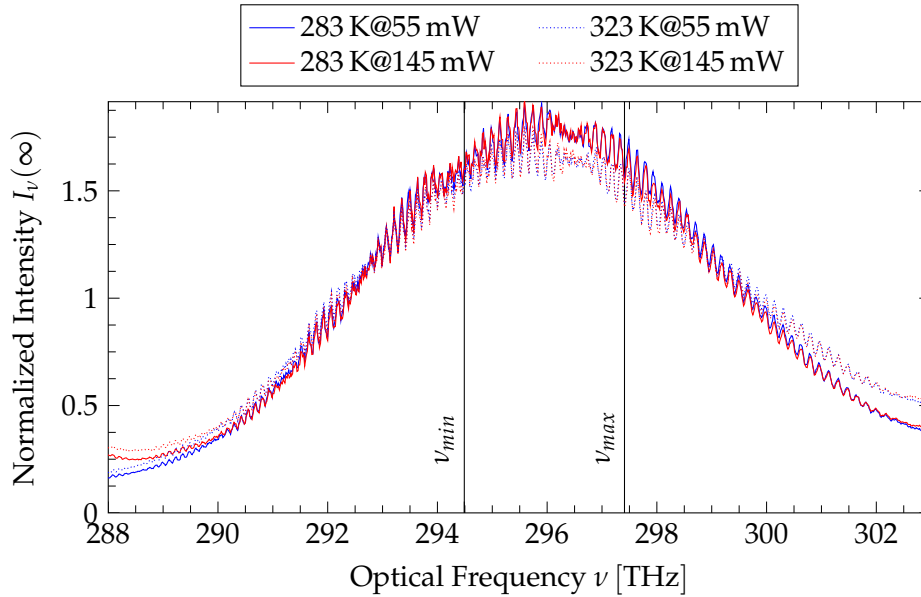


Figure 4.5: The normalized (i.e. relative to the mean of the plotted values) spectrum $I_\nu(\infty)$ of the Ytterbium doped fiber in the range of the second emission peak over different laser powers and fiber temperatures. Note that the shape is primarily temperature and not excitation dependent. Additionally a very small spectral shift to lower frequencies can be observed with higher temperatures. These shifts to lower frequencies are usually caused by pressure broadening [Dem11]. The oscillation is the result of unwanted reflections in the fiber creating interferometers.

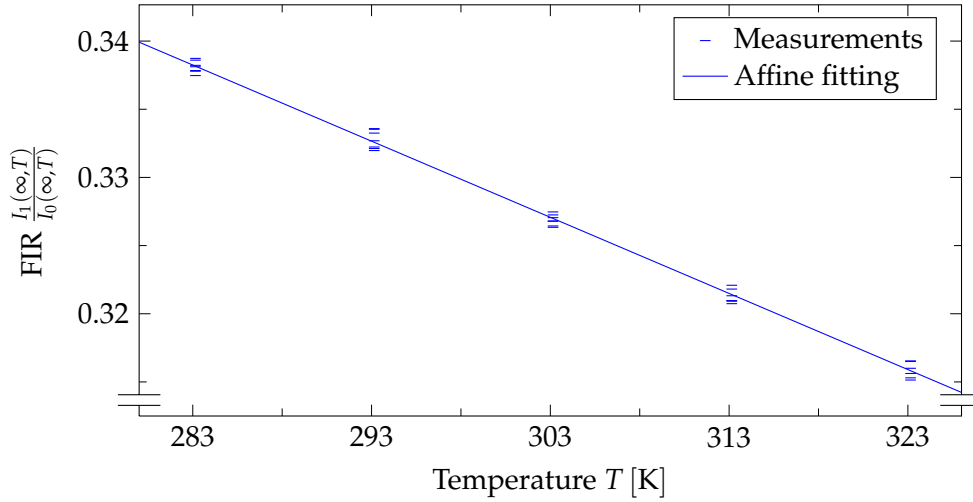


Figure 4.6: The FI Ratio as defined in section 4.2.1 and fitted using equation (4.56). $h_0(\nu)$ was chosen to be a rectangular window selecting the whole spectrum shown in figure 4.5. $h_1(\nu)$ is a rectangular window from $\nu_{min} = 294.49$ THz to $\nu_{max} = 297.41$ THz or alternatively with the center at a wavelength of 1013 nm and a bandwidth of 10 nm. The temperature sensitivity is about $\tilde{C}_1 \approx -0.00056 \frac{1}{K}$.

4.3.1 Fluorescence Intensity Ratio

A system was calibrated using the formulas derived in 4.2.1 and two rectangular functions $h_0(\nu)$ and $h_1(\nu)$. $h_0(\nu)$ simply selects the whole spectrum shown in figure 4.5. $h_1(\nu)$ is a rectangular function starting at ν_{min} and ending at ν_{max} . The resulting measurements for the seven different laser powers and the least squares fitting according to equation (4.59) are shown in figure 4.6. The assumption of an affine behavior seems to be fulfilled. The temperature sensitivity is about $\tilde{C}_1 \approx -0.00056 \frac{1}{K}$. The accuracy of temperature measurement has a standard deviation of about $\Delta T \approx 0.94$ K and will be discussed in further detail in section 4.3.3.

4.3.2 Fourier Domain Intensity Ratio

The measurement system in the Fourier domain was calibrated based on the formulas derived in 4.2.2. To minimize leakage effects, a Hamming window was used for the calculation of the discrete Fourier transformation. The result of the transformation applied to the spectrum in figure 4.5 is shown in figure 4.7. The stability over laser powers is higher for the first frequency index. Therefore, and according to equation (4.70), only the first frequency index was used for calibration.

The resulting measurements for the seven different laser powers and the least squares fitting according to equation (4.70) are shown in figure 4.8. The assumption of an affine behavior seems to be fulfilled. Note however, that the spectral shift represented

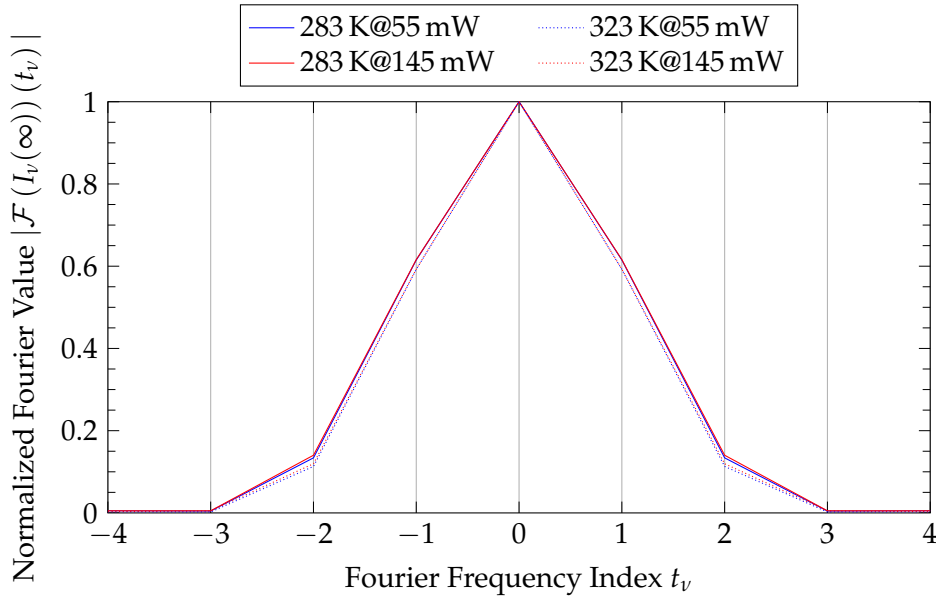


Figure 4.7: The normalized (i.e. relative to the zero frequency or mean) discrete Fourier transformation of the measured spectrum $I_v(\infty)$ as seen in 4.5. The transformation was done using a Hamming window and without adding any zero values (i.e. without any interpolation of the spectrum). While the second frequency index seems to be rather unstable with excitation, the first frequency index shows almost only temperature dependent behavior.

by the imaginary part of the logarithm (i.e. the Fourier phase) is not very robust and counteracts the accuracy of the real part. This is why only the real part is considered in the following. The temperature sensitivity of the real part is about $\tilde{C}_1 \approx -0.00095 \frac{1}{K}$. The accuracy of temperature measurement has a standard deviation of about $\Delta T \approx 0.95 K$ and will be discussed in further detail in section 4.3.3.

4.3.3 Comparison

A comparison of the FIR and the FDIR accuracy depicted in figure 4.9 shows no significant differences. Based on figure 4.9, both approaches measure increasing temperatures $T_{measured}$ with increasing laser powers. One reason could be the internal heating caused by the energy loss between excitation and emission leading to assumed temperature T_{real} that is too low. The standard deviation of both approaches is about 1 K, which is far better than the results expected by the fluorescence lifetime method but still worse than the accuracy of traditional methods (e.g. based on thermistors).

As already mentioned (see equation 4.14), the measurement based on the spectral shape needs a certain laser power to fulfill all assumptions. I.e. the laser power must excite enough electrons, such that the density $N_2(\infty)$ of excited electrons is large compared to $N_{2,0}(\infty) \frac{N_{eff} + \tilde{\sigma}_v N}{N_{2,0}(\infty) + \tilde{\sigma}_v N}$. These assumptions seem to be slightly violated for a laser

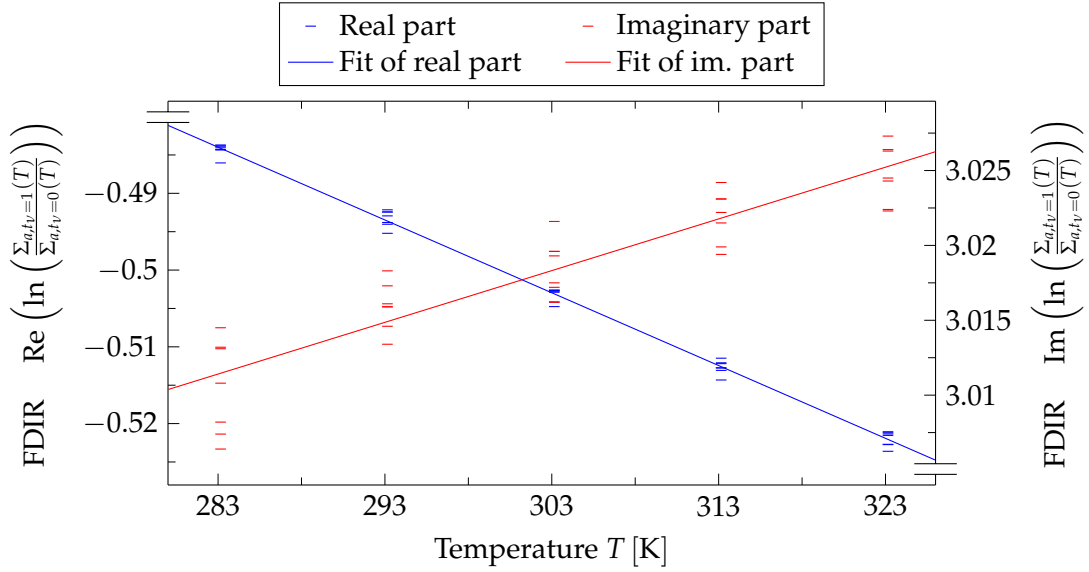


Figure 4.8: The FDI Ratio as defined in section 4.2.2 for only one frequency $t_v = 1$ and fitted using equation (4.70). The original Fourier domain spectrum is plotted in figure 4.7. Note the small shift to lower frequencies represented by the increasing imaginary part. Yet this shift is not very robust and might disturb the accuracy of the measurement, which is why only the real part is used for the actual temperature determination. The sensitivity is about $\tilde{C}(1) \approx -0.00095 \frac{1}{K}$ for the real part and $\tilde{C}(1) \approx 0.00035 \frac{1}{K}$ for the imaginary part.

power of 55 mW as the output spectrum has not completely reached its final shape independent of the excitation power leading to a false measurement. Yet this minimal laser power cannot be guaranteed in all environments.

The FIR approach could be realized based on custom made fiber optical filters and two photodiodes. This approach has the advantage of temperature measurements with only minor delay. The FDIR Methods needs a precise and fast optical spectrum analyzer and complex postprocessing. Without any significant advantages in accuracy, the FDIR method is inferior to the FIR method in terms of readout speed. However, the FDIR method is capable of tracking shifts of the spectrum, that might show greater sensitivities for other dopants.

Although an accuracy of 1 K is reasonable, it is expected to drop with shorter fibers and it is still much worse than accuracies possible with traditional methods. Additionally the self-heating of the fiber may be problematic for some applications and the minimal excitation power cannot be guaranteed in all systems. This why a third approach of temperature measurement will be analyzed in the next chapter based on the reflectometry technique for measuring magnitude and position of reflections in a fiber.

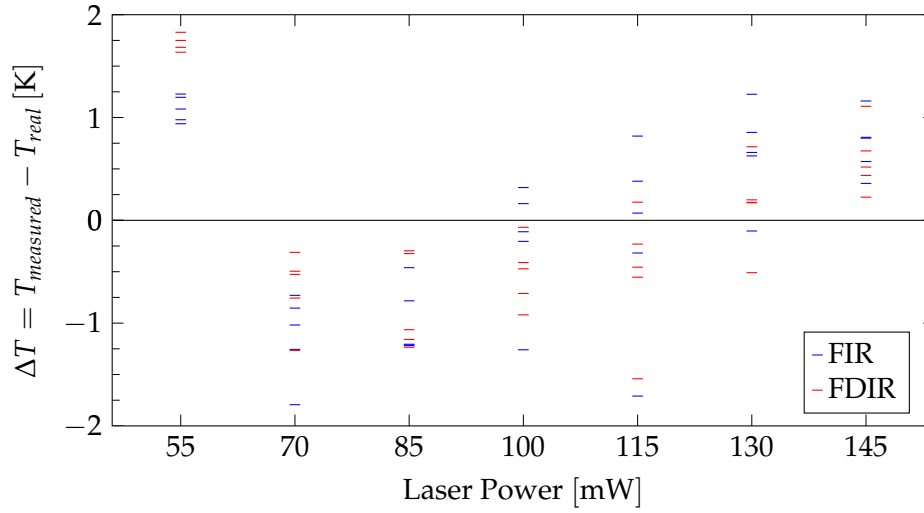


Figure 4.9: Accuracy of the temperature measurement using the spectral information. The spectral shape is too broad for the excitation with 55 mW leading to a temperature estimation that is too high. Thus, for 55 mW, the output spectrum has not completely reached its final shape (although this difference is practically invisible in figure 4.5). With increasing excitation, the temperature estimated is too high. One reason could be the internal heating caused by the energy loss between excitation and emission, leading to an assumed temperature T_{real} that is too low. The temperature estimation error is about 0.94 K (standard deviation) for the FIR approach and 0.95 K for the FDIR approach.

5 Reflectometry

Reflectometry techniques enable the distributed measurement of reflections in optical fibers. As scatterings can be interpreted as reflections, a distributed measurement of scattering effects in a fiber is possible, as well. The temperature (or strain) dependence of these reflections or scattering effects can be used to construct a sensing device.

Two reflectometry methods are reported in literature: the *Optical Time Domain Reflectometry* (OTDR) and the *Optical Frequency Domain Reflectometry* (OFDR), each having various subtypes. In fact OTDR can be seen as a special subtype of the Network Analysis (NA) OFDR. For this reason, OTDR will be explained along with NA-OFDR. [Yük09] presents the subtypes of the OFDR methods, which will be discussed in more detail in the following. A fiber internal refractive index of $n \approx 1.5$ will be assumed for calculations (e.g. like for the fiber SMF-28e+ by Corning [Inc11]).

5.1 Network Analysis Optical Frequency Domain Reflectometry

5.1.1 Method

For the NA-OFDR method [Nak87] [Dol88] a laser is intensity modulated with the function $u(t)$. The light is sent to the fiber under test through a coupler placed at distance y_l . The backscattered light in the fiber backpropagates through the coupler and reaches a photodiode measuring the current backscattered intensity. This photodiode has the distance y_p from the coupler (see figure 5.1). To reach a reflection in distance x from the coupler and travel to the photodiode, the light needs the time $\Delta t = \frac{2x+y_l+y_p}{v}$ with v being the light velocity in the fiber. While travelling to position x , the light is attenuated by $a(x)$. Additionally only a certain fraction $\sigma(x)$ of the incoming light is backscattered. The measured intensity $i(t)$ at the photodiode is the sum of all backscattered signals. Using L as length of the fiber under test, $i(t)$ is defined as

$$i(t) = \int_0^L a(x)\sigma(x)u(t - \Delta t) dx. \quad (5.1)$$

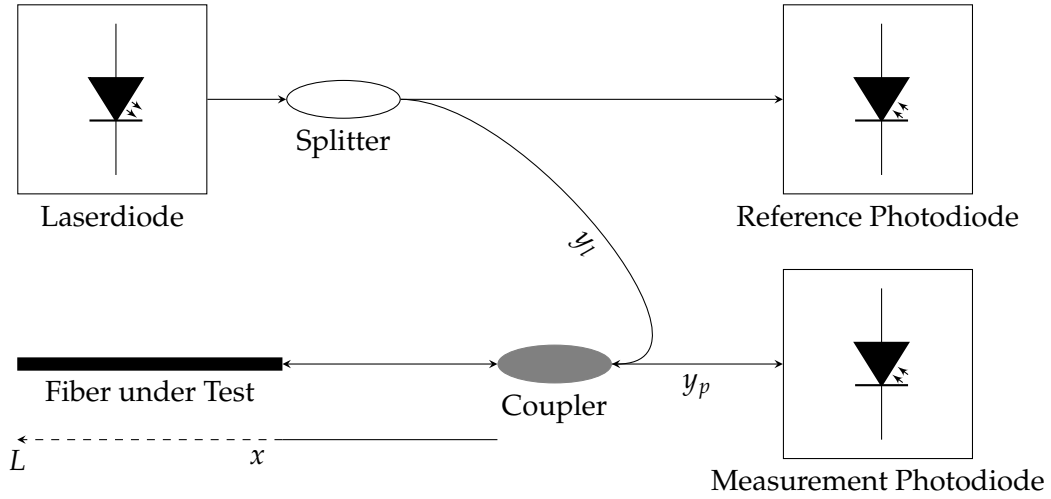


Figure 5.1: The setup for NA-OFDR measurements is shown. The laser emits modulated light with intensity $u(t)$ (measurable by using the reference photodiode), that is backscattered by the fiber reflections and measured by a photodiode. The coupler controls the distribution of emitted and scattered light. Ideally the fiber under test does not exhibit a Fresnel backreflection at its end, e.g. by using a core-less end cap and/or an angled end face.

With $s(x)$ as rectangular window function from $x = 0$ to $x = L$ and by using the relations $x = \frac{v}{2}\Delta t - \frac{y_l + y_p}{2}$ and $dx = \frac{v}{2} d\Delta t$, the equation can be rewritten as

$$\tilde{s}(\Delta t) = s\left(\frac{v}{2}\Delta t - \frac{y_l + y_p}{2}\right) \quad (5.2)$$

$$\tilde{a}(\Delta t) = a\left(\frac{v}{2}\Delta t - \frac{y_l + y_p}{2}\right) \quad (5.3)$$

$$\tilde{\sigma}(\Delta t) = \sigma\left(\frac{v}{2}\Delta t - \frac{y_l + y_p}{2}\right) \quad (5.4)$$

$$i(t) = \frac{v}{2} \int_{-\infty}^{\infty} \tilde{s}(\Delta t) \tilde{a}(\Delta t) \tilde{\sigma}(\Delta t) u(t - \Delta t) d\Delta t, \quad (5.5)$$

where $\tilde{s}(\Delta t)$, $\tilde{a}(\Delta t)$ and $\tilde{\sigma}(\Delta t)$ are just compressed and shifted versions of $s(x)$, $a(x)$ and $\sigma(x)$. This corresponds to a convolution

$$i(t) = \frac{v}{2} (\tilde{s} \tilde{a} \tilde{\sigma} * u)(t). \quad (5.6)$$

Using the Fourier transformation yields

$$I(f) = \frac{v}{2} \mathcal{F}(\tilde{s}(t) \tilde{a}(t) \tilde{\sigma}(t)) \cdot U(f). \quad (5.7)$$

The scattering coefficients can be determined by inversion

$$\tilde{s}(t) \tilde{a}(t) \tilde{\sigma}(t) = \mathcal{F}^{-1} \left(\frac{2 \cdot I(f)}{v \cdot U(f)} \right). \quad (5.8)$$

5.1.2 Resolution

The accuracy of this approach is limited by the accuracy of the inverse Fourier transform. An inverse Fourier transform done for a Fourier domain signal with enforced bandwidth B has the accuracy $t_{acc} = \frac{1}{B}$, because the bandwidth enforcement corresponds to a lowpass of the time domain signal. E.g. in case of a rectangular window function for bandwidth restriction with bandwidth B , the time domain signal will be convoluted with a sinc function that has its first zero transition at $\frac{1}{B}$.

Since the signal $I(f)$ is limited by the bandwidth B_U of $U(f)$, the inverse transform in equation (5.8) has the accuracy $t_{acc} = \frac{1}{B_U}$ leading to a spatial resolution of

$$\Delta x = \frac{v}{2B_U}. \quad (5.9)$$

Most OFDR techniques use a sinusoidally modulated signal $u(t)$ to create a high frequency signal $U(f)$. In contrast to that, OTDR is based on pulsed functions $u(t)$ [Bar76]. Pulses exhibit high frequency behavior, as well, and the same formulas hold, no matter if $u(t)$ represents sine waves or pulses.

For sensing areas in the mm scale, e.g. $\Delta x = 1$ mm, bandwidths in the hundreds of gigahertz are necessary. Even the fastest analog circuits cannot measure signals $I(f)$ in this frequency range. Thus, high resolution sensing is not practical using NA-OFDR methods.

5.2 Incoherent Frequency-Modulated Continuous Wave OFDR

5.2.1 Method

The Incoherent Frequency-Modulated Continuous Wave OFDR [Mac81] is similar to the NA-OFDR. The intensity of the laser is modulated and the reflection is measured by a photodiode (the general setup is therefore identical to NA-OFDR, see figure 5.1). However, the modulation function $u(t)$ is based on a linear chirp with the current frequency $f(t) = f_0 + \gamma t$

$$u(t) = C + C \cos \left(2\pi \int_0^t [f_0 + \gamma \tilde{t}] d\tilde{t} \right) = C + C \cos \left(2\pi \left[f_0 + \frac{\gamma}{2} t \right] t \right). \quad (5.10)$$

Thus, the measurement results in (compare to equation (5.5))

$$i(t) = C \frac{v}{2} \int_{-\infty}^{\infty} \tilde{s}(\Delta t) \tilde{a}(\Delta t) \tilde{\sigma}(\Delta t) d\Delta t + C \frac{v}{2} \int_{-\infty}^{\infty} \tilde{s}(\Delta t) \tilde{a}(\Delta t) \tilde{\sigma}(\Delta t) \cos \left(2\pi \left[f_0 + \frac{\gamma}{2} [t - \Delta t] \right] [t - \Delta t] \right) d\Delta t. \quad (5.11)$$

The AC part of $i(t)$ is (e.g. electronically) multiplied with the AC part of the modulation signal $u(t)$ yielding

$$i_M(t) = C^2 \frac{v}{4} \int_{-\infty}^{\infty} \tilde{s}(\Delta t) \tilde{a}(\Delta t) \tilde{\sigma}(\Delta t) \cdot \left[\cos \left(2\pi \gamma \Delta t \cdot t + 2\pi \left[f_0 - \frac{\gamma}{2} \Delta t \right] \Delta t \right) + \cos \left(2\pi [2f_0 + \gamma [t - \Delta t]] \cdot t - 2\pi \left[f_0 - \frac{\gamma}{2} \Delta t \right] \Delta t \right) \right] d\Delta t. \quad (5.12)$$

The second summand can easily be filtered out due to its high frequency of $f \geq 2f_0$. The first summand consists of summed cosines, where the amplitude of the cosine with frequency $f = \gamma \Delta t$ corresponds to the factor $\tilde{s}(\Delta t) \tilde{a}(\Delta t) \tilde{\sigma}(\Delta t)$. Applying a Fourier transformation on the filtered $i_M(t)$ yields

$$I_M(f) = C^2 \frac{v}{8} \int_{-\infty}^{\infty} \tilde{s}(\Delta t) \tilde{a}(\Delta t) \tilde{\sigma}(\Delta t) [\delta(f + \gamma \Delta t) + \delta(f - \gamma \Delta t)] e^{i2\pi f \frac{f_0 - \frac{\gamma}{2} \Delta t}{\gamma}} d\Delta t \\ = C^2 \frac{v}{8} \tilde{s}\left(\frac{f}{\gamma}\right) \tilde{a}\left(\frac{f}{\gamma}\right) \tilde{\sigma}\left(\frac{f}{\gamma}\right) e^{i2\pi f \frac{f_0 - \frac{f}{2}}{\gamma}} + C^2 \frac{v}{8} \tilde{s}\left(-\frac{f}{\gamma}\right) \tilde{a}\left(-\frac{f}{\gamma}\right) \tilde{\sigma}\left(-\frac{f}{\gamma}\right) e^{i2\pi f \frac{f_0 + \frac{f}{2}}{\gamma}}. \quad (5.13)$$

Using the definition of $\tilde{s}(\Delta t)$ (i.e. $\tilde{s}(\Delta t) = 0$ for $\Delta t \leq 0$) yields

$$I_M(f) = C^2 \frac{v}{8} \tilde{s}\left(\frac{|f|}{\gamma}\right) \tilde{a}\left(\frac{|f|}{\gamma}\right) \tilde{\sigma}\left(\frac{|f|}{\gamma}\right) e^{i2\pi f \frac{f_0 - \frac{|f|}{2}}{\gamma}}. \quad (5.14)$$

The advantage of this approach is that only a single AD conversion channel and only a single Fourier transformation is needed.

5.2.2 Resolution

The accuracy of this approach is again based on the length of the signal to be Fourier transformed. The frequency accuracy for a signal of length T is $f_{acc} = \frac{1}{T}$. The resulting spatial accuracy is according to equation 5.4 and 5.14

$$\Delta x = \frac{v}{2\gamma T} \quad (5.15)$$

with γT being the sweep range of the modulated input. Thus for a resolution of $\Delta x = 1$ mm and a refractive index of $n \approx 1.5$, a sweep range of $\gamma T \approx 100$ GHz (intensity frequency, *not* optical frequency) is necessary, which is far beyond any driving or measuring capabilities.

Both methods presented so far are unsuitable to track fiber reflections with high resolution. Therefore a third approach is evaluated in the next section, namely the *Coherent Optical Frequency Domain Reflectometry* (C-OFDR).

5.3 Coherent Optical Frequency Domain Reflectometry

5.3.1 Method

Instead of using the light intensity, C-OFDR uses the optical frequency ν (i.e. electromagnetic field) to create a linear frequency sweep [Eic81]. Using a constant intensity, the modulation function for the electro-magnetic field is (compare to equation (5.10))

$$u(t) = C \cos \left(2\pi \left[\nu_0 + \frac{\gamma}{2} t \right] t \right). \quad (5.16)$$

Obviously, even in case of a slowly (in comparison to the maximum time delay in the system) varying amplitude C , a normalization with a reference signal can compensate for these fluctuations and the assumption of a constant intensity is still fulfilled.

The measured optical intensity $i(t)$ is proportional to the squared magnitude of the electro-magnetic field $e(t)$ (compare to the *Poynting vector*) yielding (similar to equation (5.5))

$$e(t) = C \frac{v}{2} \int_{-\infty}^{\infty} \tilde{s}(\Delta t) \tilde{a}(\Delta t) \tilde{\sigma}(\Delta t) \cos \left(2\pi \left[\nu_0 + \frac{\gamma}{2} [t - \Delta t] \right] [t - \Delta t] + \tilde{\phi}(\Delta t) \right) d\Delta t \quad (5.17)$$

$$i(t) \propto e(t)^2, \quad (5.18)$$

where $\tilde{\phi}(\Delta t)$ models possible phase shifting effects that may occur in case of electro-magnetic wave reflections. Assuming a dominant reflection at position R with the corresponding time delay $\Delta t_R = \frac{2R + y_l + y_p}{v}$ and reflection magnitude $\tilde{a}_R \tilde{\sigma}_R$ is added, the overall measured intensity $i_R(t)$ becomes

$$e_R(t) = C \tilde{a}_R \tilde{\sigma}_R \cos \left(2\pi \left[\nu_0 + \frac{\gamma}{2} [t - \Delta t_R] \right] [t - \Delta t_R] \right) \quad (5.19)$$

$$i_R(t) \propto (e(t) + e_R(t))^2 = e(t)^2 + 2e(t)e_R(t) + e_R(t)^2. \quad (5.20)$$

The complete setup is depicted in figure 5.2 and will be further explained in section 5.3.6. The dominant reflection was thereby realized by a mirror. An alternative to

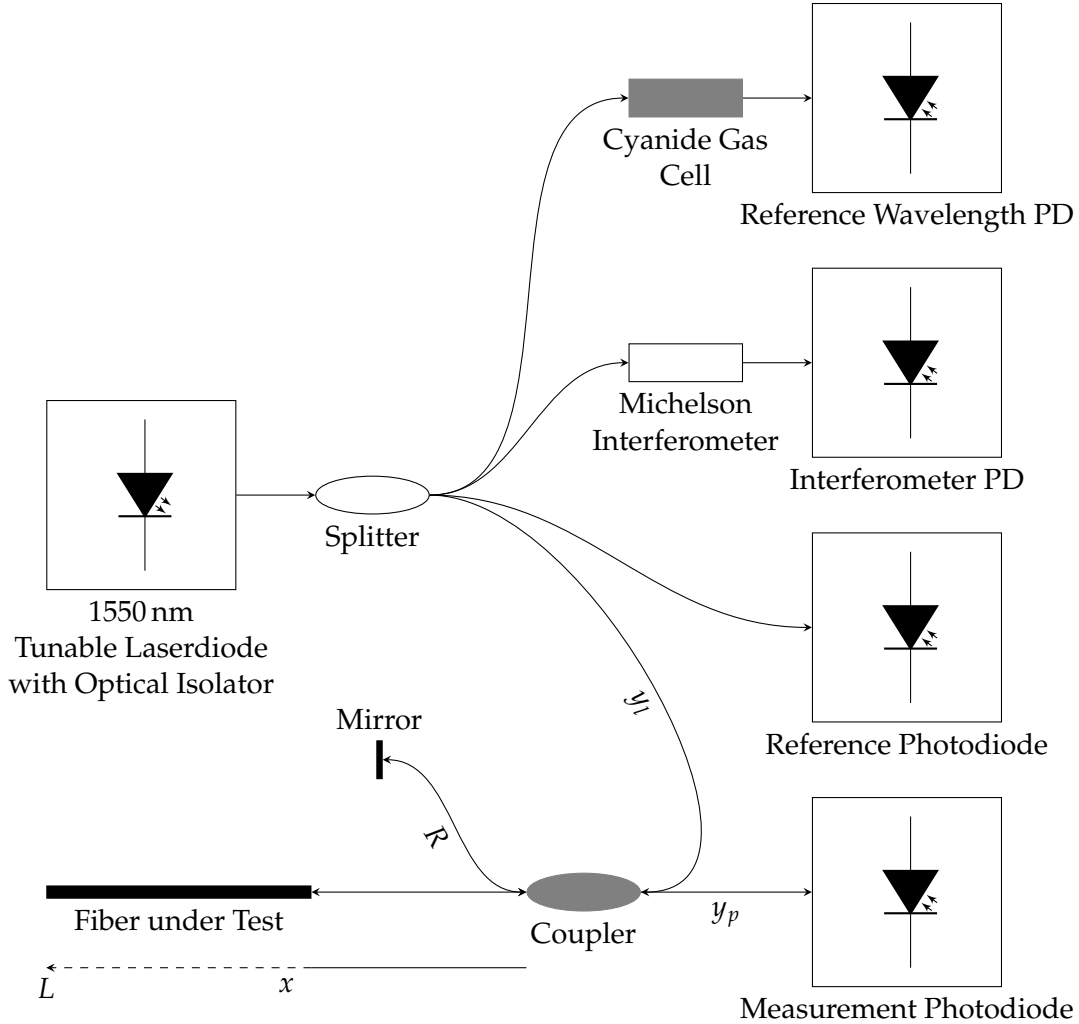


Figure 5.2: The setup for coherent OFDR. The laser emits wavelength modulated light $u(t)$ that is backscattered by the fiber reflections and measured by a photodiode as intensity $i_R(t)$. The coupler controls the distribution of emitted and scattered light. Several additional photodiodes ensure proper compensation of nonideal effects (further details in section 5.3.6). The tuneable laser must be equipped with an optical isolator to prevent damage caused by the reflected signal (compare to [Gen05]). Alternatively, the coupler must be replaced by a system preventing the backreflection of the laser power to the laser diode (e.g. by using multiple couplers like in [Gif07]). Ideally the fiber under test does not exhibit a Fresnel backreflection at its end, e.g. by using a core-less end cap and/or an angled end face.

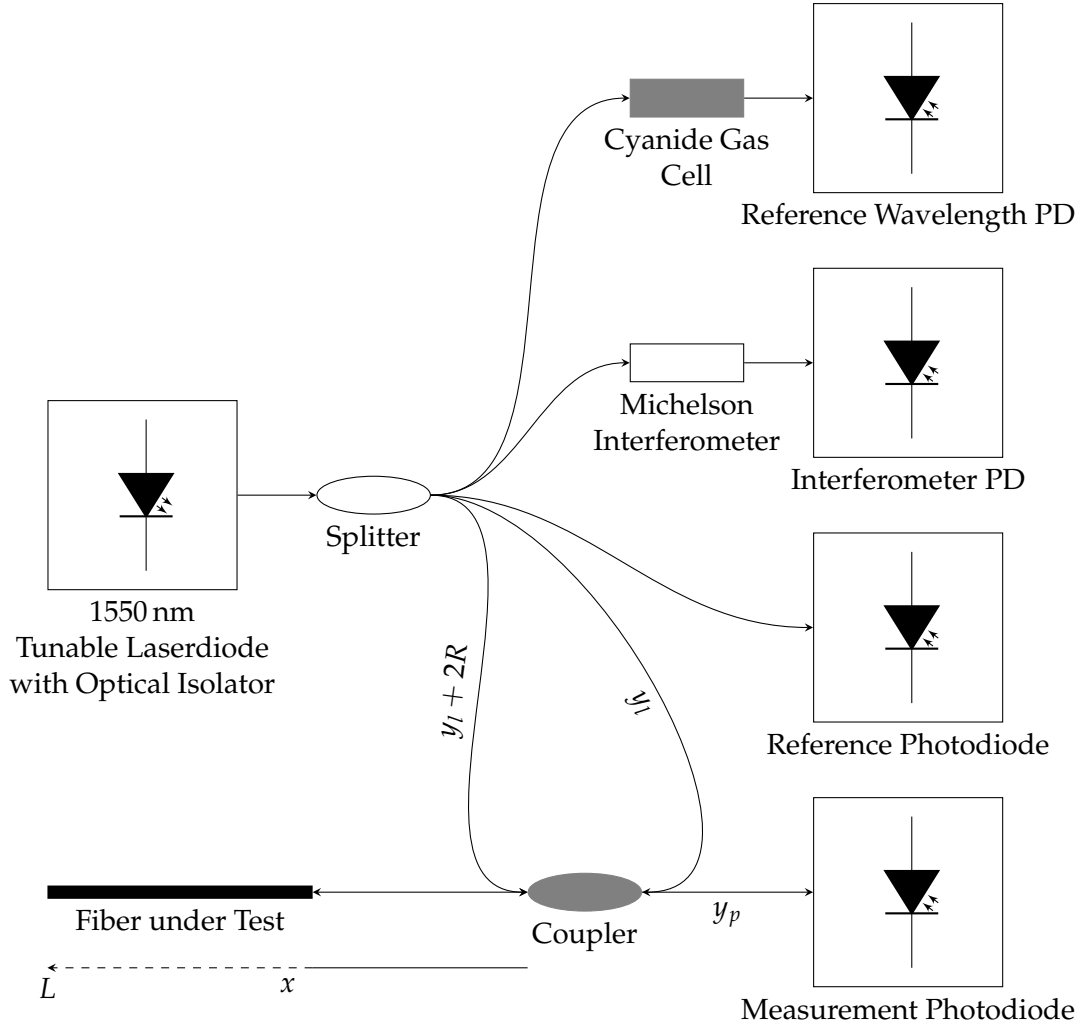


Figure 5.3: The setup for an alternative coherent OFDR is shown. Instead of using a reference mirror, the laser is directly connected to the coupler in forward and backward direction. Everything else is identical to figure 5.2. The advantage is (especially for measuring low signal reflections in the fiber under test), that no noise interferences can occur in the reference path of the coupler. However light beam changes (e.g. polarization or attenuation) between splitter and coupler cannot be compensated in this setup. A modification for improved polarization handling is found in [Gif07]. As no significant noise interferences in the reference path of the coupler are expected in the scope of this work, the setup shown in figure 5.2 will be used.

the setup presented in figure 5.2 worth mentioning is shown in figure 5.3. The mirror has been replaced with a virtual mirror created by connecting the laser directly to the reference input of the coupler. This reduces the amount of unwanted interferometric effects with the cost of a higher sensitivity to attenuation or polarization changes in the transmitting fiber.

As the reflection at R is dominant, i.e. $e(t) \ll e_R(t)$, the following approximation holds

$$i_R(t) \propto 2e(t)e_R(t) + e_R(t)^2. \quad (5.21)$$

The summands in equation 5.21 are

$$e_R(t)^2 = \frac{C^2}{2} \tilde{a}_R^2 \tilde{\sigma}_R^2 [1 + \cos(2\pi [2\nu_0 + \gamma [t - \Delta t_R]] [t - \Delta t_R])] \quad (5.22)$$

$$\begin{aligned} 2e(t)e_R(t) = & C^2 \frac{\nu}{2} \int_{-\infty}^{\infty} \tilde{s}(\Delta t) \tilde{a}(\Delta t) \tilde{\sigma}(\Delta t) \tilde{a}_R \tilde{\sigma}_R \\ & \cdot \left[\cos(2\pi \gamma [\Delta t - \Delta t_R] \cdot [t - t_{\varphi_1}] - \tilde{\phi}(\Delta t)) \right. \\ & \left. + \cos(2\pi [2\nu_0 + \gamma [t - \Delta t - \Delta t_R]] \cdot [t - t_{\varphi_2}] + \tilde{\phi}(\Delta t)) \right] d\Delta t \end{aligned} \quad (5.23)$$

with

$$t_{\varphi_1} = -\frac{\nu_0 - \frac{\gamma}{2} [\Delta t + \Delta t_R]}{\gamma} \quad (5.24)$$

$$t_{\varphi_2} = \frac{\nu_0 [\Delta t + \Delta t_R] - \frac{\gamma}{2} [\Delta t^2 + \Delta t_R^2]}{2 [\nu_0 + \frac{\gamma}{2} [t - \Delta t - \Delta t_R]]}. \quad (5.25)$$

Frequencies in the terahertz range, e.g. the (optical) frequency $2\nu_0$, are filtered by the lowpass effect inherent in every semiconductor photodiode. Accordingly all high frequency terms with $f \geq 2\nu_0$ (i.e. the second summands) can be ignored as they get filtered out automatically during measurement.

For easier calculations, the measurement can be transformed to use the current frequency sweep $\Delta\nu = \gamma t$ instead of the time (i.e. to use the control value instead of the measurement value)

$$e_R(\Delta\nu)^2 = \frac{C^2}{2} \tilde{a}_R^2 \tilde{\sigma}_R^2 \quad (5.26)$$

$$\begin{aligned} 2e(\Delta\nu)e_R(\Delta\nu) = & C^2 \frac{\nu}{2} \int_{-\infty}^{\infty} \tilde{s}(\Delta t) \tilde{a}(\Delta t) \tilde{\sigma}(\Delta t) \tilde{a}_R \tilde{\sigma}_R \\ & \cdot \cos(2\pi [\Delta t - \Delta t_R] \cdot [\Delta\nu - \gamma t_{\varphi_1}] - \tilde{\phi}(\Delta t)) d\Delta t. \end{aligned} \quad (5.27)$$

Applying a Fourier transformation from $\Delta\nu$ to t_ν combined with the functions defined in equations (5.2) to (5.4) yields

$$\mathcal{F}(e_R(\Delta\nu)^2) = \frac{C^2}{2} \tilde{a}_R^2 \tilde{\sigma}_R^2 \delta(t_\nu) \quad (5.28)$$

$$\begin{aligned} & \mathcal{F}(2e(\Delta\nu)e_R(\Delta\nu)) \\ &= C^2 \frac{v}{4} \int_{-\infty}^{\infty} \tilde{s}(\Delta t) \tilde{a}(\Delta t) \tilde{\sigma}(\Delta t) \tilde{a}_R \tilde{\sigma}_R \\ & \quad [\delta(t_\nu - [\Delta t - \Delta t_R]) + \delta(t_\nu + [\Delta t - \Delta t_R])] e^{-i2\pi t_\nu \left[\gamma t_{\phi 1} + \frac{\tilde{\phi}(\Delta t)}{2\pi[\Delta t - \Delta t_R]} \right]} d\Delta t \quad (5.29) \\ &= C^2 \frac{v}{4} s\left(R + \frac{vt_\nu}{2}\right) a\left(R + \frac{vt_\nu}{2}\right) \sigma\left(R + \frac{vt_\nu}{2}\right) \tilde{a}_R \tilde{\sigma}_R e^{i2\pi t_\nu [v_0 - \gamma \Delta t_R - \frac{\gamma t_\nu}{2}]} - i\tilde{\phi}(\Delta t_R + t_\nu) \\ & \quad + C^2 \frac{v}{4} s\left(R - \frac{vt_\nu}{2}\right) a\left(R - \frac{vt_\nu}{2}\right) \sigma\left(R - \frac{vt_\nu}{2}\right) \tilde{a}_R \tilde{\sigma}_R e^{i2\pi t_\nu [v_0 - \gamma \Delta t_R + \frac{\gamma t_\nu}{2}]} + i\tilde{\phi}(\Delta t_R - t_\nu). \end{aligned} \quad (5.30)$$

The Fourier transformation for $i_R(\Delta\nu)$ from $\Delta\nu$ to t_ν is denoted by (compare to equation (5.21))

$$I_R(t_\nu) = \mathcal{F}(i_R(\Delta\nu)) \propto \mathcal{F}(e_R(\Delta\nu)^2) + \mathcal{F}(2e(\Delta\nu)e_R(\Delta\nu)). \quad (5.31)$$

Using the properties of $s(x)$ as introduced in section 5.1 as well as $\delta(0) \approx \Delta\nu_{max}$ due to the resolution limitations of the Fourier transform with $\Delta\nu_{max}$ being the maximum frequency shift and the conversion $\Delta x = \frac{v}{2\Delta\nu_{max}}$ (see chapter 5.3.2), the following sums up the relationships between $a(x)\sigma(x)$ and $I_R(t_\nu)$

$$\tilde{\phi}(\Delta t) = \phi\left(\frac{v}{2}\Delta t - \frac{y_l + y_p}{2}\right) \quad (5.32)$$

$$a_\sigma(x) = a(x)\sigma(x) \quad (5.33)$$

$$\begin{aligned} I_R\left(\pm 2\frac{|x-R|}{v}\right) &\propto C^2 \frac{v}{4} \tilde{a}_R \tilde{\sigma}_R \cdot \dots \\ &\left\{ \begin{aligned} & \left[2a_\sigma(R) + \frac{\tilde{a}_R \tilde{\sigma}_R}{\Delta x} \right], & 0 = |x-R| \\ & \left[a_\sigma(x) e^{\pm i4\pi \frac{|x-R|}{v} \left[v_0 - \frac{\gamma}{v} [v\Delta t_R + x - R] - \frac{v\phi(x)}{4\pi|x-R|} \right]} \dots \right. \\ & \quad \left. + a_\sigma(2R-x) e^{\pm i4\pi \frac{|x-R|}{v} \left[v_0 - \frac{\gamma}{v} [v\Delta t_R + R - x] - \frac{v\phi(2R-x)}{4\pi|R-x|} \right]} \right], & 0 < |x-R| \leq \min(R, |L-R|) \\ & a_\sigma(x) e^{\pm i4\pi \frac{|x-R|}{v} \left[v_0 - \frac{\gamma}{v} [v\Delta t_R + x - R] - \frac{v\phi(x)}{4\pi|x-R|} \right]}, & |x-R| > \min(R, |L-R|) \end{aligned} \right. \end{aligned} \quad (5.34)$$

How to use these relationships for stable measuring will be discussed in the next sections after an analysis of the resolution.

5.3.2 Resolution

Fourier Limitations

Based on the constraints of the Fourier transformation, the resolution for t_ν is $t_{\nu,acc} = \frac{1}{\Delta\nu_{max}}$ with $\Delta\nu_{max}$ being the maximum frequency shift leading to a spatial resolution of

$$\Delta x = \frac{v}{2\Delta\nu_{max}}. \quad (5.35)$$

A frequency sweep of $\Delta\nu_{max} \approx 100$ GHz is necessary to obtain 1 mm resolution with a refractive index of $n \approx 1.5$. That corresponds to a wavelength sweep of about 0.8 nm for a 1550 nm light source, which is easily obtainable. According to the Nyquist theorem, the maximum length depends on the stepsize $s_{\Delta\nu}$ of the measured frequencies $\Delta\nu$ and is

$$\max(L - R, R) = \frac{v}{2} t_{\nu,max} = \frac{v}{4s_{\Delta\nu}}. \quad (5.36)$$

Comparable results are obtained in [Sol05].

A possible stepsize is 1 pm, leading to a maximal length of 0.4 m given a 1550 nm light source and a refractive index of $n \approx 1.5$. Another limiting property, especially for the length, is the laser coherence or spectral linewidth, which is discussed in more detail in the following.

Spectral Laser Linewidth Limitations

The electromagnetic light wave $u(t)$ describes the emitted electromagnetic amplitude over time. However, the electromagnetic field in reality consists of a sum of different waves each caused by a slightly different optical frequency ν' . In the following, an approach for modeling the imperfection of the electromagnetic wave is presented.

To describe the distribution of the optical frequencies around a center frequency, the spectral shape $G(\nu)$ is used in this work, where the sum of all different frequency shifts is described by a convolution in the frequency domain

$$\mathcal{F}(u(t)_{real})(\nu) = (\mathcal{F}(u(t)) * G)(\nu). \quad (5.37)$$

The scaling of $G(\nu)$ is chosen, such that (according to the law of conservation of energy) the energy of a perfect cosine $u(t)$ is not changed by the convolution, i.e.

$$\int_{-\infty}^{\infty} |\mathcal{F}(u(t))(\nu)|^2 d\nu = \int_{-\infty}^{\infty} |\mathcal{F}(u(t)_{real})(\nu)|^2 d\nu. \quad (5.38)$$

Because $\mathcal{F}(u(t))$ has a dirac shape in case $u(t)$ is a perfect cosine, the following relation holds

$$\int_{-\infty}^{\infty} \delta(\nu)^2 d\nu = \int_{-\infty}^{\infty} |G(\nu)|^2 d\nu. \quad (5.39)$$

Using

$$\int_{-\infty}^{\infty} \delta(\nu)^2 d\nu = \int_{-\infty}^{\infty} \delta(\nu)\delta(\nu-0) d\nu = \delta(\nu=0) \quad (5.40)$$

leads to

$$\int_{-\infty}^{\infty} |G(\nu)|^2 d\nu = \delta(\nu=0). \quad (5.41)$$

The time domain functions are:

$$g(t) = \mathcal{F}^{-1}(G(\nu))(t) \quad (5.42)$$

$$u_{real}(t) = u(t) \cdot g(t). \quad (5.43)$$

The electromagnetic fields can therefore be modeled by

$$e(t) = \frac{v}{2} \int_{-\infty}^{\infty} \tilde{s}(\Delta t) \tilde{a}(\Delta t) \tilde{\sigma}(\Delta t) g(t - \Delta t) u(t - \Delta t) d\Delta t \quad (5.44)$$

$$e_R(t) = \tilde{a}_R \tilde{\sigma}_R g(t - \Delta t_R) u(t - \Delta t_R). \quad (5.45)$$

$u(t - \Delta t)$ is assumed to include possible phase shifts without having any influence on $g(t - \Delta t)$. Possible phase shifts ϕ in $u(t)_{real}$ show up as a multiplication with a symmetric (i.e. complex conjugated for positive and negative frequencies) exponential $e^{i \text{sign}(\nu)\phi}$ in frequency domain. Accordingly, it can be modeled as being part of $u(t)$ only. As $\mathcal{F}(u(t))$ lacks zero frequency regions, a convolution of the phase shifted transform $\mathcal{F}(u(t))$ with G yields the same result as if the phase would have been added after the convolution. Therefore G can be assumed to be independent of a possible phase shift.

The products $e_R(t)^2$ and $2e(t)e_R(t)$ are calculated by

$$e_R(t)^2 = \tilde{a}_R^2 \tilde{\sigma}_R^2 g(t - \Delta t_R)^2 u(t - \Delta t_R)^2 \quad (5.46)$$

$$2e(t)e_R(t) = v \int_{-\infty}^{\infty} \tilde{s}(\Delta t) \tilde{a}(\Delta t) \tilde{\sigma}(\Delta t) \tilde{a}_R \tilde{\sigma}_R \cdot g(t - \Delta t) g(t - \Delta t_R) u(t - \Delta t) u(t - \Delta t_R) d\Delta t. \quad (5.47)$$

It is known from equations (5.21) to (5.23), that

$$u(t - \Delta t_R)^2 = \frac{C^2}{2} \quad (5.48)$$

$$u(t - \Delta t_R) u(t - \Delta t) = \frac{C^2}{2} \cos(2\pi\gamma [\Delta t - \Delta t_R] \cdot [t - t_{\phi_1}] - \tilde{\phi}(\Delta t)). \quad (5.49)$$

Using $t = \frac{\Delta v}{\gamma}$, the Fourier transformations of $e_R(\Delta v)^2$ and $2e(\Delta v)e_R(\Delta v)$ are

$$\mathcal{F}(e_R(\Delta v)^2) = \frac{C^2}{2} \tilde{a}_R^2 \tilde{\sigma}_R^2 \gamma^2 \left(G(\gamma\tau_v) e^{-i2\pi\gamma\tau_v\Delta t_R} *_{\tau_v} G(\gamma\tau_v) e^{-i2\pi\gamma\tau_v\Delta t_R} \right) (t_v) \quad (5.50)$$

$$\begin{aligned} \mathcal{F}(2e(\Delta v)e_R(\Delta v)) &= C^2 \frac{v}{4} \int_{-\infty}^{\infty} \tilde{s}(\Delta t) \tilde{a}(\Delta t) \tilde{\sigma}(\Delta t) \tilde{a}_R \tilde{\sigma}_R \\ &\quad \cdot \gamma^2 \left(G(\gamma\tau_v) e^{-i2\pi\gamma\tau_v\Delta t} *_{\tau_v} G(\gamma\tau_v) e^{-i2\pi\gamma\tau_v\Delta t_R} \right. \\ &\quad \left. *_{\tau_v} [\delta(\tau_v + [\Delta t - \Delta t_R]) + \delta(\tau_v - [\Delta t - \Delta t_R])] e^{-i2\pi\tau_v \left[\gamma t_{\phi_1} + \frac{\tilde{\phi}(\Delta t)}{2\pi[\Delta t - \Delta t_R]} \right]} \right) (t_v) d\Delta t, \end{aligned} \quad (5.51)$$

where $*_{\tau_v}$ denotes a convolution over τ_v . Obviously, the accordance of these formulas with the formulas (5.21) to (5.23) will be limited by the filtering kernel

$$G_{filt}(t_v) = \gamma^2 \left(G(\gamma\tau_v) e^{-i2\pi\gamma\tau_v\Delta t} *_{\tau_v} G(\gamma\tau_v) e^{-i2\pi\gamma\tau_v\Delta t_R} \right) (t_v). \quad (5.52)$$

In an ideal case, $G_{filt}(t_v)$ has no effect meaning

$$G_{filt}(t_v) \stackrel{!}{=} \delta(t_v). \quad (5.53)$$

For an exact calculation of this filtering kernel, $G(\gamma\tau_v) = |G(\gamma\tau_v)| e^{i\varphi(\gamma\tau_v)}$ needs to be known. However only the spectral power shape $|G(\gamma\tau_v)|^2$ is known for most laser diodes. The missing phase information $\varphi(\gamma\tau_v)$ is subject to various influences, including the working mechanism of the laser, dispersion effects in the fiber and temporal fluctuations. A simplified analysis, fitting the setup of this work (i.e. small γ , small time difference $|\Delta t - \Delta t_R|$ and reflections with comparable orders of magnitude), is presented in the following.

Due to the symmetry properties of the Fourier transformation, $\varphi(-\gamma\tau_v) = -\varphi(\gamma\tau_v)$ and $|G(\gamma\tau_v)| = |G(-\gamma\tau_v)|$ must hold. For easier calculations, $G(\gamma\tau_v)$ is scaled such that $\int_{-\infty}^{\infty} |G(\gamma t_v)|^2 d\gamma t_v = 1$ is fulfilled. Therefore $\sqrt{\delta(\gamma t_v = 0)}$ is added as multiplication for each kernel $G(\gamma\tau_v)$ in the following formulas (compare to equation (5.41)). Consequentially the filtering kernel according to equation (5.52) can be expressed as

$$G_{filt}(t_v) = \delta(t_v = 0) e^{-i2\pi\gamma t_v \Delta t_R} \int_{-\infty}^{\infty} |G(\nu)| |G(\nu - \gamma t_v)| e^{-i2\pi\nu[\Delta t - \Delta t_R]} e^{i\Delta\varphi_\nu(t_v)} d\nu, \quad (5.54)$$

with

$$\delta(t_v = 0) = \gamma \delta(\gamma t_v = 0) \quad (5.55)$$

$$\nu = \gamma\tau_v \quad (5.56)$$

$$\Delta\varphi_\nu(t_v) = \varphi(\nu) - \varphi(\nu - \gamma t_v). \quad (5.57)$$

The phase difference between two frequencies ν and ν' with frequency difference γt_v is denoted by $\Delta\varphi_\nu(t_v)$ (see equation (5.57)). The emission of frequencies is assumed to be a random process and the phase of the emitted frequencies is assumed to be uniformly distributed (i.e. the emission of a frequency ν or ν' starts at a random moment in time). Therefore the phase difference of the frequencies ν and ν' is assumed to be random based on a uniform distribution

$$\Delta\varphi_\nu(t_v) = \mathcal{U}(-\pi, \pi) \quad (5.58)$$

with $t_v > 0$. Alternatively $\Delta\varphi_{\nu=\gamma\tau_v}(t_v)$ can be sampled over τ_v yielding

$$\Delta\varphi_{\tau_v}(t_v) = \mathcal{U}(-\pi, \pi). \quad (5.59)$$

In this case

$$\int_{\tau_v^{(min)}}^{\tau_v^{(max)}} e^{i\Delta\varphi_{\tau_v}(t_v)} d\tau_v = 0, \quad (5.60)$$

holds, because the integral is proportional to the mean over an endless amount of samples represented by different times τ_v .

The integral of equation (5.54) is transformed to

$$G_{integral}(t_v) = \gamma \int_{-\infty}^{\infty} |G(\gamma\tau_v)| |G(\gamma\tau_v - \gamma t_v)| e^{-i2\pi\gamma\tau_v[\Delta t - \Delta t_R]} e^{i\Delta\varphi_{\tau_v}(t_v)} d\tau_v, \quad (5.61)$$

using equation (5.56). If $|\Delta t - \Delta t_R| \ll \frac{\partial_{\tau_v} \Delta\varphi_{\tau_v}(t_v)}{2\pi\gamma}$, which is either fulfilled for small $|\Delta t - \Delta t_R|$ or small γ , $|G(\gamma\tau_v)| |G(\gamma\tau_v - \gamma t_v)| e^{-i2\pi\gamma\tau_v[\Delta t - \Delta t_R]}$ can be considered to be slowly varying over τ_v compared to $e^{i\Delta\varphi_{\tau_v}(t_v)}$. Accordingly, the integral can be approx-

imated by a sum of integral sections

$$G_{integral}(t_\nu) \approx \gamma \sum_{i \in \mathbb{Z}} |G(\gamma\tau_{\nu,i})| |G(\gamma\tau_{\nu,i} - \gamma t_\nu)| e^{-i2\pi\gamma\tau_{\nu,i}[\Delta t - \Delta t_R]} \int_{\tau_{\nu,i}^{(min)}}^{\tau_{\nu,i}^{(max)}} e^{i\Delta\varphi_{\tau_\nu}(t_\nu)} d\tau_\nu. \quad (5.62)$$

Based on equation (5.60), this leads to

$$G_{integral}(t_\nu) \approx 0, \quad (5.63)$$

if $t_\nu > 0$.

Plugging this result into equation (5.54) yields

$$G_{filt}(t_\nu) = \begin{cases} \delta(t_\nu = 0) \int_{-\infty}^{\infty} |G(\nu)|^2 e^{-i2\pi\nu[\Delta t - \Delta t_R]} d\nu, & t_\nu = 0 \\ 0, & t_\nu \neq 0 \end{cases} \quad (5.64)$$

$$= \delta(t_\nu) \int_{-\infty}^{\infty} |G(\nu)|^2 e^{-i2\pi\nu[\Delta t - \Delta t_R]} d\nu. \quad (5.65)$$

The reason for the shapes $|G(\nu)|$ are broadening mechanism. Equivalent to section 4.2, the broadening leads to a Lorentzian or Gaussian power spectrum $|G(\nu)|^2$. Thus exemplary shapes for $|G(\nu)|^2$ with the FWHM Bandwidth ν_Δ are

$$|G(\nu)|^2 = \frac{2}{\pi\nu_\Delta} \frac{1}{1 + 4\frac{\nu^2}{\nu_\Delta^2}} \quad \text{Lorentzian} \quad (5.66)$$

$$|G(\nu)|^2 = \sqrt{\frac{\ln(16)}{\pi\nu_\Delta^2}} e^{-\ln(16)\frac{\nu^2}{\nu_\Delta^2}} \quad \text{Gaussian,} \quad (5.67)$$

where the functions have been normed such that $\int_{-\infty}^{\infty} |G(\nu)|^2 d\nu = 1$. The corresponding filter functions are

$$G_{filt}(t_\nu) = e^{-\pi\nu_\Delta|\Delta t - \Delta t_R|} \cdot \delta(t_\nu) \quad \text{Lorentzian} \quad (5.68)$$

$$G_{filt}(t_\nu) = e^{-\frac{\pi^2\nu_\Delta^2|\Delta t - \Delta t_R|^2}{\ln(16)}} \cdot \delta(t_\nu) \quad \text{Gaussian.} \quad (5.69)$$

Another more complex approach for a filter kernel analysis of a (Lorentzian) laser source is based on stationary Gaussian phase noise in time domain instead of uniform phase noise in frequency domain. Additionally, instead of assuming that $e(t) \ll e_R(t)$ and either γ or the time difference $|\Delta t - \Delta t_R|$ is small, the simplifying assumption of having only a single reflectivity besides the reference reflectivity is used with the focus on scattering measurements under the influence of a strong Fresnel reflection. The results are presented in [Ven93] and although the calculations are based on different assumptions, the results are identical to the formulas derived in this work – at least

for either small time shifts $\tau_0 = |\Delta t - \Delta t_R| \leq \frac{1}{\pi\nu_\Delta}$ or small frequency slopes γ . In these cases, the transfer function of the measurement system and the sweep range are the limiting factors for spatial accuracy as a Dirac function has no filtering effect on the response.

However, the filtering kernels will decrease the signal strength with an increasing time difference $|\Delta t - \Delta t_R|$. A way to handle this decrease is the definition a *coherence time* t_c , after which the signal has decreased to $\frac{1}{e}$ of its ideal strength. A Lorentzian source is assumed in the following as worst case estimation, because Lorentzian laser sources have a stronger impact on the response strength compared to Gaussian laser sources (see equations (5.68) and (5.69)). Based on equation 5.68, this leads to

$$t_c = \frac{1}{\pi\nu_\Delta}. \quad (5.70)$$

The according reflectometry *coherence length* $x_{coherence}$, i.e. the position difference between reference and fiber reflection that causes a time shift t_c , is

$$x_{coherence} = \frac{v}{2} t_c. \quad (5.71)$$

The maximum position difference to be measured should fulfill

$$\max(L - R, R) \leq x_{coherence} \approx \frac{v}{2\pi\nu_\Delta}. \quad (5.72)$$

Greater position differences are possible, but yield a decreased SNR due to the attenuation of the signal (e.g. as in [Gif07]).

Conclusion

Four different types of scattering or reflections have been mentioned. Raman, Brillouin and Rayleigh scattering as well as Fresnel reflections. In the following the applicability of each reflection type for C-OFDR with respect to the reachable resolution is discussed.

Raman scattering has a bandwidth of about $\nu_\Delta \geq 100$ GHz in silicon [Har70]. Brillouin scattering shows a bandwidth of about $\nu_\Delta \geq 100$ MHz in optical fibers [Par97]. Thus the best case length based on these scatterings can be accomplished using Brillouin scattering

$$\max(L - R, R)_{Brillouin} \leq \frac{v}{2\pi\nu_\Delta} \leq 0.34 \text{ m}, \quad (5.73)$$

using the refractive index $n \approx 1.5$. This length constraint might suffice in some cases. However, Brillouin scattering introduces an additional strain dependent frequency shift, that has to be compensated in order to measure Brillouin scattering with C-

OFDR techniques. Such a compensation could be done by frequency shifting the reference reflection using an acousto-optic modulator (similar to *Self-Heterodyne Linewidth Measurements* [Oko80]). However, a modulator introduces additional bandwidths, circuitry and thus limitations and might even destroy the laser coherence. Additionally, the needed frequency shift is not exactly known and subject to temperature and strain effects. Another possible way would be to increase γ such that the Brillouin frequency shift occurs as simple position shift, since the frequency changes along the fiber according to the sweep speed γ and the propagation speed of the light. However, the maximum measurable distance is strongly limited due to the bandwidth of Brillouin scattering and γ would need to be unreasonable large in order to shift the Brillouin scattering to a measurable distance. For these reasons, Raman or Brillouin measuring do not seem to be reasonable using C-OFDR. The last remaining reflection types are Rayleigh scatterings (parasitic due to manufacturing) or intentional reflections not shifting the frequency, where intentional reflections yield higher signals and thus higher SNRs. This is one reason why this work focuses on fiber Bragg gratings (i.e. user induced reflections).

A laser with bandwidth $\nu_\Delta \approx 100$ kHz was used, leading to a coherence length limitation of

$$\max(L - R, R) \leq 300 \text{ m.} \quad (5.74)$$

Accordingly the length of this system will be limited by the stepsize $s_{\Delta v}$ and not by the laser bandwidth. The upper limit for the fiber length is therefore about 0.4 m for $s_{\Delta v} \approx 125$ GHz (corresponding 1 pm at 1550 nm) and the attenuation caused by the laser coherence is negligible.

5.3.3 Reflectivity Value Based Measurement

A possible measurement variable is the amount of reflected power at a position x (or likewise the reflectivity value). Yet the reflectivity value is a scale variant measurement variable. Therefore a proper normalization measure must be found.

The fraction $\sigma(x) \cdot \epsilon$ of light scattered between position x and $x + \epsilon$ can be computed using the assumption that the attenuation $a(x)$ in the fiber is only caused by reflections or scatterings (i.e. no light is absorbed). If ϵ is assumed to be small, the scattered fraction is

$$\sigma(x)\epsilon = \overbrace{a(x)}^{\text{attenuation during backpropagation}} \sqrt{1 - \underbrace{\frac{a(x+\epsilon)^2}{a(x)^2}}_{\text{transmitted power at } x}} = \sqrt{a(x)^2 - a(x+\epsilon)^2} \stackrel{\epsilon \rightarrow 0}{\approx} \sqrt{-\frac{d}{dx}a(x)^2}\epsilon. \quad (5.75)$$

This formula leads to the differential equation

$$a(x)\sigma(x) = a(x)\sqrt{-\frac{2a(x)a'(x)}{\epsilon}}. \quad (5.76)$$

Assuming $a(x)\sigma(x)$ as known function and resolving for $a(x)$ yields

$$a(x) = \sqrt[4]{a(0)^4 - 2\epsilon \int_0^x a(\tilde{x})^2 \sigma(\tilde{x})^2 d\tilde{x}}. \quad (5.77)$$

ϵ can be replaced if some value $a(L)$ is known:

$$\epsilon = \frac{a(0)^4 - a(L)^4}{2 \int_0^L a(\tilde{x})^2 \sigma(\tilde{x})^2 d\tilde{x}} \quad (5.78)$$

$$a(x) = \sqrt[4]{a(0)^4 - \frac{\int_0^x a(\tilde{x})^2 \sigma(\tilde{x})^2 d\tilde{x}}{\int_0^L a(\tilde{x})^2 \sigma(\tilde{x})^2 d\tilde{x}} [a(0)^4 - a(L)^4]}. \quad (5.79)$$

Two interesting extreme cases exist

$$a(x) \approx \begin{cases} a(0) & a(L > x) \approx a(0) \\ a(0) \sqrt[4]{1 - \frac{\int_0^x a(\tilde{x})^2 \sigma(\tilde{x})^2 d\tilde{x}}{\int_0^L a(\tilde{x})^2 \sigma(\tilde{x})^2 d\tilde{x}}} & a(L) \approx 0 \end{cases}. \quad (5.80)$$

Therefore, a scale invariant measurement variable depending on the amount of reflected power can be developed for the latter case. Although the attenuation $a(x)$ includes all reflections until position x , this dependence can be removed by solving the *Beer-Lambert-Law* $a(x)^2 = e^{-\int_0^x \alpha(x)}$ for the *attenuation coefficient* $\alpha(x)$ [Fan12] [Eic81]. Note that $a(0) = 1$, according to the *Beer-Lambert-Law*. However, in the scope of this work, the assumption of the first case is fulfilled as the fiber is rather short. Accordingly, $a(x) \approx a(0) = 1$ is assumed in the following and another method to get a scale invariant measurement variable is derived.

Using equation (5.34) and $2a(R)\sigma(R) \ll \frac{\tilde{a}_R \tilde{\sigma}_R}{\Delta x}$ leads to

$$\left| I_R \left(\pm 2 \frac{|x-R|}{v} \right) \right| \propto C^2 \frac{v}{4} \tilde{a}_R \tilde{\sigma}_R \cdot \begin{cases} \frac{\tilde{a}_R \tilde{\sigma}_R}{\Delta x} & 0 = |x-R| \\ a(x)\sigma(x) & |x-R| > \min(R, |L-R|) \end{cases}. \quad (5.81)$$

Consequently, the measurement can be normalized by

$$\left| \frac{I_R \left(\pm 2 \frac{|x-R|}{v} \right)}{I_R(0)} \right| \approx \frac{a(x)\sigma(x)}{\tilde{a}_R \tilde{\sigma}_R} \Delta x \approx \frac{\sigma(x)}{\tilde{a}_R \tilde{\sigma}_R} \Delta x \quad \text{for } |x-R| > \min(R, |L-R|). \quad (5.82)$$

This normalization depends on the stability of the reference reflection $\tilde{a}_R \tilde{\sigma}_R$, which is why a stable reference reflection must be ensured. The reflectivity $\sigma(x)$ is independent

of previous reflections in case of a constant $a(x) \approx 1$ and is directly proportional to the reflected signal at position x (compare to equation (5.75)).

5.3.4 Position Based Measurement

An interesting feature for measuring purposes is the position of the reflectivities. Positions have the advantage of being scale invariant. However, position changes due to temperature or strain are very small compared to the absolute position and high resolutions are necessary to track them. If the resolution is too low, position changes will show up as changes in the magnitude of the reflection and its respective phase shift rather than a spatial position change. The reflection magnitude is scale variant and subject to other influences, phase values are periodic and therefore ambiguous. A method to overcome these disadvantages is combining several phase measures in a certain region with the cost of a decreased spatial accuracy. The most straightforward way to combine different phase values at different positions with different weights is a superposition of waves each having a different phase shift and amplitude. In complex representation the amplitude of the superposition of waves with frequency $\Delta\nu$ can be written as

$$P(\Delta\nu) = \left| \int_{t_{v_{min}}}^{t_{v_{max}}} I_R(t_v) e^{i2\pi t_v \Delta\nu} dt_v \right|, \quad (5.83)$$

where $I_R(t_v)$ incorporates the phase shift and amplitude caused by reflections and $2\pi t_v \Delta\nu$ is the phase shift caused by the respective position. A short introduction in complex wave representation and its benefits for amplitude calculation can be found in [Sir93, p. 9f]. This method is for example used for interferometers, where the combination of specially chosen phase values can lead to a favored frequency having the highest response of all frequencies. If the reflections in the fiber are chosen such that $P(\Delta\nu)$ exhibits a favored frequency $\Delta\nu$, this frequency would be a good and ideally scale invariant measurement variable for position changes in the fiber.

In the following, it is shown that this superposition is proportional to the spectral response of a certain fiber section. The response amplitude of a fiber section with respect to a certain frequency ν and a unity input amplitude $C = 1$ is (similar to equation (5.17) for $\gamma = 0$)

$$|e(\nu)| = |e(\nu)^*| = \left| \int_{x_{min}}^{x_{max}} a(x) \sigma(x) e^{i2\pi\nu \frac{2x}{v} - i\phi(x)} dx \right|, \quad (5.84)$$

where $2\pi\nu \frac{2x}{v}$ models the time delay due to the position x and $\phi(x)$ the phase shift caused by the reflection at position x . Assuming $x > 2R$, $2a(R)\sigma(R) \ll \frac{\tilde{a}_R \tilde{\sigma}_R}{\Delta x}$ as well as $\gamma [\Delta t_R + \frac{x-R}{v}] \approx 0$ (which is especially true for short fibers), it is known from equa-

tions (5.34) and (5.82) that

$$a(x)\sigma(x) \approx \frac{\tilde{a}_R \tilde{\sigma}_R}{\Delta x} \frac{I_R\left(2\frac{x-R}{v}\right)}{I_R(0)} \approx \frac{\tilde{a}_R \tilde{\sigma}_R}{\Delta x} \frac{I_R\left(2\frac{x-R}{v}\right)}{I_R(0)} e^{-i4\pi\frac{x-R}{v}\nu_0 + i\phi(x)}. \quad (5.85)$$

Combining the above equations yields

$$|e(\nu)| \approx \left| \int_{x_{min}}^{x_{max}} \frac{\tilde{a}_R \tilde{\sigma}_R}{\Delta x} \frac{I_R\left(2\frac{x-R}{v}\right)}{I_R(0)} e^{i2\pi\left[-2\frac{x-R}{v}\nu_0 + 2\frac{x-R}{v}\nu + 2\frac{R}{v}\nu\right]} dx \right| \quad (5.86)$$

$$= \left| \int_{x_{min}}^{x_{max}} \frac{\tilde{a}_R \tilde{\sigma}_R}{\Delta x} \frac{I_R\left(2\frac{x-R}{v}\right)}{I_R(0)} e^{i2\pi 2\frac{x-R}{v}[\nu - \nu_0]} dx \right| \quad (5.87)$$

$$= \Delta\nu_{max} \frac{\tilde{a}_R \tilde{\sigma}_R}{I_R(0)} \left| \int_{2\frac{x_{min}-R}{v}}^{2\frac{x_{max}-R}{v}} I_R(t_\nu) e^{i2\pi t_\nu[\nu - \nu_0]} dt_\nu \right|. \quad (5.88)$$

The last formula is proportional to the calculation of $P(\Delta\nu)$. The integral corresponds to an inverse Fourier transformation of $I_R(t_\nu)$ in a window from $t_{\nu_{min}} = 2\frac{x_{min}-R}{v}$ to $t_{\nu_{max}} = 2\frac{x_{max}-R}{v}$.

Summing up, the relationship between $P(\nu - \nu_0)$, $|e(\nu)|$ and $I_R(t_\nu)$ is

$$P(\nu - \nu_0) \propto |e(\nu)| \approx \Delta\nu_{max} \frac{\tilde{a}_R \tilde{\sigma}_R}{I_R(0)} \left| \mathcal{F}^{-1}(s_{range} I_R)(\nu - \nu_0) \right|, \quad (5.89)$$

where $s_{range}(t_\nu)$ is a rectangular window from $t_{\nu_{min}} = 2\frac{x_{min}-R}{v}$ to $t_{\nu_{max}} = 2\frac{x_{max}-R}{v}$ and x_{min} must fulfill the condition $x_{min} > 2R$. Therefore the spectral responses of single fiber sections can be calculated by an inverse Fourier transformation of this section.

The use for measurement can be enhanced if the reflectivities in the fiber are chosen to develop high peak responses – for example if the reflectivities form a Fiber Bragg Grating. In this case the result of the inverse Fourier transformation will show peaks (like in case of interferometer responses), where the peak position will be influenced by the reflection positions. Accordingly, the scale invariant measurement variable based on the reflection positions is

$$\nu_{peak} = \arg \max_{\nu} \left| \mathcal{F}^{-1}(s_{range} I_R)(\nu - \nu_0) \right|. \quad (5.90)$$

[Chi01] and [Yük11] used this approach to determine the distributed spectral responses of Fiber Bragg Gratings for measuring strain or temperatures.

Due to the advantages of Fiber Bragg Gratings for sensing purposes, it is assumed in the following that the reflectivities in the fiber form Fiber Bragg Gratings.

5.3.5 Fitting Functions

Fiber Bragg gratings change their reflection wavelength proportional to the effective refractive index n_{eff} and the grating length L

$$\frac{c}{\nu_{peak}(T)} = \lambda_{peak}(T) \propto L n_{eff}. \quad (5.91)$$

n_{eff} is thereby defined as the average effective refractive index $n_{eff} = \frac{n_{eff,high} + n_{eff,low}}{2}$ [Erd97], where $n_{eff,high}$ and $n_{eff,low}$ are the effective refractive indices of the grating sections. According to manufacturer technical informations, e.g. [SNA08], the refractive indices of optical fibers show a positive polynomial dependency to temperature with a degree of three. Lengths are known to have a positive affine temperature behavior for most materials [Lid00]. Just like in chapter 4, it is assumed that the small temperature range of only 40 K allows an affine approximation of $L n_{eff}$. This assumption is also justified by the measurements shown in [Fer00] suggesting an affine temperature dependency of the Bragg reflection wavelength.

The corresponding Bragg peak reflection power according to [Erd97] for a uniform fiber grating with constant effective index perturbation (i.e. a rectangular apodization) of length L is

$$|e(\nu_{peak})|^2 = \tanh^2 \left(\frac{\pi \nu_{peak}}{2c} L \Delta n_{eff} \right), \quad (5.92)$$

where c denotes the speed of light and Δn_{eff} the difference of the induced effective index perturbation $\Delta n_{eff} = n_{eff,high} - n_{eff,low}$. Using equation (5.89) leads to

$$L \Delta n_{eff} \approx \frac{2\lambda_{peak}}{\pi} \operatorname{artanh} \left(\Delta \nu_{max} \frac{\tilde{a}_R \tilde{\sigma}_R}{I_R(0)} \left| \mathcal{F}^{-1}(s_{range} I_R)(\nu_{peak} - \nu_0) \right| \right). \quad (5.93)$$

As $\tilde{a}_R \tilde{\sigma}_R$ must be assumed to be unknown, this function would require a nonlinear fitting in order to connect the temperature dependency of $L \Delta n_{eff}$ with the measurement $\left| \mathcal{F}^{-1}(s_{range} I_R)(\nu - \nu_0) \right|$. However in case of a weak grating $L \Delta n_{eff} \ll \frac{2\lambda_{peak}}{\pi}$ (i.e. the result of $\operatorname{artanh}(\cdot)$ is $\ll 1$), $\operatorname{artanh}(\cdot)$ can be replaced with a simple proportionality. Additionally, assuming $\tilde{a}_R \tilde{\sigma}_R$ is constant yields

$$\frac{\left| \mathcal{F}^{-1}(s_{range} I_R)(\nu_{peak} - \nu_0) \right|}{I_R(0)} \propto \frac{L \Delta n_{eff}}{\lambda_{peak}} \propto \frac{\Delta n_{eff}}{n_{eff}}. \quad (5.94)$$

Note that this equation is directly influenced by the scale of $\frac{I_R(t_\nu)}{I_R(0)}$ and therefore, according to equation (5.82), by the reflection values $\sigma(x)$ in the range of s_{range} . Thus, this measurement expands the single position measurement $\sigma(x)$ to a measurement of $\sigma(x)$ in a range x_{min} to x_{max} . However, measurements performed in [Guo06] show

no temperature dependency of the intensity $|e(\nu_{peak})|$, yet this result will be rechecked and evaluated in section 5.3.6. Just like for the reflection wavelength, it is assumed that an affine function yields satisfying accuracies for the fitting of the rational function $\frac{\Delta n_{eff}}{n_{eff}}$ due to the small temperature range of 40 K.

To sum up, the following relations are used for the peak frequency and the reflectivity value

$$|e_{norm}(\nu)| = \frac{|\mathcal{F}^{-1}(s_{range} I_R)(\nu - \nu_0)|}{I_R(0)} \quad (5.95)$$

$$\nu_{peak} = \arg \max_{\nu} |e_{norm}(\nu)| \quad (5.96)$$

$$\frac{c}{\nu_{peak}(T)} \approx \begin{pmatrix} 1 & T \end{pmatrix} \begin{pmatrix} C_{freq} \\ C_{T,freq} \end{pmatrix} \quad (5.97)$$

$$|e_{norm}(\nu_{peak})| \approx \begin{pmatrix} 1 & T \end{pmatrix} \begin{pmatrix} C_{refl} \\ C_{T,refl} \end{pmatrix}. \quad (5.98)$$

These fitting functions are targeted at uniform fiber Bragg gratings with rectangular apodization as sensing reflectivities. They generate two equations based on the same region x_{min} to x_{max} rather than a single position x . The fact that both equations are based on the same region is important for a proper combination of both equations for compensation applications (which is one reason why the fitting is based on $|e_{norm}(\nu)|$ instead of $\sigma(x)$).

As these fitting functions are entirely targeted at fiber Bragg responses, one might wonder if (besides peak wavelength and reflectivity) the linewidth of the fiber Bragg spectrum is usable for sensing. As reflectometry techniques need weak gratings in order to reduce attenuation at longer distance sensing points, the linewidth of the responses is (according to [Erd97]) $\Delta\lambda \approx \frac{2}{N}\lambda_{peak}$, where N is the amount of grating periods. Therefore the linewidth does not add any additional information and is more difficult to measure than the peak wavelength λ_{peak} . In case of strong gratings, the linewidth can be calculated by $\frac{\Delta\lambda}{\lambda_{peak}} \approx \frac{\Delta n_{eff}}{n_{eff}}$ and shows the same dependency as the reflection intensity $|e_{norm}(\nu)|$ for weak gratings, which is analyzed in the following.

5.3.6 Experimental Results

For the coherent OFDR approach, an external cavity laser was tuned from $\nu_{max} = 193.64$ THz to $\nu_{min} = 193.45$ THz (1548.2 nm to 1549.7 nm) leading to an expected spatial accuracy of roughly $\frac{v}{2(\nu_{max} - \nu_{min})} \approx 0.5$ mm (equation (5.35)). The reference reflection was placed relatively near to the coupler, thus the maximal fiber length was about $L \leq 0.4$ m. The refractive index of the fiber was thereby assumed to be $n \approx 1.5$.

The interferometer was designed with a peak distance of $s_{\Delta\nu} = 125$ MHz (about 1 pm at 1550 nm). The peaks are used to mark the correct sampling points for the measurement photodiode response in order to achieve an almost constant stepsize $s_{\Delta\nu}$. To be able to have comparable measurements over the exact same frequency range, a wavelength reference based on a cyanide gas cell was used in order to initialize and stop the measurement. The measured reflection power was normalized with a reference photodiode measuring the current output power of the laser. The schematic of this setup was already introduced in figure 5.2.

The sweep responses of the interferometer, the reference wavelength and the reference photodiode were measured along with the sweep response of the fiber from the measurement photodiode. The correct sampling, start and stop positions were interpolated in software by detecting the corresponding peak positions in the response of the interferometer and the wavelength reference respectively, and by interpolating the fiber response at those time indices. The normalization of the signal was done in software, as well.

Four fiber Bragg gratings were implemented in the fiber under test in order to get peaks in the spectral response that are suitable for position based measurements. Each FBG has a reflection wavelength of about 193.5 THz (1549.3 nm), a length of about 10 mm and a grating period in the order of 0.5 μm (thus, the grating itself is not visible in the measurement, but the overall structure is). The gratings were written to a reflectivity of 1 – 2% to comply with the assumption of negligible attenuation along the fiber (equation (5.82)).

One measured example for $i_R(\Delta\nu)$ is shown in figure 5.4. The corresponding Fourier transformation, i.e. $\sigma(x)$, is shown in figure 5.5. Examples for the normalized spectral response $|e_{norm}(\Delta\nu)|$ of selected fiber sections are shown in figure 5.6. The frequency shift $\Delta\nu$ expresses the difference $\Delta\nu = \nu - \nu_{min}$ between the current frequency and the smallest used frequency.

The temperatures were tuned by fixing the fiber under test onto a TEC device, such that only the two fiber Bragg gratings in the mid section had contact to the TEC, and applying temperatures in the range from 283 K to 323 K. The measurements were fitted with affine functions and repeatedly evaluated over 7 mW and 8 mW laser emission powers in order to test the robustness. All peak measurements have been interpolated using quadratic interpolation.

The result for the position based measurement is shown in figure 5.7, the results for the reflectivity value based measurement in figure 5.8. Using an affine function approximates the behavior of the peak wavelength over temperature with sufficient accuracy and provides an accurate way to determine the temperature. The temperature sensitivity is $C_{T, freq} = 9.4 \frac{\text{pm}}{\text{K}}$ for FBG #2 and $C_{T, freq} = 9.8 \frac{\text{pm}}{\text{K}}$ for FBG #3. The reflectivity value, however, does not show a significant temperature behavior. This is why the

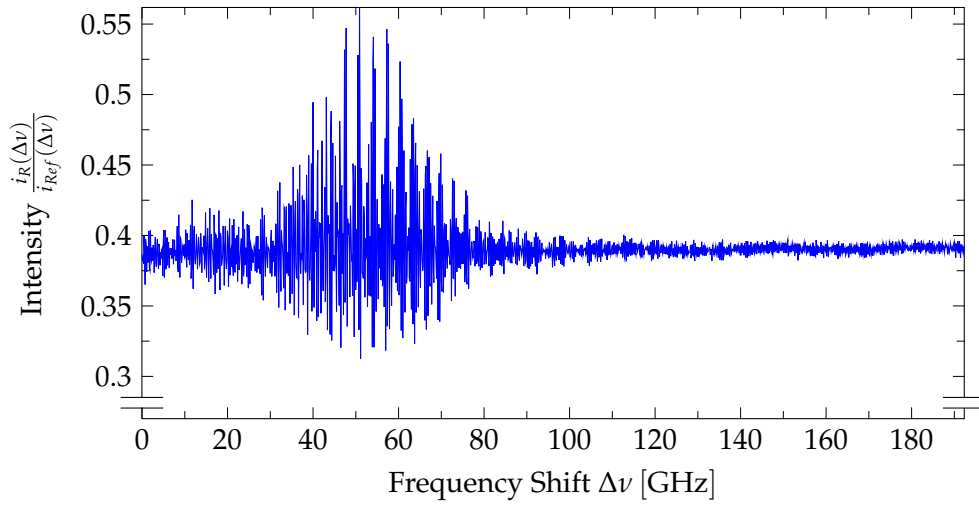


Figure 5.4: An example for the measurement of $i_R(\Delta\nu)$ relative to the reference measurement $i_{Ref}(\Delta\nu)$, i.e. the intensity directly measured by the measurement photodiode normalized by the reference photodiode readings. The laser power was 7 mW and the TEC temperature 293 K. The fiber had four FBGs, each having a reflection wavelength of about 193.5 THz.

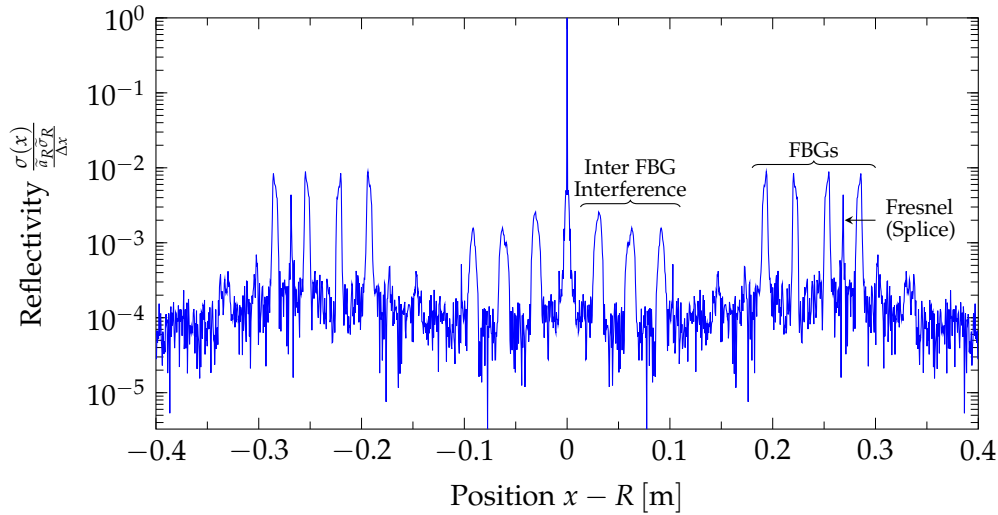


Figure 5.5: An example for a measurement of $\sigma(x)$ relative to $\frac{\tilde{a}_R \tilde{\sigma}_R}{\Delta x}$, i.e. the absolute value of the fast Fourier transformation for $i_R(\Delta\nu)$ corresponding to figure 5.4 normalized by $I_R(0)$ (see equation (5.82)). The four fiber Bragg Gratings are clearly visible (broad peaks), as well as one Fresnel reflection (narrow peak) caused by bad splicing. Also visible are three weak peaks near the origin. Those peaks are caused by the interference between the Fiber Bragg Gratings (i.e. one Fiber Bragg Grating has the effect of a reference reflection).

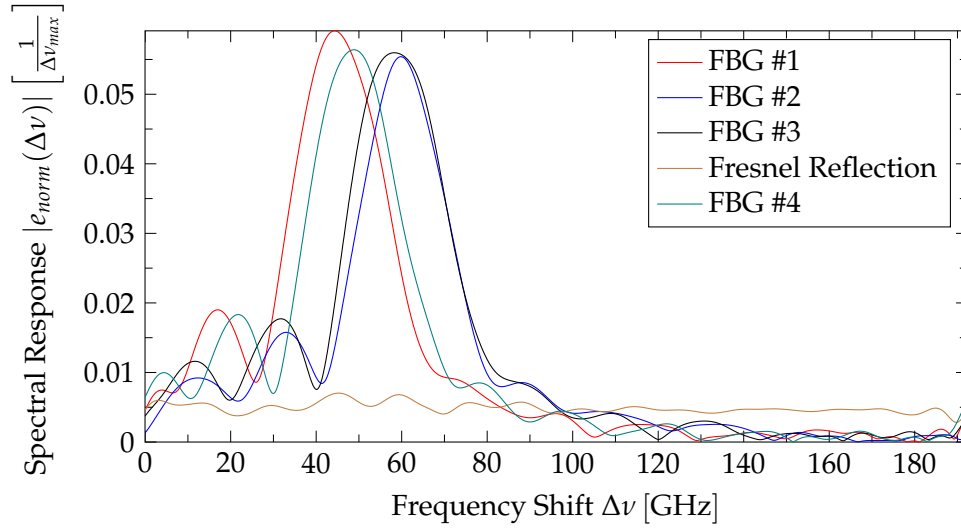


Figure 5.6: Examples for a measurement of $|e_{norm}(\Delta\nu)|$, i.e. the sectionwise inverse fast Fourier transformation for the five strongest peaks in figure 5.5 (see equation (5.89) and (5.95)). Note that figure 5.5 only shows an absolute value. The inverse Fourier transformation additionally uses the complex phase not shown in figure 5.5. The ordering represents the distance, thus the first FBG is the nearest to the reference reflection. The advantage of having fiber Bragg gratings for tracking changes of the peak frequency ν_{peak} is obvious as Fresnel reflections have no well defined peak. The repetition of the response in the high frequency shift region is due to the discrete Fourier transformation.

reflectivity value can be assumed to be constant over temperature making it unusable for temperature sensing.

Figure 5.9 shows the accuracy of the peak wavelength approach (i.e. figure 5.7) over the different laser powers. The results are stable over the laser powers and an accuracy of about ± 0.35 K (standard deviation) can be reached. This is in good accordance with the expected accuracy of the setup – i.e. the accuracy of the applied temperature by the TEC.

High precision distributed temperature sensing can be realized with distributed fiber Bragg gratings by using the wavelength shift of the gratings. However the reflectivity value seems to be independent of temperature (which was confirmed in [Guo06]). But the reflectivity value might be solely strain dependent, in which case no temperature compensation is necessary for proper strain measurement. Unfortunately this is improbable, as properties induced by strain changes are mostly results of the changed elongation of the fiber under test. Because temperature changes the elongation as well (amongst others), a temperature dependence must exist if a strain dependence exists. If there is no temperature dependence, then there is most likely no strain dependence.

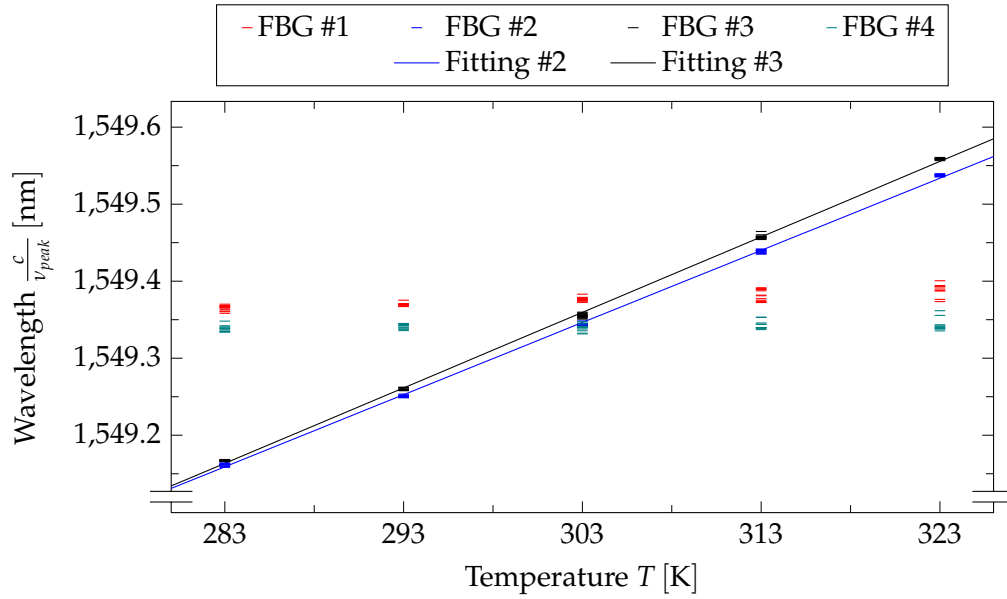


Figure 5.7: The resulting behavior of $\frac{c}{\nu_{peak}}$ over temperature under the influence of different laser powers can be seen for all fiber Bragg gratings along with the corresponding fitting function. The second and third Fiber Bragg Grating was used for temperature tracking (compare to figure 5.6). The coefficients for the affine fitting function were $C_{freq} = 1547 \text{ nm}$ and $C_{T,freq} = 9.4 \frac{\text{pm}}{\text{K}}$ for FBG #2 and $C_{freq} = 1546 \text{ nm}$ and $C_{T,freq} = 9.8 \frac{\text{pm}}{\text{K}}$ for FBG #3, respectively.

Summing up, although this approach can be used to gain two equation systems, only one equation is usable for temperature or strain sensing. Under these circumstances simultaneous measurement of temperature and strain is impossible in the exact same location.

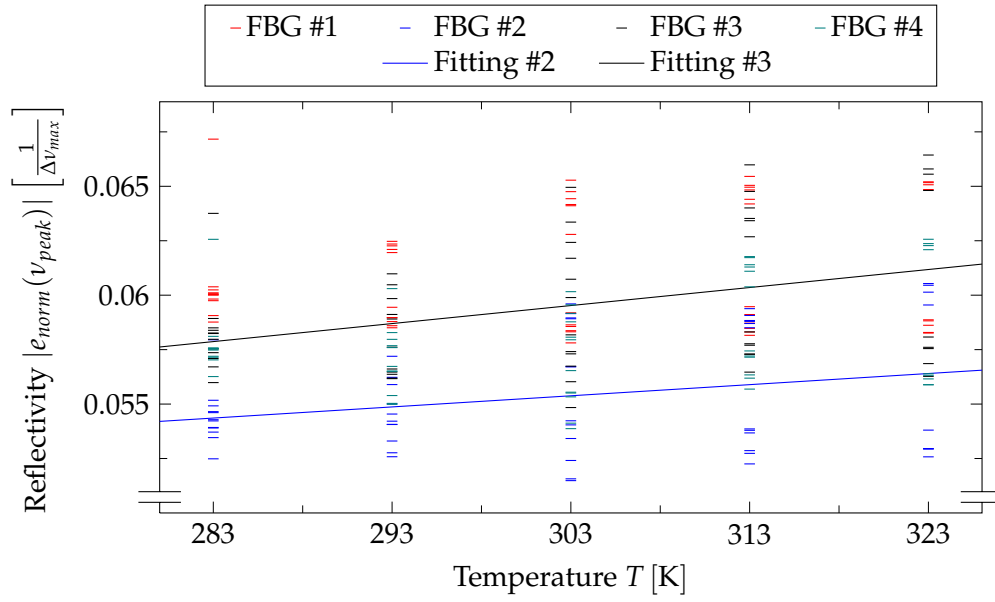


Figure 5.8: The resulting behavior of $|e_{\text{norm}}(v_{\text{peak}})|$ over temperature under the influence of different laser powers can be seen along with the corresponding fitting function. The second and third Fiber Bragg Grating was used for temperature tracking (compare to figure 5.6). The coefficients for the affine fitting function were $C_{\text{refl}} = \frac{399 \cdot 10^{-4}}{\Delta v_{\text{max}}}$ and $C_{T,\text{refl}} = \frac{0.51 \cdot 10^{-4}}{\Delta v_{\text{max}} \text{K}}$ for FBG #2 as well as $C_{\text{refl}} = \frac{344 \cdot 10^{-4}}{\Delta v_{\text{max}}}$ and $C_{T,\text{refl}} = \frac{0.83 \cdot 10^{-4}}{\Delta v_{\text{max}} \text{K}}$ for FBG #3. Obviously, there is almost no difference in the response between the tempered FBGs #2 or #3 and the non-tempered FBGs #1 or #4. For this reason, the response is assumed to be independent of temperature and the differing responses are likely to have another origin (possibly the increasing temperature of the measuring circuit).

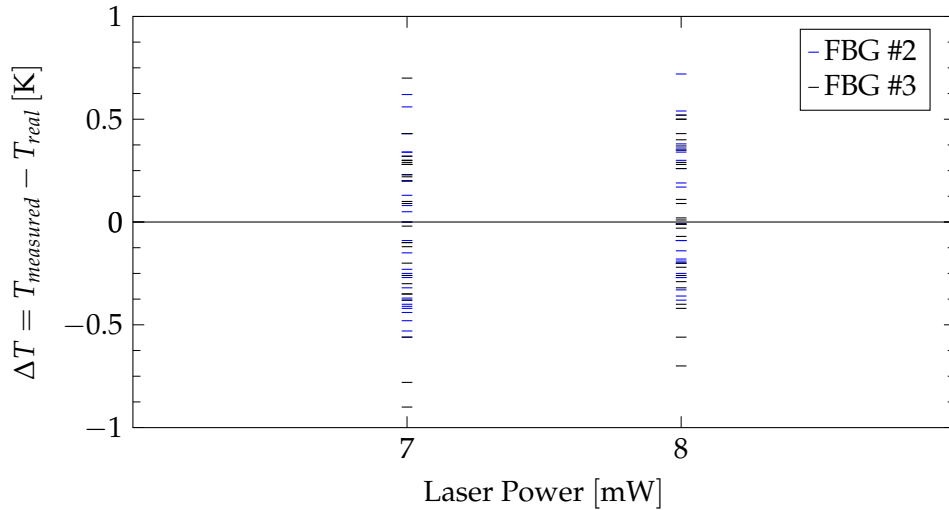


Figure 5.9: The difference between measured and applied temperature over different laser powers is shown for the position based (wavelength changes) approach depicted in figure 5.7. The reached accuracy is about ± 0.35 K (standard deviation).

6 Conclusion

Different approaches for fiber optic temperature sensing with possible strain measurement have been analyzed for short fiber segments: using the fluorescence lifetimes of doped fibers, tracking the lowpass effect of the emission spectrum of doped fibers and determining reflection positions and magnitudes based on distributed Fiber Bragg Gratings.

The fluorescence lifetime proved to be significantly sensitive to noise limiting the obtainable temperature accuracies to over ± 15 K. The magnitude of reflections exhibited temperature constant behavior making simultaneous temperature and strain measurement using reflection magnitudes and positions impossible. Doped fiber approaches based on the emission spectrum instead of the lifetime proved to be a robust and strain independent possibility for temperature measurement. However, the temperature accuracy obtained is rather low (max. ± 2 K deviation in case of Ytterbium) and limits the accuracy of compensation. Yet, different dopings may show higher temperature sensitivities, thus increasing the accuracy. Self heating due to the energy loss between absorption and emission is a possible source for additional measurement errors.

Important relationships for the fluorescence lifetime have been derived, yielding the most accurate model function of fluorescence decay to the author's knowledge. Even a dependence of the fluorescence lifetime to the current excitation power has been shown.

Additionally, a connection between absorption, stimulated emission, spontaneous emission and the measured spectrum has been developed for a two level system based on the fluorescence decay model found. The measured spectrum is thereby considered as the steady state result of a dynamic system influenced by spontaneous emission, amplified stimulated emission, reabsorption, stimulated emission and absorption. The result suggests that the measured spectrum is close to the absorption spectrum and not to the emission spectrum – at least in case of Ytterbium and in the range of the minor emission peak. A dependence of the spectrum to the excitation power has been shown. However, this dependence is negligibly weak for high excitation powers. The results emphasize the need to treat the measured spectrum as the steady state of a dynamic system rather than an approximated representation of internal absorption and emission spectra.

Finally, different reflectometry techniques have been presented for distributed reflection or scattering measurement including their limitations. The target application of this work strictly restricts the usable reflectometry techniques to the coherent optical domain reflectometry (C-OFDR), whose resolution and range are primarily limited by the Fourier transformation and not by the laser properties. Brillouin and Raman scattering effects have been shown to be unsuitable for C-OFDR based approaches. A way to track reflectivity position changes with magnitudes lower than the reached resolution was presented. Actually spectral responses of spatially distributed Fiber Bragg Gratings have been calculated using a single measurement.

Summing up the favored approach for temperature compensation is analyzing the spectrum of excited doped fibers (using fluorescence intensity ratios to track lowpass effects in the spectrum and/or spectral shifts to track Fourier domain phase changes applied by the lowpass), where the optimal doping material is subject of further research. If a dopant is used that is not accurately modeled by a two level system, special care must be taken that the dopant possesses an operating point with excitation independent spectral properties.

List of Figures

1.1	MiroSurge System for Minimally Invasive Robotic Surgery	2
1.2	Fiber Optic Strain Sensor Based on Fiber Bragg Gratings	2
2.1	Birefringent Fiber Interferometry	7
2.2	Tilted Fiber Bragg Grating	10
2.3	Energy Levels of Erbium and Ytterbium	14
3.1	Transition of Electrons by Absorption and Emission	21
3.2	Fluorescence Lifetime Measurement Setup	28
3.3	Decay of Fluorescence Intensity	29
3.4	Fluorescence Lifetime and Residual Norm over Excitations	30
3.5	Fluorescence Lifetime and Residual Norm for Simulated Measurements	31
3.6	Fluorescence Lifetimes over Temperature	32
4.1	Ytterbium Spectral Cross Sections	36
4.2	Ytterbium Measurement Factors	38
4.3	Spectral Measurement Setup	48
4.4	Measured Ytterbium Emission Spectrum	49
4.5	Ytterbium Second Peak in the Emission Spectrum	49
4.6	Fluorescence Intensity Ratio Measurement	50
4.7	Ytterbium Emission Spectrum in Fourier Domain	51
4.8	Fourier Domain Intensity Ratio Measurement	52
4.9	Accuracy of the Temperature Measurement using the Spectrum	53
5.1	Sketch of NA-OFDR Measurement Setup	56
5.2	Sketch of Coherent OFDR Setup	60
5.3	Sketch of Alternative Coherent OFDR Setup	61
5.4	Example Plot for $i_R(\Delta\nu)$	77
5.5	Example Plot for $\sigma(x)$	77
5.6	Example Plot for $ e_{norm}(\Delta\nu) $	78
5.7	Measured $\frac{c}{\nu_{peak}}$ over Temperature for Ytterbium	79
5.8	Measured $ e_{norm}(\nu_{peak}) $ over Temperature for Ytterbium	80
5.9	Accuracy of OFDR Based Temperature Measurement	80

List of Tables

2.1 Summary of Temperature Dependent Properties in Fibers 17

3.1 Notation Used for Fluorescence Calculations 20

Bibliography

- [Ala05] M. N. Alahbabi, Y. T. Cho and T. P. Newson: *Simultaneous Temperature and Strain Measurement with Combined Spontaneous Raman and Brillouin Scattering*, Optics Letters **30**, 1276 (2005). Cited on page 16.
- [Bar76] M. K. Barnosk and S. M. Jensen: *Fiber Waveguides: a Novel Technique for Investigating Attenuation Characteristics*, Applied Optics **15**, 2112 (1976). Cited on page 57.
- [Bax96] G. W. Baxter, S. A. Wade, S. F. Collins, G. Monnom and E. Maurice: *Rare-Earth-Doped Optical Fibers for Point Temperature Sensing*, Proc. SPIE **2841**, 249 (1996). Cited on page 42.
- [Bel03] A. Bellemare: *Continuous-Wave Silica-Based Erbium-Doped Fibre Lasers*, Progress in Quantum Electronics **27**, 211 (2003). Cited on page 14.
- [Bow05] S. R. Bowman, S. P. O'Connor and S. Biswal: *Ytterbium Laser With Reduced Thermal Loading*, IEEE Journal of Quantum Electronics **41**, 1510 (2005). Cited on pages 19 and 26.
- [Che07] E. Chehura, S. W. James and R. P. Tatam: *Temperature and Strain Discrimination Using a Single Tilted Fibre Bragg Grating*, Optics Communications **275**, 344 (2007). Cited on pages 9 and 12.
- [Chi01] B. A. Childers, M. E. Froggatt, S. G. Allison, S. T. C. Moore, D. A. Hare, C. F. Batten and D. C. Jegley: *Use of 3000 Bragg Grating Strain Sensors Distributed on Four 8-m Optical Fibers During Static Load Tests of a Composite Structure*, in SPIE's 8th Annual International Symposium on Smart Structures and Materials, International Society for Optics and Photonics, 2001, 133–142. Cited on page 73.
- [Ciu05] E. W. Ciurczak: *Revisiting the Polarization Interferometer*, Spectroscopy **20**, 68 (2005). Cited on page 6.
- [Col02] S. F. Collins, G. Baxter, S. Wade and P. Farrell: *Strain dependence of Fluorescence from Rare-Earth-Doped Optical Fibres: Application to the Simultaneous, Co-located, Measurement of Strain and Temperature*, Composite Structures **58**, 373 (2002). Cited on pages 13, 15, 18, and 27.

- [De 01] K. De Souza and T. P. Newson: *Improvement of Signal-to-Noise Capabilities of a Distributed Temperature Sensor Using Optical Preamplification*, Measurement Science and Technology **12**, 952 (2001). Cited on page 16.
- [Dem11] W. Demtröder: *Linienbreiten und Profile von Spektrallinien*, in *Laserspektroskopie 1*, Springer-Verlag, 2011. Cited on pages 39, 40, and 49.
- [Dol88] D. W. Dolfi, M. Nazarathy and S. A. Newton: *5-mm-resolution optical-frequency-domain reflectometry using a coded phase-reversal modulator*, Optics Letters **13**, 678 (1988). Cited on page 55.
- [Don10] Y. Dong, L. Chen and X. Bao: *Truly Distributed Birefringence Measurement of Polarization-Maintaining Fibers based on Transient Brillouin Grating*, Optical Letters **35**, 193 (2010). Cited on page 8.
- [Don11] X. Dong, H. Zhang, B. Liu and Y. Miao: *Tilted Fiber Bragg Gratings: Principle and Sensing Applications*, Photonic Sensors **1**, 6 (2011). Cited on page 10.
- [Dre12] P. Drexler and P. Fiala: *Optical Fiber Birefringence Effects – Sources, Utilization and Methods of Suppression*, in D. M. Yasin (ed.), *Recent Progress in Optical Fiber Research*, InTech, 2012. Cited on pages 6 and 17.
- [Eic81] W. Eickhoff and R. Ulrich: *Optical Frequency Domain Reflectometry in Single Mode Fiber*, Applied Physics Letters **39**, 693 (1981). Cited on pages 59 and 71.
- [Erd96] T. Erdogan and J. E. Sipe: *Tilted Fiber Phase Gratings*, Optical Society of America **13**, 296 (1996). Cited on page 9.
- [Erd97] T. Erdogan: *Fiber Grating Spectra*, Journal of Lightwave Technology **15**, 1277 (1997). Cited on pages 9, 74, and 75.
- [Fan12] Z. Fang, K. K. Chin, R. Qu and H. Cai: *Fundamentals of Optical Fiber Sensors*, John Wiley & Sons, 2012. Cited on page 71.
- [Fer00] L. A. Ferreira, J. L. Santos, F. Farahi and F. M. Araújo: *Simultaneous Measurement of Strain and Temperature Using Interferometrically Interrogated Fiber Bragg Grating Sensors*, Optical Engineering **39**, 2226 (2000). Cited on pages 6, 12, 13, 17, and 74.
- [Gen05] J. Geng, C. Spiegelberg and S. Jiang: *Narrow Linewidth Fiber Laser for 100-km Optical Frequency Domain Reflectometry*, IEEE Photonics Technology Letters **17**, 1827 (2005). Cited on page 60.
- [GH03] U. S. amd G. Hirzinger: *A 6-axis Force/Torque Sensor Design for Haptic Feedback in Minimally Invasive Robotic Surgery*, MICRO.tec - 2nd VDE World Microtechnologies Congress , 239 (2003). Cited on page 1.

- [Gho94] G. Ghosh: *Temperature Dispersion of Refractive Indexes in some silicate fiber glasses*, IEEE Photonics Technology Letters **6**, 431 (1994). Cited on page 5.
- [Gif07] D. K. Gifford, M. E. Froggatt, M. S. Wolfe, S. T. Kreger, A. K. Sang and B. J. Soller: *Millimeter Resolution Optical Reflectometry Over Up to Two Kilometers of Fiber Length*, in *Avionics, Fiber-Optics and Photonics Technology Conference, 2007 IEEE*, 2007, 52–53. Cited on pages 60, 61, and 69.
- [Gri07] P. Griffiths and J. A. De Haseth: *Fourier Transform Infrared Spectrometry*, John Wiley & Sons, 2007. Cited on page 42.
- [Guo06] T. Guo, X. Qiao, Z. Jia, Q. Zhao and X. Dong: *Simultaneous Measurement of Temperature and Pressure by a Single Fiber Bragg Grating with a Broadened Reflection Spectrum*, Applied Optics **45**, 2935 (2006). Cited on pages 74 and 78.
- [Har70] T. R. Hart, R. L. Aggarwal and B. Lax: *Temperature Dependence of Raman Scattering in Silicon*, Physical Review B **1**, 638 (1970). Cited on pages 16 and 69.
- [Has13] R. Haslinger, P. Leyendecker and U. Seibold: *A Fiberoptic Force-Torque-Sensor for Minimally Invasive Robotic Surgery*, IEEE International Conference on Robotics and Automation (ICRA) , 4375 (2013). Cited on pages 1, 2, and 3.
- [Hil97] K. O. Hill and G. Meltz: *Fiber Bragg Grating Technology Fundamentals and Overview*, Journal of Lightwave Technology **15**, 1263 (1997). Cited on page 9.
- [Hua09] M. Huang, H. Yan, C. Chen, D. Song, T. F. Heinz and J. Hone: *Phonon Softening and Crystallographic Orientation of Strained Graphene Studied by Raman Spectroscopy*, Proceedings of the National Academy of Sciences **106**, 7304 (2009). Cited on page 16.
- [Ina06] D. Inaudi and B. Glisic: *Distributed Fiber Optic Strain and Temperature Sensing for Structural Health Monitoring*, Int'l Conference on Bridge Maintenance, Safety and Management **3** (2006). Cited on page 16.
- [Inc11] C. Inc.: *Corning SMF-28-e+ Optical Fiber*, Product Information **PI1463** (2011). Cited on page 55.
- [Ley10] P. Leyendecker: *Temperaturkompensation faseroptischer Kraft-Momenten-Sensoren mittels Fluoreszenz-Lebensdauer Messung*, Diplomarbeit, Technische Universität München (2010). Cited on pages 2 and 28.
- [Lid00] D. P. Lide (ed.): *CRC Handbook of Chemistry and Physics*, CRC PRESS, 2000, 81st edn.. Cited on page 74.
- [Mac81] R. I. MacDonald: *Frequency Domain Optical Reflectometer*, Applied Optics **20**, 1840 (1981). Cited on page 57.

- [Mat09] Mathworks, Solution ID 1-1MD9F1: *How can I fit my data to a curve that is only defined implicitly, using Optimization Toolbox 3.0 (R14)?* (2009). Cited on page 27.
- [McC64] D. E. McCumber: *Einstein Relations Connecting Broadband Emission and Absorption Spectra*, Physical Review **136**, A954 (1964). Cited on pages 21 and 35.
- [Mel89] G. Meltz, W. Morey and W. H. Glenn: *Formation of Bragg Gratings in Optical Fibers by a Transverse Holographic Method*, Optics Letters **14**, 823 (1989). Cited on page 9.
- [Mys97] P. Myslinski, D. Nguyen and J. Chrostowski: *Effects of Concentration on the Performance of Erbium-Doped Fiber Amplifiers*, Journal of Lightwave Technology **15**, 112 (1997). Cited on page 14.
- [Nak87] J. Nakayama, K. Iizuka and J. Nielsen: *Optical Fiber Fault Locator by the Step Frequency Method*, Applied Optics **26**, 440 (1987). Cited on page 55.
- [New07] T. C. Newell, P. Petersen, A. Gavrielides and M. P. Sharma: *Temperature Effects on the Emission Properties of Yb-Doped Fibers*, Optics Communications **273**, 256 (2007). Cited on page 14.
- [Oko80] T. Okoshi, K. Kikuchi and A. Nakayama: *Novel Method for High Resolution Measurement of Laser Output Spectrum*, Electronics Letters **16**, 630 (1980). Cited on page 70.
- [Ops10] Opsens inc.: *Opsens White-Light Polarization Interferometry Technology* (2010). Cited on page 7.
- [Par96] F. Parvaneh, M. Farhadiroushan, V. Handerek and A. Rogers: *High-resolution optical-fibre distributed temperature sensor based on the frequencyderived technique*, Electronics Letters **32**, 2263 (1996). Cited on page 8.
- [Par97] T. R. Parker, M. Farhadiroushan, V. A. Handerek and A. J. Rogers: *Temperature and Strain Dependence of the Power Level and Frequency of Spontaneous Brillouin Scattering in Optical Fibers*, Optics Letters **22**, 787 (1997). Cited on pages 16 and 69.
- [Pas97] R. Paschotta, J. Nilsson, A. C. Tropper and D. C. Hanna: *Ytterbium-Doped Fiber Amplifiers*, IEEE Journal of Quantum Electronics **33**, 1049 (1997). Cited on page 36.
- [PCW96] T. P. N. P. C. Wait: *Landau Placzek Ratio Applied to Distributed Fibre Sensing*, Optic Communications **122**, 141 (1996). Cited on page 16.
- [Pow98] R. C. Powell: *Physics of Solid-State Laser Materials*, Springer-Verlag, 1998. Cited on page 36.

-
- [Rao97] Y. Rao, D. J. Webb, D. A. Jackson, L. Zhang and I. Bennion: *In-fiber Bragg-Grating Temperature Sensor System for Medical Applications*, *Lightwave Technology* **15**, 779 (1997). *Cited on page 9.*
- [Rob87] I. M. Robinson, M. Zakikhani, R. J. Day, R. J. Young and C. Galiotis: *Strain Dependence of the Raman Frequencies for Different Types of Carbon Fibres*, *Journal of Materials Science Letters* **6**, 1212 (1987). *Cited on page 16.*
- [Sam12] D. Samiek: *Distributed fibre-optic temperature and strain measurement with extremely high spatial resolution*, *Photonik International* , 10 (2012). *Cited on page 11.*
- [Sch91] K. Schick, E. Daub, S. Finkbeiner and P. Würfel: *Verification of a Generalized Planck Law for Luminescence Radiation from Silicon Solar Cells*, *Applied Physics A* **54**, 109 (1991). *Cited on page 36.*
- [Sin07] S. P. Singh, R. Gangwar and N. Singh: *Nonlinear Scattering Effects in Optical Fibers*, *Progress In Electromagnetics Research* **74**, 379 (2007). *Cited on page 16.*
- [Sir93] R. S. Sirohii: *Wave Optics And Its Applications*, Orient Longman Limited, 1993. *Cited on page 72.*
- [SNA08] I. SCHOTT North America: *Temperature Coefficient of the Refractive Index*, Technical Information **TIE-19** (2008). *Cited on page 74.*
- [Sol05] B. Soller, D. Gifford, M. Wolfe and M. Froggatt: *High Resolution Optical Frequency Domain Reflectometry for Characterization of Components and Assemblies*, *Optics Express* **13**, 666 (2005). *Cited on page 64.*
- [Son10] K. Y. Song, S. Chin, N. Primerov and L. Thévenaz: *Time-Domain Distributed Sensor with 1 cm Spatial Resolution Based on Brillouin Dynamic Gratings*, *Lightwave Technology* **28**, 2062 (2010). *Cited on page 16.*
- [Sun98] T. Sun, Z. Y. Zhang, K. T. V. Grattan and A. W. Palmer: *Ytterbium-Based Fluorescence Decay Time Fiber Optic Temperature Sensor Systems*, *Review of Scientific Instruments* **69**, 4179 (1998). *Cited on pages 19, 31, and 32.*
- [Sun04] W. Sun, J. Zhang, L. Yu, Y. Zhang, Y. Xiang, L. Yuan, T. Sun and K. T. V. Grattan: *Measurement of Decay Time Based on FFT*, *Optics & Laser Technology* **36**, 323 (2004). *Cited on page 19.*
- [Thé10] L. Thévenaz: *Brillouin Distributed Time-Domain Sensing in Optical Fibers: State of the Art and Perspectives*, *Frontiers of Optoelectronics in China* **3**, 13 (2010). *Cited on page 16.*

- [Ven93] S. Venkatesh and W. Sorin: *Phase Noise Considerations in Coherent Optical FMCW Reflectometry*, Journal of Lightwave Technology **11**, 1694 (1993). Cited on page 68.
- [Yük09] K. Yüksel, M. Wuilpart, V. Moeyaert and P. Mégret: *Optical Frequency Domain Reflectometry: A Review*, in *11th International Conference on Transparent Optical Networks*, 2009, 1–5. Cited on page 55.
- [Yük11] K. Yüksel, P. Mégret and M. Wuilpart: *A Quasi-Distributed Temperature Sensor Interrogated by Optical Frequency-Domain Reflectometer*, Measurement Science and Technology **22**, 115204 (2011). Cited on page 73.
- [Zha93] Z. Zhang, K. T. V. Grattan and A. W. Palmer: *Phaselocked Detection of Fluorescence Lifetime*, Review of Scientific Instruments **64**, 2531 (1993). Cited on page 19.
- [Zha96] Z. Zhang, K. T. V. Grattan, Y. Hu, A. W. Palmer and B. T. Meggitt: *Prony's Method for Exponential Lifetime Estimations in Fluorescencebased Thermometers*, Review of Scientific Instruments **67**, 2590 (1996). Cited on page 19.

Acknowledgements

I would like to thank my advisors Robert Haslinger and Patrick Leyendecker at the DLR for their patience, for enduring thousands of emails, for helping me to solve almost every problem, giving me interesting and helpful research material and helping me setting up the measurements. Special thanks goes to Patrick Leyendecker for supplying me with his measurement-setups and even redoing his measurements to fulfill my needs. Additionally, I would like to thank my colleagues Thomas Scherübl and Serkan Türker for listening to all my thoughts and adding their own remarks, that often lead to the solution.

At last, this work would not have been possible without Prof. Paolo Lugli, who supervised this Master Thesis although it was entirely written at an external institution.

Eidesstattliche Erklärung

Hiermit versichere ich, die vorliegende Arbeit selbstständig verfasst und keine anderen als die angegebenen Quellen und Hilfsmittel benutzt sowie die Zitate deutlich kenntlich gemacht zu haben.

Ort, Datum

Martin Kaumanns

